AFP: A Proposal to Install Proton Detectors at 220 m around ATLAS to Complement the ATLAS High Luminosity Physics Program

L. Adamczyk[a], R. B. Appleby[b,c], P. Bańka[d], M. Boonekamp[e], A. Brandt[f], P. Bussey[g], M. Campanelli[h], E. Chapon[e], J. Chwastowski[d], B. Cox[b], E. Delagnes[e], M. Dueren[i], A. Farbin[f], J.-F. Genat[j], H. Grabas[e], Z. Hajduk[d], H. Hakopian[k], Z. Janoska[l], O. Kepka[l], A. Kupčo[l], V. Kus[l], S. Liu[m], A. Pilkington[b,n], J. Pinfold[m], P. Ponsot[e], K. Potter[b,o], M. Przybycień[a], M. Rijssenbeek[q], C. Royon[e], P. Ruzicka[l], L. Schoeffel[e], R. Soluk[m], J. Soukup[m], R. Staszewski[d,e], T. Sykora[r], H. Stenzel[i], M. Tasevsky[l], T. Tic[l], M. Trzebiński[d,e], J. Turnau[d], V. Vacek[s], A. Valkarova[r], V. Vrba[l], S. Watts[b], and M. Zeman[e,l]

[a]Faculty of Physics and Applied Computer Science, AGH-University of Science and Technology, Cracow, Poland

[b]University of Manchester, UK
[c]CERN, Geneva, Switzerland

[d]Institute of Nuclear Physics, Polish Academy of Sciences, Kraków, Poland
[e]IRFU, CEA Saclay, France

[f]University of Texas Arlington, USA
[g]University of Glasgow, UK

[h]University College London, UK

[i]University of Giessen, Germany

[j]LPNHE, University of Paris 6-7, France

[k]University of Yerevan, Armenia

[l]Institute of Physics, Academy of Sciences of the Czech Republic, Na Slovance 2, CZ - 18221 Praha 8, Czech Republic
[m]University of Alberta, Canada
[n]University of Durham, UK
[o]Cockroft Institute, UK
[q]Stony Brook University, USA
[r]Charles University, Prague, Czech Republic
[s]Czech Technical University, Prague, Czech Republic

February 22, 2011

Abstract

We present the Technical Proposal to build and install forward proton detectors at 220 m from the interaction point on both sides of the ATLAS experiment. The detectors would be designed to operate at high instantaneous luminosities of up to 10^{34} cm^{-2}s^{-1}. The primary goal is to enhance the ATLAS baseline physics program, particularly the anomalous couplings between γ and W or Z as well as QCD studies. AFP will allow Higgsless and Extra-dimension models to be probed with an unprecedented precision by searching for anomalous couplings between γ and W/Z. We propose the installation of moveable beam pipes housing precision silicon and timing detector to enable this physics program during the 2013-2014 shutdown.

Contents

Chapter 1

Introduction

This Technical Proposal presents Stage I of the ATLAS Forward Proton (AFP) upgrade for ATLAS Upgrade Phase 0. The proposal consists of a plan to add high precision detectors at ~ 220 m upstream and downstream of the ATLAS interaction point to detect intact final state protons scattered at small angles and with small momentum loss. The capability to detect *both* outgoing protons in diffractive and photoproduction processes in conjunction with the ATLAS central detector enables a rich QCD, electroweak and beyond the Standard Model experimental program.

A prime process of interest is Central Exclusive Production (CEP), $pp \to p + \phi + p$, in which the central system ϕ may be, for example, a pair of W or Z bosons, a pair of jets, or a neutral Higgs boson. The observation of a new particle in the CEP channel allows for a direct determination of its quantum numbers, since to a good approximation only 0^{++} central systems can be produced in this manner. Furthermore, tagging both protons allows the mass of the centrally produced system ϕ to be reconstructed with a resolution (σ) between 3 GeV and 6 GeV per event if both protons are tagged at 220 m, irrespective of the decay products of the central system. Tagging both protons allows the probing of anomalous couplings between γ and W or Z with an unprecedented precision. Simulations show that it is possible to improve the LEP sensitivity by four orders of magnitude with 30 fb^{-1}, which should be sufficient to discover or rule out Higgsless or Extra-dimension models.

To enable this physics program, we propose to install movable beam pipes at $\pm$ 216 m and $\pm$ 224 m from the ATLAS main detector. This specialized beam pipe will both house the AFP detectors, and allow them to be positioned within a few mm of the circulating beam. The primary detector is a silicon tracking spectrometer which uses points measured along the track at the two stations in conjunction with the LHC dipole and quadrupole magnets to reconstruct the momentum and scattering angle of the final state protons. The acceptance covers fractional momentum losses in the range $0.02 < \xi < 0.2$. For events in which both protons are tagged, this corresponds to a range of central masses from several hundred GeV (depending on the distance of the detectors from the beam) to beyond 1 TeV. The movable beam pipe will also contain precision timing detectors to suppress overlap combinatoric backgrounds.

This proposal was solicited by ATLAS Executive Board following an extensive review of the AFP Letter of Intent [1], which was submitted to ATLAS in fall of 2008. Details of the review process are available at [2]. The major concerns of the review committee (listed here for reference) have largely all been addressed:

1. **Consistency of the AFP schedule with the LHC schedule**: we have addressed this with our staging plan and discuss the key milestones in Chapter 6.

2. **Silicon detector lifetime issues**: we have removed this concern by switching from the FE-I3 to FE-I4 chip, which is much better designed to deal with the high expected flux rates.

3. **Micro-channel plate PMT lifetime issues**: these have been reduced by R&D with Hamamatsu, Photonis, and Photek as well as improved detector design; the requirements are also less significant in the moderate luminosity expected up to about 2016.

4. **Trigger issues**: these include concerns about trigger bandwidth, latency, method, and simulation. Dedicated triggers are not going to be needed due to the acceptance limitation at low mass, removing this entire category from concern. Nevertheless, we will employ a simple Level 1 trigger using the timing system, paving the way for a more sophisticated trigger in Stage II (equivalent timescale to Upgrade Phase I).

5. **Machine issues**: these include concerns about interference with the collimation system and the cryostats as well as a safety review. We developed an alternate collimation scheme that protects critical LHC components while maintaining sufficient acceptance to enable the AFP physics program. We have deferred the cryostat issues by moving the 420 m installation to Stage II, although we note that the cryostat bypass that we developed has been largely incorporated into the LHC cryo-collimator design, so this is no longer a significant concern. The safety review is only possible after the Technical Proposal is approved, since it requires interaction with the accelerator experts.

The outline of this document is as follows: Chapter 2 presents the physics motivation of the proposed 220 m system, Chapter 3 describes the Hamburg movable beampipe solution for housing both silicon tracking and fast timing detectors, Chapter 4 describes the silicon tracking detector, Chapter 5 describes the timing detector, and Chapter 6 present the conclusions, as well as a brief discussion of resources, and a project timeline. The Appendix includes details on collimation and acceptance studies, and a potential future extension of the project by adding detectors at 420 m, which would greatly improve the low mass acceptance.

Chapter 2

Physics Case

2.1 Introduction

The purpose of the new forward detectors described in this technical proposal is to open a possibility to identify and record events with leading intact protons emerging from inelastic collisions occurring in ATLAS. Historically, measurements involving intact leading protons are mainly associated with diffractive analyses (involving soft pomeron exchanges). Probing the structure of a nucleon under special conditions which do not lead to its disruption enhances our understanding of hadrons beyond what is achieved solely by conventional measurements.

With the high energy proton beams at the LHC, forward physics enters a new era. The exclusive productions with leading protons in the event have seizable cross sections and can be exploited to give very precise electroweak or SUSY measurements. Detecting the leading protons on either one or both sides of the central detector broadens the spectrum of physics analyses that can be carried out and maintains the competitiveness of ATLAS with other experiments, in particular with CMS, which has a better coverage in the forward region and thus has higher sensitivity to the above-mentioned processes.

One possibility for a system ϕ to be produced exclusively is via an exchange of two photons $pp \to p(\gamma\gamma)p \to p + \phi + p$ [3, 4, 5]. The two photons may couple to electroweak bosons, leptons or SUSY particles. A schematic diagram of these exchanges is shown in Figure 2.1. The '+' sign denotes the regions devoid of activity, often called rapidity gaps. The cross section falls very quickly as a function of the photon transverse momentum, and the photons move mainly in the longitudinal direction. Outgoing protons therefore scatter at very small angles. The radiation of collinear photons off protons is largely calculable within perturbative Quantum Electrodynamics, and the cross sections have relatively small theoretical uncertainties, especially since rescattering corrections are small. These processes can therefore provide unique precision measurements of the electroweak sector of the Standard Model (SM) and reveal details of the electroweak symmetry breaking also in the case where there is no Higgs boson. The advantage of AFP is that by tagging the outgoing protons and with few relatively simple additional requirements in the central detector, the selected event is ensured to be initiated by two-photons. Electroweak tests can therefore be performed with higher precision than by using the central detector only. As we will see in the following of this chapter, this process will allow to probe anomalous couplings between γ and W/Z with a unprecentented precision at the LHC.

A second topic consists of the exclusive diffractive production. Central exclusive production (CEP) of new particles has received a great deal of attention in recent years [6, 7, 9]. The production is driven by an exchange of a di-gluon system. The color flow is screened by an exchange of an additional gluon such that the produced system is colorless. Due to the very

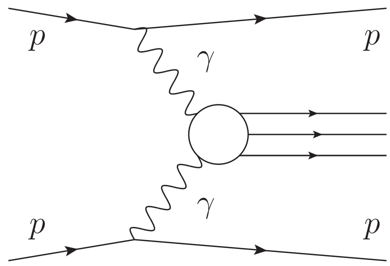

Figure 2.1: Exclusive production occurring via the exchange of di-photon system.

small scattering angles of the outgoing protons, this system obeys to a good approximation a J_z = 0, C-even, P-even, selection rule, so that the quantum numbers of the produced system are constrained, irrespective of the decay channel.

The particular physics program of two-photon and CEP physics depends strongly on the acceptance of the ATLAS Forward Proton Detectors in terms of the mass of the exclusive system $W^2 = s\xi_1\xi_2$, where ξ is the proton fractional momentum loss and s is the centre-of-mass energy of the pp collision. The range in ξ to which detectors are sensitive are determined by the geometrical acceptance of the forward detectors. Reaching as low W masses as possible is desired to maintain high production yields because diffractive and exclusive production cross sections roughly fall as $1/\xi$.

As discussed in Appendix III, the production and installation of 420 m detectors is much more intricate than for those at 220 m since they require the installation in the cold region of the LHC and a dedicated cryogenic design. The detector acceptance in fractional momentum loss acceptance at 220 m is of the order $\xi \sim 1-10\%$, while it is $\xi \sim 0.1-1\%$ for those installed at 420 m. The physics program of the AFP project in the baseline configuration with detectors at 220 m only is reviewed in this document. They provide an acceptance to relatively large exclusive masses. The program of a possible extension of the project with more distant detectors is briefly summarized in Appendix III.

2.2 Acceptance

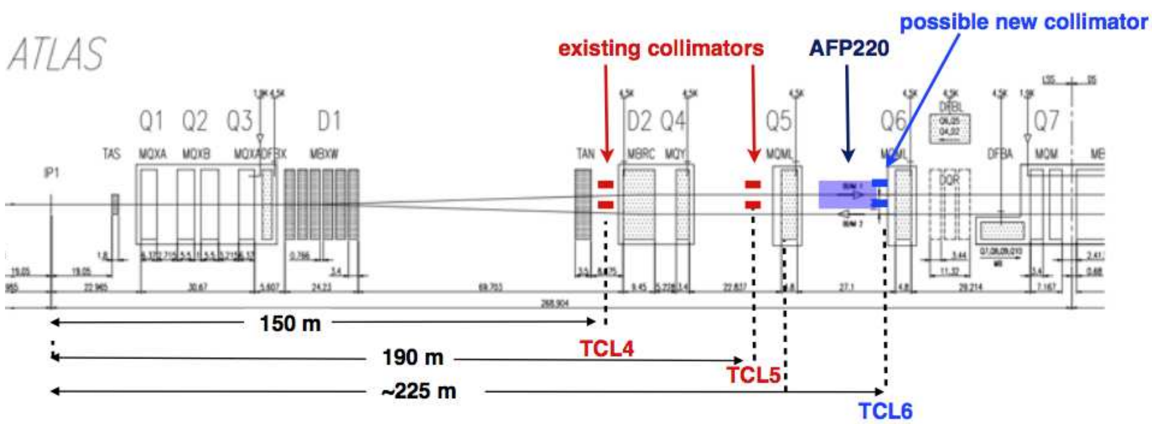

Figure 2.2: Layout of the straight section on the right side of ATLAS.

To obtain the acceptance in fractional proton momentum ξ and thus the physics possibilities

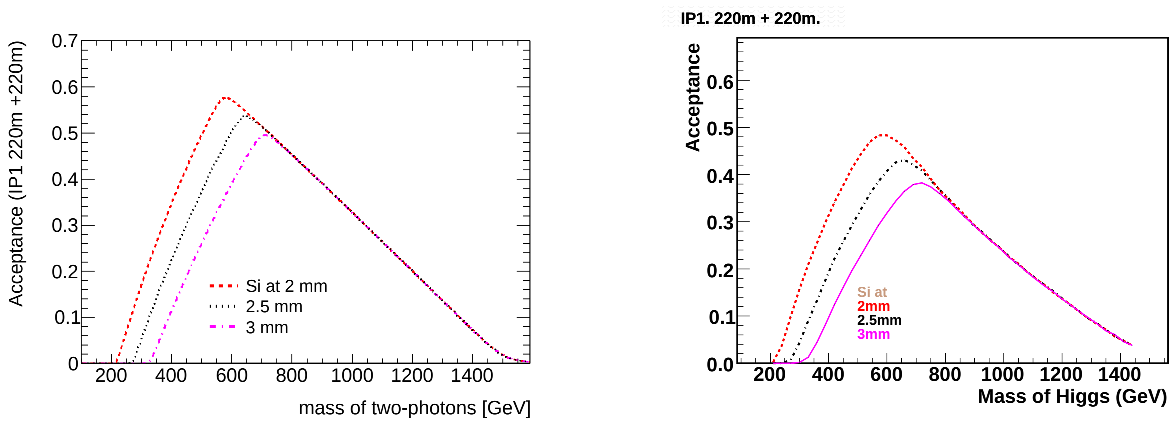

Figure 2.3: Geometrical acceptances due to a limited coverage of the forward detectors in ξ and t in terms of central exclusive mass two-photon exclusive (left) and central exclusive (right) productions.

of our detector, we assume the existence of three collimators called TCL4, TCL5 and TCL6 in front of our detectors at 220 m as described in Fig. 2.2. Compared to the default present situation, this solution assumes that the positions of TCL4 and TCL5 are at 30 and 50 σ from the beam respectively [1]. In addition, the TCL6 new collimator is positioned at 40 σ from the beam. This solution allows to keep a good acceptance for diffracted protons and was admitted as a possible alternative to the present scheme by the LHC Vaccuum group. It is presented in detail in Appendix I of this technical proposal.

The acceptance as a function of mass produced in exclusive events is depicted in Figure 2.3 for two-photon physics (left) and CEP production (right). They are obtained by means of a complete simulation of the scattered protons through the LHC optical elements; the proton tracking through the LHC beam line is discussed in Appendix II. It is shown for various distances of the forward detectors from the beam - 2, 2.5, and 3 mm, which denote the "optimist", "realistic", and "pessimistic" configuration scenarios. In all cases, the 220 m acceptance removes events below $\sim$ 300 GeV. Due to larger tails in mass for two-photon production, the acceptance is in general slightly larger than in CEP. In particular, for the baseline detector distance of 2.5 mm the acceptance at its maximum $W = 650$ GeV is by about 10% higher than the acceptance for central exclusive production.

Furthermore, the reduced mass acceptance significantly lowers the yield of CEP processes. For example, only a couple of events are expected for exclusive di-jets with $p_{\mathrm{T}}^{jet} > 60$ GeV. The double proton tag is required in order to remove pile-up background, in which non-diffractive di-jet event is overlayed with soft diffractive events giving a proton hit in forward detectors using the forward detectors. This can be done by comparing the jet and the reconstructed kinematics. Due to its small yield, the exploratory physics program using central exclusive processes (Higgs bosons...) is not considered with 220 m detectors only and the focus is made on the two-photon exclusive production and the standard QCD diffractive measurements. However, the search for exclusive diffractive events in the jet channel as performed by the CDF collaboration is still possible [10].

[1] We recall that the assumed position of TCL4 and TCL5 for the default scenario is at 15 σ deom the beam which kills fully the acceptance of our 220 m detectors.

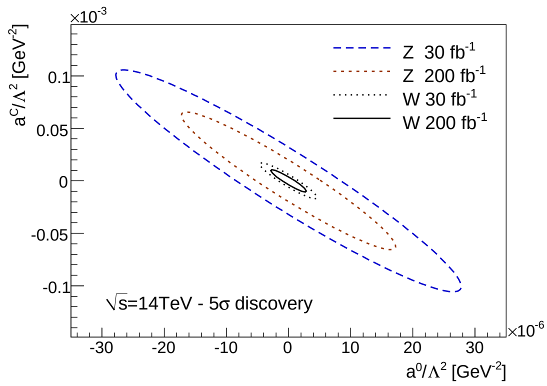

Figure 2.4: 5σ discovery contours for all the WW and ZZ quartic couplings at $\sqrt{s} = 14$ TeV for luminosity of 30 fb^{-1} and 200 fb^{-1}. See [4] for notation.

2.3 Photon-photon physics

In this section we consider inelastic photon-photon collisions, $pp \to p(\gamma\gamma)p \to pXp$. The central system in the final state is separated on each side by a large rapidity gap from forward protons. Photon-photon fusion opens up a rich electroweak program that complements the QCD physics. Recently, the exclusive two-photon production of lepton pairs has been observed by the CDF collaboration [11] and is in good agreement with the theoretical predictions.

2.3.1 Lepton pair production

Two-photon exclusive production of muon pairs has a well known QED cross section, including very small hadronic corrections. Thanks to its distinct signature, the selection procedure is very simple: two muons within the central detector acceptance ($|\eta| < 2.5$), with transverse momenta above a minimum value $p_T > 10$ GeV depending on the experimental trigger. After applying this selection criterion and requiring one forward proton tag, the cross section is ~ 25fb for the detector distance of 2.5 mm from the beam. Due to the exclusivity of the event, the dilepton p_T is very much correlated with the proton ξ and cross section is very sensitive to the position of the edge of the detector with respect to the beam. After requesting one proton tag in detector placed at 2.0 mm from the beam, only muons with $p_T > 10$ GeV can be measured. This means that triggers with lower p_T thresholds are not necessary. Using di-muon trigger may help to keep prescales low for high machine luminosities. As discussed in Appendix II, two-photon dimuon events can be used for calibration of 220 m detectors to a required accuracy with about hundred of such events.

If 420 m taggers can be installed, the cross section increases to 1.3 pb [4, 5]. This corresponds to ~ 50 muon pairs detected in a 12 hour run at a mean luminosity of 10^{33} cm^{-2}s^{-1}. Apart for calibration purposes, the large event rate coupled with a small theoretical uncertainty makes this process a potentially important candidate for the measurement of the absolute LHC luminosity [12]. The e^+e^- production can also be studied at ATLAS, although the trigger thresholds will be larger and hence the final event rate reduced.

2.3.2 Vector boson production

This section describes the main physics topics of AFP which allows to probe electroweak symmetry breaking with unprecedented precision.

Couplings	OPAL limits [GeV^{-2}]	Sensitivity @ $\mathcal{L} = 30$ (200) fb^{-1} 5σ	95% CL
a_0^W/Λ^2	[-0.020, 0.020]	5.4 10^{-6} (2.7 10^{-6})	2.6 10^{-6} (1.4 10^{-6})
a_C^W/Λ^2	[-0.052, 0.037]	2.0 10^{-5} (9.6 10^{-6})	9.4 10^{-6} (5.2 10^{-6})
a_0^Z/Λ^2	[-0.007, 0.023]	1.4 10^{-5} (5.5 10^{-6})	6.4 10^{-6} (2.5 10^{-6})
a_C^Z/Λ^2	[-0.029, 0.029]	5.2 10^{-5} (2.0 10^{-5})	2.4 10^{-5} (9.2 10^{-6})

Table 2.1: Reach on anomalous couplings obtained in γ induced processes after tagging the protons in the final state in the ATLAS Forward Physics detectors compared to the present OPAL limits. The 5σ discovery and 95% C.L. limits are given for a luminosity of 30 and 200 fb^{-1}

The cross section of exclusive two-photon production of W boson pairs is expected to be about 100 fb at the LHC [5]. The majority of such events would require one proton tagged at 220 m and one proton tagged at 420 m due to the relatively large mass of the central system. The easiest selection consists of large missing $E_\mathrm{T}^\mathrm{miss}$ and large p_T of electron or muon. Asking $E_\mathrm{T}^\mathrm{miss} > 20$ GeV and $p_\mathrm{T} > 25$ GeV together with the double proton tag in 220 m detectors results in ~ 10 events per $30\mathrm{fb}^{-1}$ with zero background expected from QCD. The overlap background is expected to be small due to an intrinsically large cut on mass required by forward 220 m detectors.

Moreover, vector boson pair production provides an opportunity to investigate anomalous gauge boson couplings, in particular the anomalous quartic gauge couplings (QGCs) $\gamma\gamma VV$. Note that in the SM, the tree-level pair production of Z bosons by photon-photon fusion is not allowed and any observation of exclusive ZZ final states implies an anomalous coupling. Conversely, the SM does allow both triple and quartic gauge couplings, γW^+W^- and $\gamma\gamma W^+W^-$ and the anomalous contribution would exist as an excess over the SM prediction.

The sensitivity of a forward detector system to anomalous gauge couplings has been investigated in [4, 5] for the leptonic decays $\gamma\gamma \to W^+W^- \to l^+l^-\,\nu_l\,\bar{\nu}_l$ and $\gamma\gamma \to ZZ \to l^+l^- j\,j$, using the signature of two leptons (e or μ). In the second set of references, a complete analysis with numerous diffractive and two-photon backgrounds was carried out for the 220+420 m detectors. The anomalous coupling appears predominantly at high two-photon masses and is selected applying $E_\mathrm{T}^\mathrm{miss} > 20$, $p_\mathrm{T} > 25$ GeV, $|\eta| < 2.5$ of the leading lepton and requiring large invariant reconstructed mass in forward detectors $W > 800$ GeV. The results are presented as 5σ discovery contour limits in Figure 2.4, and in Table 2.1.

The sensitivities obtained using AFP and 30 fb^{-1} of data are about 10000 times better than the best limits established at LEP2 [13] and about 100 times better then using the central detector only in analysis studying radiation zero in $pp \to l^\pm\nu\gamma\gamma$ events ($l = e$ or μ) [14]. These sensitivities reach the values expected for Higgless or extra-dimension kinds of models (a few 10^{-6}). This study show the great potential of AFP to probe these new kinds of models with a precision which does not seem to be reachable by other means at the LHC. The studies of the sensitivity using AFP were performed again with a reduced acceptance in mass corresponding to 220 m only. Since large mass $W > 800$ GeV was already required in the previous analysis, the sensitivity is not much degraded. Depending on the anomalous parameter, the limits are between 1000-10000 better than the best limits from LEP2, clearly showing the large and unique potential of such studies at the LHC even using 220 m detectors only. This will allow to probe with an with high precision the electroweak symmetry breaking in the SM model. As mentioned already, such values of the couplings to which AFP is sensitive appear in some Higgsless or extra-dimension models, even though the exact link between the studied effective Lagrangian and the particular theories is difficult to make due to not easy theoretical calculation. New signal not compatible with the SM predictions would surely stimulate the interest in these theories [15].

2.4 Diffraction and QCD

Proton tagging at ATLAS will allow the study of hard diffraction, expanding and extending the investigations carried out at CERN by UA8 [16], more recently at HERA by H1 and ZEUS and at Fermilab by CDF and D0 (see e.g. [17, 18, 20, 19] and references therein). At low luminosity, single diffractive (SD) meson, di-jet and vector boson production, $pp \to pX$, can be observed. At higher luminosities, double pomeron exchange, $pp \to pXp$, can be used for similar studies, the lower event rate being compensated by additional rejection against the combinatorial overlap backgrounds (from requiring one extra proton tag and vertex matching using the fast-timing detectors). Note that DPE is distinct from CEP, as the central system contains remnants from the diffractive exchange in addition to the hard subprocess. These processes are sensitive to the low-x structure of the proton and the diffractive parton distribution functions (dPDFs). Inclusive jet and heavy quark production are mainly sensitive to the gluon component of the dPDFs, while vector boson production is sensitive to quarks. The kinematic region covered expands that explored at HERA and Tevatron, with values of β (the fractional momentum of the struck parton in the diffractive exchange) as low as 10^{-4} and of Q^2 up to tens of thousands of GeV^2.

SD and DPE can also be used to determine the soft-survival probability, which is interesting in its own right because of its relationship with multiple scattering effects and hence the structure of the underlying event in hard collisions. Azimuthal correlations between the two forward protons produced in DPE allow the soft-survival factor to be probed as a function of the proton kinematics. More detailed studies, including diffractive di-jet production, W and Z production and B meson production can be found in [20].

Besides the diffractive analyses involving a hard scatter mentioned above, forward detectors will allow the analysis of the particle flow in soft diffractive events for example by measuring the charged particle distributions in events with one proton tag. Such studies will be performed at the very beginning of the physics program since the issue of additional pile-up events is less problematic than in hard diffraction. The modeling of the soft diffractive component is quite different between various Monte Carlo generators (such as PYTHIA6/8, PHOJET). The validity of the triple-pomeron approach in Regge theory can be tested by measuring the soft diffractive cross section as a function of the diffractive mass $M^2 = s\xi$ [21, 22].

2.5 Summary

Forward proton tagging at ATLAS has the potential to significantly increase the physics reach of the experiment. The key experimental channels only accessible using the very precise forward detectors are central double pomeron exchange and photon-photon physics. Two proton tags coupled with time-of-flight information from the forward detectors will allow inclusive (parton-parton) backgrounds to be adequately rejected, even for the fully hadronic final states, at high luminosity running.

Diffraction and QCD	
Soft diffraction	YES
Luminosity monitoring	YES
Survival probability	YES
PDF in Pomeron measurements	YES
Single diffractive W, Z, jets	YES
Double pomeron exchange jets	YES
Double pomeron exchange WW, ZZ	YES
Photon-Photon Physics	
Alignment (lepton pairs)	YES
Luminosity measurement	NO
Anomalous couplings of vector bosons	YES
Threshold scan WW	NO
Light SUSY	NO
$\gamma g \to tt$	NO
$\gamma g \to t$	NO
Associated WH production	NO
Central Exclusive Production	
BSM Higgs quantum number measurement	NO
Di-jets, Study of Sudakov suppression	NO

Table 2.2: Summary of measurements which can be performed with a reduced forward detector acceptance using only 220 m detectors with respect to the complete 220+420 m setup described in Appendix III.

In the first phase of installation before the inclusion of 420 m detectors, not all the physics measurements are possible. However, the available acceptance however allows us to perform a number of interesting analyses even without the increased acceptance that 420 m taggers would bring. The 220 m detectors will enable us to exploit the range of forward physics while preparing for the possibility of a 420 m upgrade in a second phase. The program that we anticipate to be available is summarised in Table 2.2.

It is possible to measure single diffraction in which one proton remains intact and is tagged by a forward detector. The majority of these searches have a large cross section and could be investigated during special runs. Further work is required to determine up to which luminosity the measurements can be made. Single diffraction provides additional information on the dPDFs and soft-survival by measuring di-jet and vector boson production.

Photon-photon physics allows absolute luminosity determination and *in situ* forward detector calibration through the well-known QED process, $\gamma\gamma \to \mu^+\mu^-$, though the statistics will be limited with 220 m detectors. Vector boson production in this channel allows competitive sensitivities to be set on the anomalous quartic gauge couplings even in the 220 m running configuration, and allows to extend the ATLAS sensitivities to Higgsless and extra-dimension models with an unprecedented precision.

In the second stage of the forward physics program with 420 m detectors, the study of the Higgs bosons in the supersymmetric extensions, MSSM and NMSSM is made possible. For any resonance production in CEP, the quantum numbers of the produced particle are restricted to $J^{PC} = 0^{++}$ to a very good approximation. In addition, forward detectors provide an excellent mass measurement regardless of the decay products of the produced particle.

In two-photon production, the high yields of $\gamma\gamma \to \mu^+\mu^-$ process allows the absolute luminosity determination and, in addition, *in situ* forward detector calibration through the well-known QED process. Charged SUSY pair production could be measured for light SUSY particles and the information provided by the forward detectors will improve the mass measurement of the new particles. Photoproduction allows the study of single top production, allowing limits to be set on the anomalous γut and γct couplings.

Double pomeron exchange allows the studies of diffractive parton distribution functions and the soft-survival factor, which is responsible for the factorization breaking observed in hard diffractive interactions between ep and $p\bar{p}$ colliders. Event rates for vector meson, di-jet and vector boson production are very large in this case when lower fractional momentum losses of the protons are detectable.

Chapter 3

Hamburg Beampipe

3.1 Introduction

Near beam detectors are typically housed in Roman Pots, such as those used by ALFA, which allow the detector to remain outside of the machine vacuum and be remotely located close to the beam after injection. Due to space restrictions, however, AFP plans to use a moving-beampipe technique developed at DESY [23]. This so-called "Hamburg beampipe" is a large diameter section of beampipe that has rectangular thin wall "pockets" to house the Silicon pixel detectors and precision Time of Flight detectors used to track and time scattered beam protons at $\pm$ 220 m. This specialized section of beampipe is connected at either end to the standard LHC beampipe by bellows that can withstand a transverse displacement of about 25 mm.

The Hamburg pipe mechanics has several advantages over typical Roman Pot technology. It allows a much simpler access to detectors and provides direct mechanical and optical control of the actual detector positions. Unlike the Roman pot system, which has to compensate for the force arising from pressure differences as the detectors are inserted into the vacuum, the Hamburg pipe maintains a fixed vacuum volume. This results in a greatly reduced mechanical stress allowing a very simple and robust design. In effect, the Hamburg pipe is an instrumented collimator. Consequently, the LHC collimator control system and motor design can be adopted with little modification. In this chapter, the main features of the moveable beam pipe design are presented. More detailed information can be found in the FP420 design report [24].

Figure 3.1 shows the layout of the movable beam pipe including two detector stations and the support table. The 220 m support table is much simpler than the 420 m table in Ref. [24], since it is already located in a warm region (no cryo bypass needed) and does not need to support any radiation shielding.

3.2 Hamburg pipe design requirements

The Hamburg pipe has the following requirements:

- It must allow for a precise and repeatable movement of the detectors by $\sim$ 25 mm, so that the detectors housed in pockets in the Hamburg pipe can be kept a safe distance from the beam during filling and tuning.

- It must have minimal deformation and a thin vacuum window both perpendicular and parallel to the beam allowing the detector to be placed within a few mm of the beam.

- The pockets must be optimized to house the different detectors and allow for secondary vacuum and cooling.
- The RF impact of the pockets should be minimal.
- Wherever possible standard LHC components should be used to ensure compatibility with the machine and collimator controls.

3.3 Movable pipe design

Figure 3.2 shows one of the two detector stations equipped with timing and silicon detectors, an LVDT (Linear Variable Differential Transformer) for position measurement and one moving and one fixed beam position monitor (BPM). The support table and motion system are shown in Fig. 3.3.

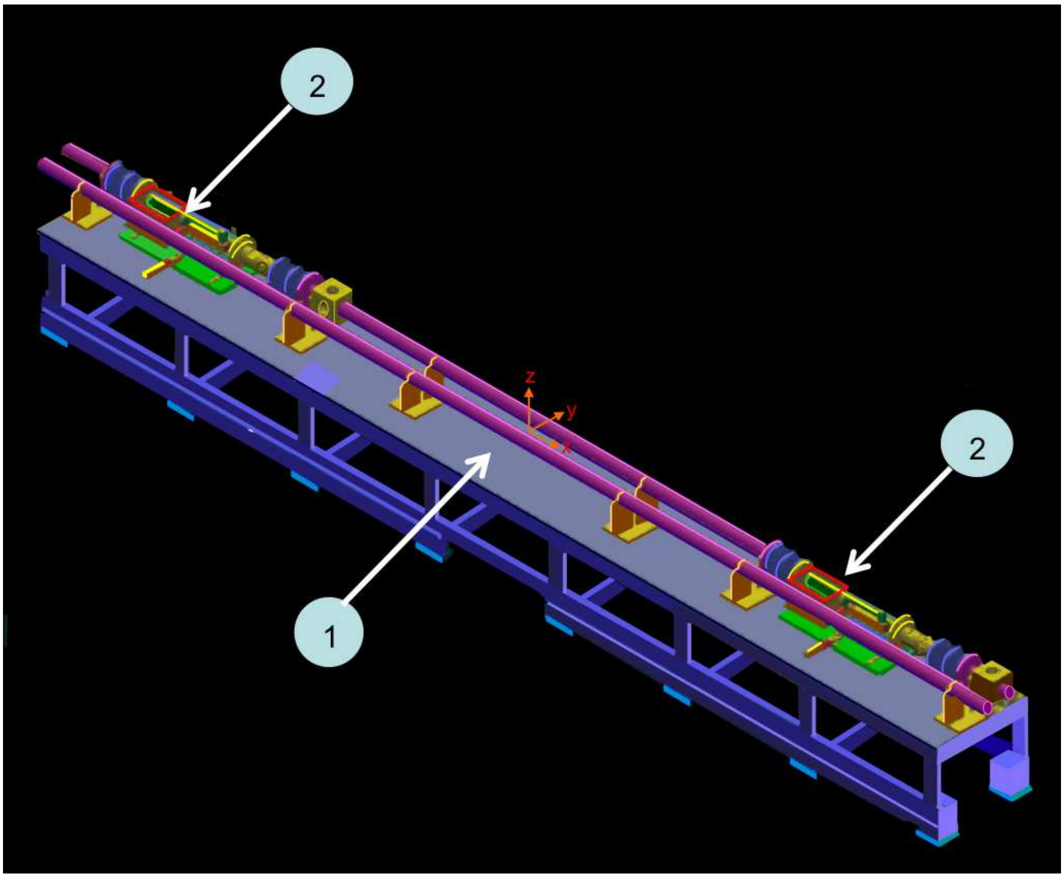

Figure 3.1: Schematic view of the: (1) detector arm with support table; and, (2) detector sections.

For the prototype design, each of the four detector stations (two each at ± 220 m) is composed of a beam-pipe with inner diameter of 68.9 mm, wall thickness of 3.6 mm and two pockets, with default lengths 200 mm for the silicon detectors and 360 mm for the fast timing detectors. Rectangular thin-walled pockets are built into the pipe to house the different detectors that must be positioned close to the beam. The displacement between data taking position and the retracted or parked position is 25 mm. The ends of the moving beam-pipes are connected to the fixed beam-pipes by a set of two bellows.

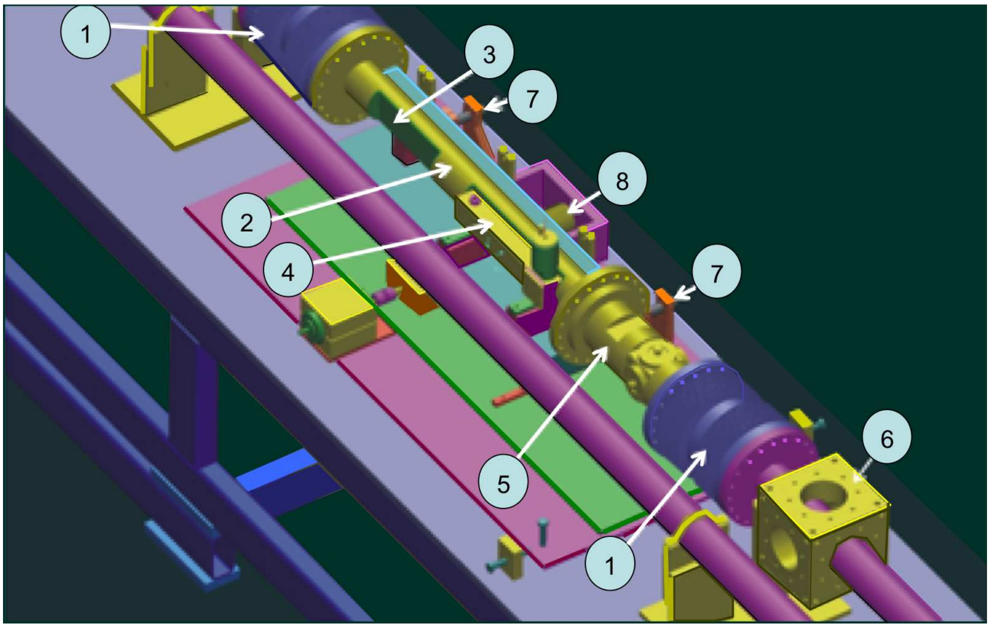

Figure 3.2: Top view of one detector section: bellows (1), moving pipe (2), Si-detector pocket (3), timing detector (4), moving BPM (5), fixed BPM (6), LVDT position measurement system (7), emergency spring system (8).

3.3.1 Pocket design

A key factor in the pocket design is the desire to maximise detector acceptance, which is achieved by minimizing the distance of the detector edge from the LHC beam. This in turn requires that the thickness of the detector pocket wall should be minimised to limit the dead area. Care must be taken to avoid significant window deformation which could also limit the detector-beam distance.

A rectangular shaped detector pocket is the simplest to construct, and minimises the thin window material perpendicular to the beam which can cause multiple scattering and degrade angular resolution of the proton track. Only stainless steel beam tubes are suitable. They will be copper coated for RF-shielding and Non-Evaporative Getter (NEG) coated for vacuum pumping.

3.3.2 Motorization and detector system positioning

In routine operation, detector stations will have two primary positions (1) the parked position during beam injection, acceleration and tuning, and (2) the operational position close to the beam for data taking. The positioning must be accurate and reproducible. Two options have been considered: equipping both ends of the detector section with motor drives which move synchronously but allowing for axial corrections with respect to the beam axis, or a single drive at the centre, complemented with a local manual axial alignment system. A two motor solution in principle allows perfect positioning of the detector station, both laterally and axially. However,

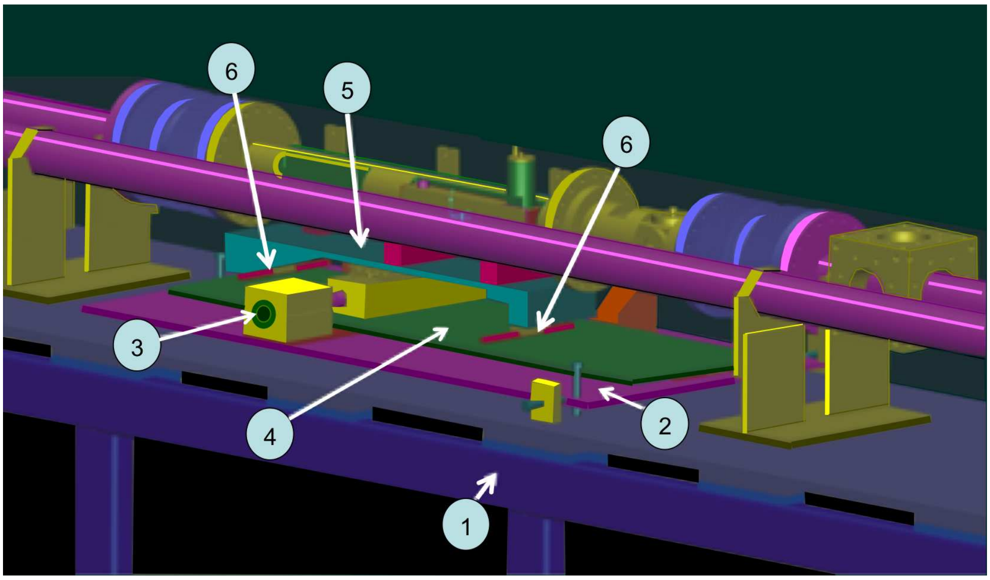

Figure 3.3: Support table (1), drive support table with alignment system (2), drive motor (3), intermediate table for emergency withdrawal (4), moving support table (5), and linear guides (6).

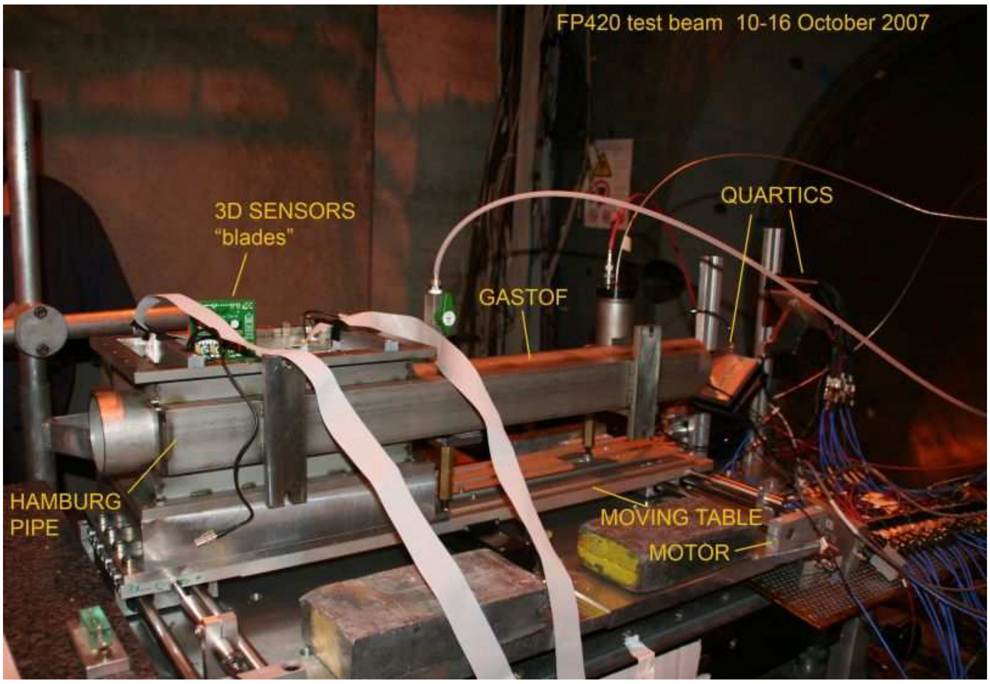

Figure 3.4: Photograph of the prototype beam-pipe section used in the October 2007 CERN test beam.

it adds complexity to the control system, reduces reliability, and increases cost. Positioning accuracy and reproducibility are also reduced because extremely high precision guiding systems can no longer be used, due to the necessary additional angular degree of freedom. Therefore, a single motor drive system has been chosen, accompanied by two precise LVDTs.

3.3.3 Beam position monitors and alignment

The reconstruction of the proton momentum depends in principle only on the optics of the two beamlines and the position of the silicon sensors relative to the beam. In practice, however, the magnet currents will vary from fill to fill, and the fields in the magnets will vary accordingly. The AFP collaboration considered two independent alignment strategies. One is to use a physics process detectable in the ATLAS central detector which produces proton tracks in the detectors of known energy. This strategy is independent of the precise knowledge of the LHC optics between the IP and the detectors and is described in the physics chapter. It will also be necessary to have a real-time alignment system to fix the position of the detectors relative to the beam and provide complementary information to the off-line calibration using tracks.

An independent real-time alignment system is also essential for safety purposes while moving the detectors into their working positions. Two options, both based on Beam Position Monitors (BPMs), are being considered: a 'local' system consisting of a large-aperture BPM mounted directly on the moving beampipe and related to the position of the silicon detectors by knowledge of the mechanical structure of the assembly, and an 'overall' system consisting of BPMs mounted on the (fixed) LHC beampipe at the two ends of the system, with their positions and the moving silicon detectors' positions referenced to an alignment wire using a Wire Positioning Sensor (WPS) system. Figure 3.5 shows schematically the proposed 'overall' alignment subsystem. To simplify the illustration only one moving beam pipe section is shown. The larger aperture BPMs for the 'local' alignment system are not shown (one would be mounted on each moving beam pipe section). It is likely that both the local and overall BPM alignment schemes will be implemented.

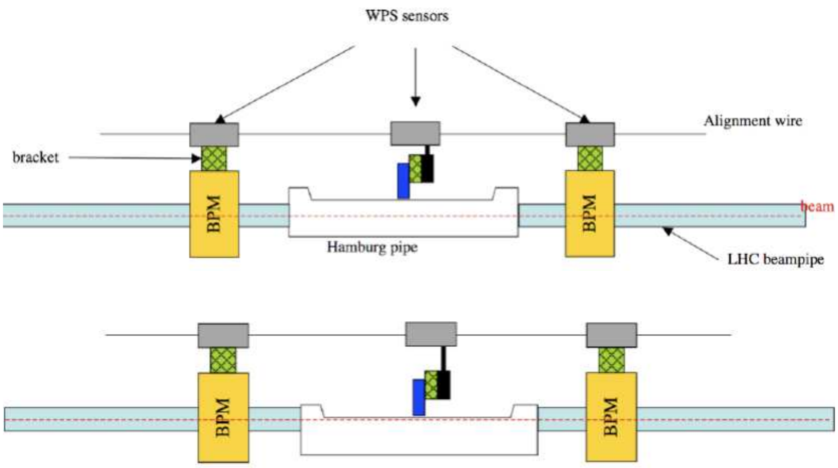

Figure 3.5: The proposed overall alignment system, shown with detectors in garage position (top picture) and in operating position (bottom picture).

Sources of uncertainty in such a system include the intrinsic resolution of the WPS system, the intrinsic resolution (and calibration) of the BPMs, and the mechanical tolerances between the components. The mechanical uncertainties may be affected by temperature fluctuations and vibrations in the LHC tunnel, and the movement of the detectors relative to the beam must be taken into account. The individual components of the system, with comments on their expected accuracy, are described in the following subsections.

Beam position monitors

A direct measurement of the beam position at the detector positions can be obtained with beam position monitors (BPMs). Although there are several pickup techniques available, an obvious choice would be the type used in large numbers in the LHC accelerator itself. The precision and accuracy of these electrostatic button pickups can be optimized through the choice of electrode geometry and readout electronics. While BPMs can be made with precision geometry, an important issue is balancing the gain of the right and left (or up and down) electronics; one can have a time-duplexed system such that the signals from opposing electrodes are sent through the same path on a time-shared basis, thus cancelling any gain differences. Multiplexing of the readout chain will avoid systematic errors due to different electrical parameters when using separate channels and detuning through time and temperature drift. Preliminary tests with electrostatic BPMs designed for the CLIC injection line have shown promising behavior on the test bench, even when read out with general purpose test equipment. More details can be found in [24].

Although the requirements are not as demanding for the LHC as for ATLAS FP, it is our expectation that the necessary level of precision, resolution and acquisition speed can be obtained. It should be emphasized that the precision will depend to a large extent on the mechanical tolerances which can be achieved. Several strategies and optimizations have been proposed to reach precision and resolution of a few microns, and to achieve bunch-by-bunch measurement. This is being developed by the LHC machine group.

Multi-turn integration will improve the resolution at least by a factor 10. Bunch/bunch measurements will still be possible since the bunches in LHC can be tagged, allowing measurements of each bunch to be integrated over a number of turns. The variation of one specific bunch between turns is expected to be small.

Shortly before the installation of each complete ATLAS FP section (with trackers and BPMs) a test-bench survey using a pulsed wire to simulate the LHC beam will provide an initial calibration of the BPMs. Further in-situ calibration can be done by moving each BPM in turn and comparing its measured beam position with that expected from the measurements in the other BPMs in the system; the potential for success of such an online BPM calibration scheme has been demonstrated with cavity-style BPMs intended for use in linear colliders [26, 27]. Such calibration may even be possible at the beginning and end of data-taking runs when the BPMs are being moved between garage and operating positions, removing a need for dedicated calibration runs.

Wire positioning sensors)

Wire Positioning Sensor (WPS) systems use a capacitive measurement technique to measure the sensors' positions, along two perpendicular axes, relative to a carbon-fibre alignment wire. Such systems have been shown to have sub-micron resolution capability in accelerator alignment applications and will be used in LHC alignment. The principle of operation is shown in Fig. 3.6. Photographs of a sensor (with cover removed) and of two end-to-end sensors are shown in Fig. 3.7.

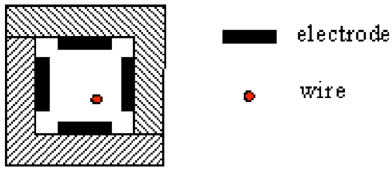

Figure 3.6: A cross-sectional schematic of a WPS sensor and alignment wire.

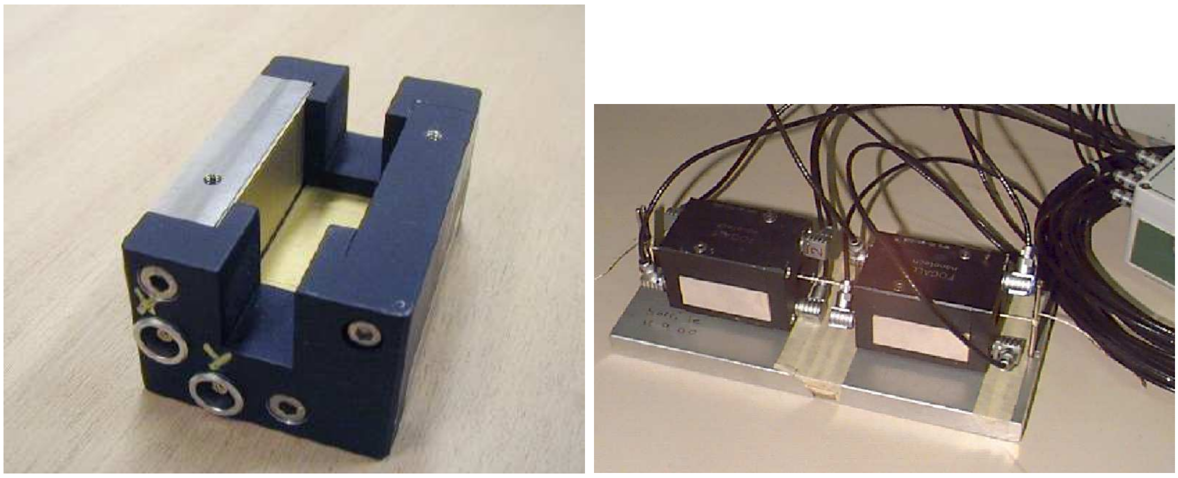

Figure 3.7: A WPS sensor with lid removed (left), showing the electrodes. The aperture is 1cm square. Also shown are two WPS sensors on the test bench (right).

3.4 System performance and operation

The baseline prototype of the moving beampipe was prepared for use in test beam at CERN in October 2007. Figure 3.4 shows the one-meter long beam-pipe equipped with two pockets, one of 200 mm length for the pixel detector and the other of 360 mm length for the gas Čerenkov timing detector. The vacuum window thickness was 0.4 mm. A detector box for the 3D detectors was mounted in the first pocket. The moving pipe was fixed on a moving table, driven by a MAXON motor and guided by two high precision linear guides. The relative position of the moving pipe was measured with two SOLARTRON LVDT displacement transducers, which have 0.3 μm resolution and 0.2% linearity. The magnitude of the deformation of a 600 mm long pocket, measured by FP420 [24], was less than 100 μm. The shorter pockets planned for the final design is expected to yield significantly less deformation.

The AFP detectors incorporated into the beam pipe will operate at all times in the shadow of the LHC collimators in order to guarantee low background rates and to avoid detector damage from unwanted beam losses. Therefore, the high-level Hamburg pipe control system will be integrated into the collimator control system. The interface between low- and high-level controls will be implemented using the CERN standard Front End Standard Architecture (FESA) [25].

The LHC Control Room will position the detectors close to the beam after stable collisions are established. The precision movement system will be able to operate at moderate and very low speed for positioning the detectors near the beam. During insertion and while the detectors are in place, rates in the timing detectors will be monitored, as well as current in the silicon. The step motor and LVDT's will provide redundant read-back of the position of the detectors and fixed and moveable BPM's will provide information on the position of the detectors with respect to the beam.

3.5 Machine induced backgrounds and RF effects

The safe distance of approach of the detectors to the beam depends on the beam conditions, machine-induced backgrounds, collimator positions and the RF impact of the detector on the LHC beams. Detailed studies have been performed and the machine-induced background from near beam-gas and betatron cleaning collimation was found to be small. A reevaluation of this background is planned based on early LHC data. Extensive simulation and laboratory studies were carried out to test the impact of the Hamburg pipe on the LHC impedance budget [24]. The designs described above were found to have a negligible impact on the LHC impedance budget at 420 m, and similar results are expected for the 220 m region.

3.6 Ongoing research and development

After the Technical Proposal has been accepted by the ATLAS Collaboration we can begin the final design phase of the Hamburg pipe. At this point we will repeat impedance studies using the final design and the 220 m optics. We envisage that a joint ATLAS/CMS safety review committee will be instituted together with LHC Vacuum group to assess all safety issues related to the project. This safety review will validate the details of the final design of the Hamburg Pipe mechanics.

3.7 Conclusions

The Hamburg moving pipe concept provides the optimal solution for the 220 m detector systems at ATLAS. It ensures a simple and robust design and good access to the detectors. Moreover, it is compatible with the limited space available at 220 m needed to host both the silicon tracking detectors and the timing detectors. Its reliability is linked to the inherent absence of compensation forces and the direct control of the actual position of the moving detectors.

The detectors can easily be incorporated into the pockets, which are simply rectangular indentations in the moving pipes. The prototype detector pockets show the desired flatness of the thin windows, and the first motorised moving section, with prototype detectors inserted, has been tested at the CERN test beam. This was a first step in the design of the full system, including assembling, positioning and alignment aspects.

It should be noted that the Hamburg pipe design, development, and prototyping was performed with the direct knowledge of the LHC cryostat group. In particular, the Technical Integration Meetings (TIM), held regularly at CERN and chaired by K. Potter, provided an efficient and crucial framework for discussions and information exchanges. Similar meetings would re-commence after the Technical Proposal is approved by ATLAS.

Chapter 4

The Silicon Tracking Detector

4.1 Introduction

The silicon tracker system is the heart of the ATLAS Forward Proton detector system. Its purpose is to measure points along the trajectory of beam protons that are deflected at small angles as a result of collisions. The tracker when combined with the LHC dipole and quadrupole magnets, forms a powerful momentum spectrometer. Silicon tracker stations will be installed in Hamburg beam pipes at ± 216 and ± 224 m from the ATLAS IP as discussed in the previous chapter. To reconstruct the mass of the central system produced in ATLAS, it is necessary to measure both the distance from the beam and the angle of the proton tracks relative to the beam with high precision, so beam position monitors (BPM's) are integrated into the Hamburg pipe system.

The smallest distance at which sensors can approach the beam to detect the scattered protons determines the minimum fractional momentum loss (ξ) of detectable protons. The 220 m stations are designed to track protons with fractional momentum losses in the range $0.02 < \xi < 0.2$. For events in which both protons are tagged this corresponds to a range of central masses from a few hundred GeV to beyond one TeV. With a typical LHC beam size at 220 m of $\sigma_{beam} \approx 100$ μm, the window surface of the Hamburg pipe can theoretically safely approach the beam to $15\times\sigma_{beam} \approx 1.5$ mm. The window itself adds another 0.2 mm to the minimum possible distance of the detectors from the beam, and any dead region of the sensors should clearly be kept to a minimum. Placing the sensors a few millimeters from the beam imposes high demands on the radiation hardness, the radio frequency pick-up in the detector and the local front-end electronics.

4.2 Tracking system requirements

The key requirements for the silicon tracking system at 220 m are listed below:

- Spatial resolution of ~ 10 (30) μm per detector station in x (y)
- Angular resolution for a pair of detectors of about 1 μrad
- High efficiency over an area of 20 mm $\times$ 20 mm.
- Minimal dead space at the edge of the sensors
- Sufficient radiation hardness

- Capable of robust and reliable operation at high LHC luminosity

The required position and angular resolution is obtained from the tracking studies and is consistent with a mass resolution of ~ 5 GeV. Figure 4.1 shows that an area of about 20 mm $\times$ 20 mm is needed to have full acceptance for scattered protons given that the detector is located 2 to 3 mm from the beam axis.

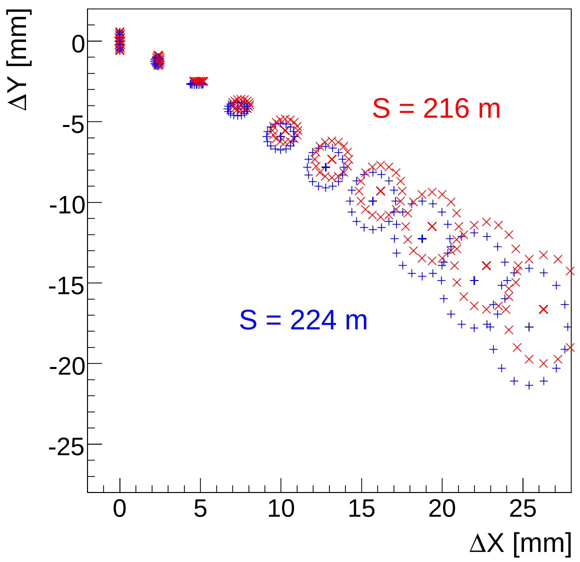

Figure 4.1: The displacement in x and y for scattered protons from the nominal beam axis which is placed at $(x, y) = (0, 0)$. Moving from left to right, different ellipses correspond to increasing values of ξ, the centers of ellipses correspond to $t = 0.0$ GeV^2, while the ellipses correspond to $t = 0.5$ GeV^2. The red symbols show the results for the station at 216 m, the blue symbols for the station at 224 m from the IP. The largest value of ξ is given by the LHC apertures in front of the stations.

4.3 Tracking system design

The basic building block of the AFP detection system is a module consisting of an assembly of a sensor array, on-sensor read-out chip(s), electrical services, data acquisition (DAQ) and detector control system (DCS). The module will be mounted on the mechanical support with embedded cooling and other necessary services. The module concept and its mechanical size are essentially determined by sensor granularity dictated by physics requirements and the read-out chips employed.

4.3.1 The silicon sensor

The 2008 AFP Letter of Intent [1] had 3D sensors coupled to FE-I3 readout chips as the default silicon option due to the high radiation tolerance and small inactive regions. Since then the Manchester group leading the 3D option has been forced to halt work on AFP due to funding issues. There have also been significant R&D programmes into 3D and planar sensors for the Insertable B layer (IBL) project [28], which has a similar time scale and requirements. Finally, the Prague group involved in the project brings significant planar silicon expertise and resources. We thus are exploring all the different sensor options and outline them below:

3D sensors

Different ways to manufacture 3D sensors have been investigated and the two proposed for IBL are called "double-sided" [29, 30] and single sided "full3D" with active edges [31, 32] (see Fig. 4.2). Prototypes for both methods have been manufactured and characterized with FE-I3 readout electronics over the past three years with and without magnetic fields and for fluences expected for the IBL and beyond [33, 34]. The electrode configuration chosen for the IBL is called "2n-250". This means that 2 n-type electrodes will be used to span the 250 μm readout pitch [35]. This configuration has an inter-electrode distance of $\approx$ 70 μm and, for the IBL radiation dose, is a good compromise between signal efficiency and capacitive noise increases with the number of electrodes per pixel.

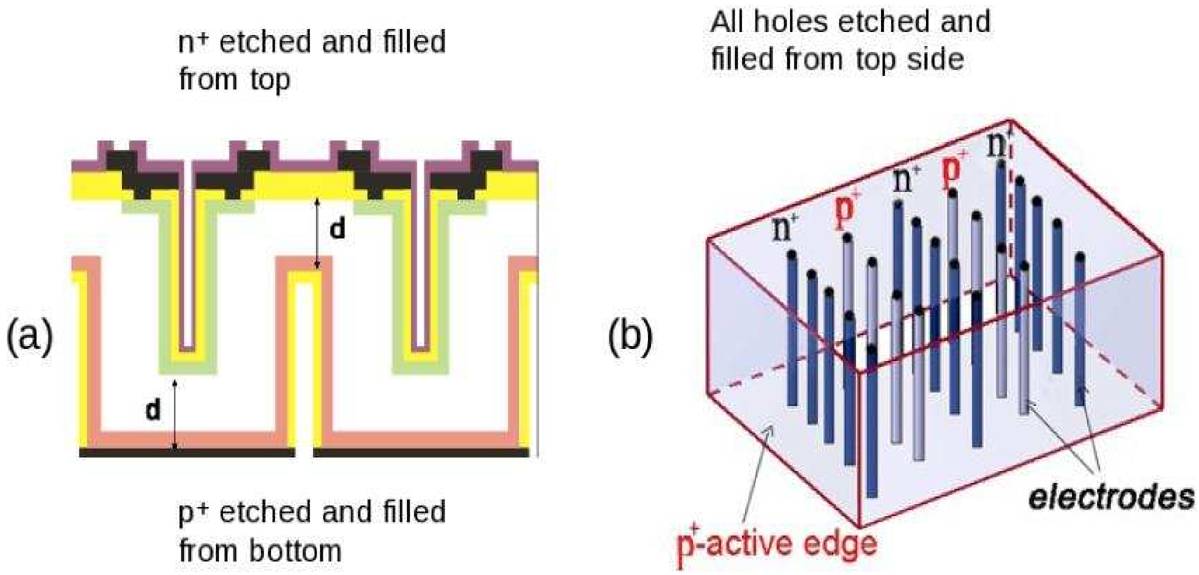

Figure 4.2: Double sided process (a) and full 3D with active edges (b). An un-etched distance d of order 20 μm is needed in (a) for mechanical integrity.

The signal efficiency for both methods measured with infrared photons and minimum ionizing particles is shown in Fig. 4.3 a), while the expected most probable signal for a substrate thickness of 230 μm is shown in Fig. 4.3 b). The results for the 3E-400 configuration shown in Fig. 4.3 have been obtained using the FE-I3 chip. Due to the larger readout pitch of the FE-I3 chip the 3E-400 configuration corresponds to the 2E-250 configuration chosen for the IBL.

Thanks to a relatively short charge collection in 3D sensors the required bias voltage is low even in over-depletion, both before and after irradiation, and consequently the power dissipation is reduced. The 3E-400 operating bias voltages are 80 V before irradiation, 120 V at 5×10^{15} n/cm^2, and 180 V at 2×10^{16} n/cm^2 fluences. Besides the demonstrated high radiation tolerance, another strong feature of the 3D sensors is the active edge. A dead region close to the sensor edge of size of a few microns is achieved by etching a trench around the sensor physical edge and by diffusing in dopants to make an electrode. The electrode center is not fully efficient and hence to increase the efficiency, the sensors need to be tilted. The efficiency with a 3200 e$^-$

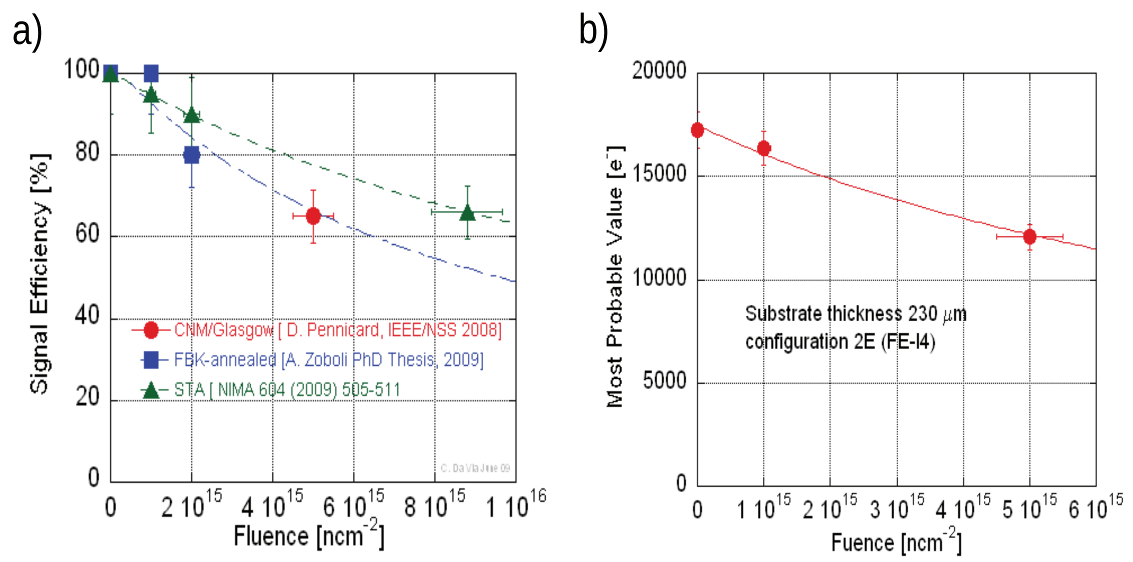

Figure 4.3: (a) Signal efficiency of double sided (CNM and FBK data points) and full3D (STA data points) 3E-400 electrode configurations. (b) Expected most probable signal for a 2E-250 electrode configuration, based on an averaged signal efficiency value from left. All sensors are 230 μm thick.

threshold is 96% at normal incidence and 99.9% at 15° from normal.

Planar sensors

There are three types of planar sensors under consideration:

conservative n-in-n design

This option (Fig. 4.4 a)) is closest to the current design of the present ATLAS Pixel detector [36] which has been proven to function reliably. By reducing the number of guard rings from 16 (current ATLAS Pixel sensor) to 13, one can reduce the inactive region to 450 μm. It has been shown experimentally that this would typically exceed the full depletion voltage by more than 150 V. The pixel length in y has to be reduced to 250 μm to match the y-size of the FE-I4 pixel. The n-in-n technology requires double-side processing. The main advantage of this option is the proven reliability.

slim-edge n-in-n design

The guard rings of the n-in-n design are placed on the p-side of the sensor, and therefore it is possible to shift them inwards, leading to a partial overlap with the outermost pixel row (see Fig. 4.4 b)). This has the advantage of reducing the inactive region to about 200 μm. This shift distorts the field close to the sensor edge, but from simulations [37] the effect is expected to be negligible after irradiation because most of the charge is collected directly below the pixel implant due to partial depletion and trapping. The signal efficiency at the edge still needs to be studied in test beam. The overall sensor design is identical to the conservative design above.

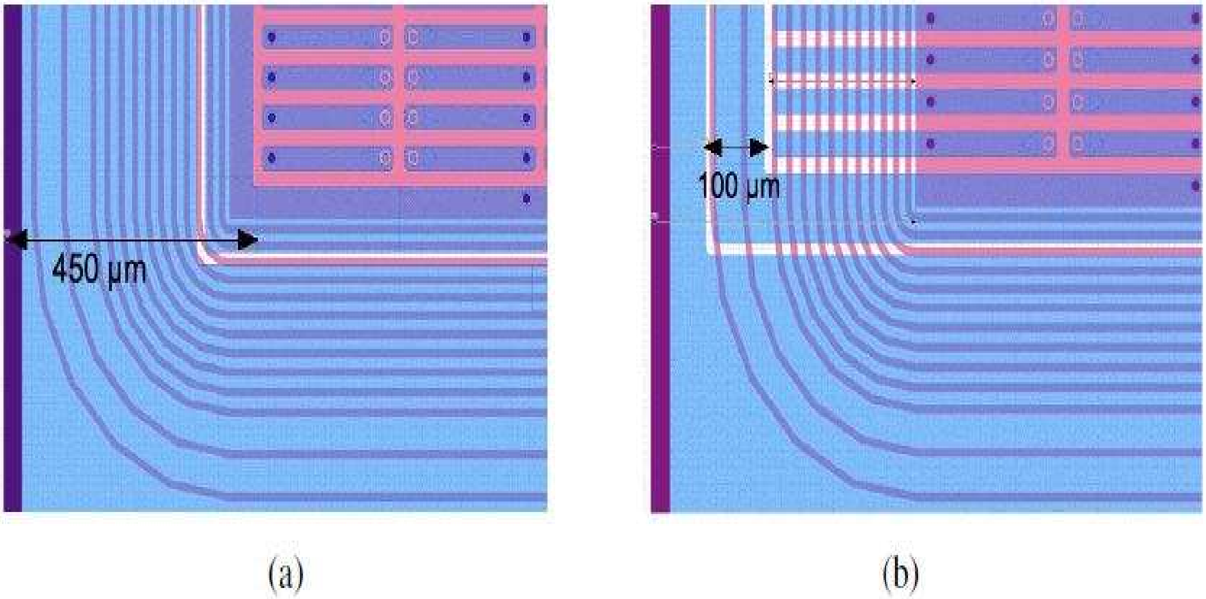

Figure 4.4: a) Conservative n-in-n sensor design. b) Slim-edge n-in-n sensor design.

thin n-in-p design

Sensors made on p-bulk are an interesting alternative to the more complex double-sided n-bulk sensors. The n-in-p technology is a choice for future strip upgrades replacing the hole-collecting p-in-n technology which performs poorly after high fluences. Therefore a significant R&D program is taking place within the ATLAS Upgrade environment in collaboration with leading semiconductor manufacturers. The n-in-p technology is being tested by all LHC experiments as well as by the RD50 Collaboration [38]. Performance before irradiation measured with the FE-I3 chip is equal to that of n-in-n sensors. While tests before irradiation showed a sufficient protection, the behaviour after the irradiation is still being investigated. n-in-p sensors offer, in addition to the large number of vendors capable of producing them, easier methods for thinning. A handle wafer method [39] has been developed to process n-in-p sensors down to thicknesses of below 100 μm. Good performance before and after irradiation has been achieved on FE-I3 compatible pixel sensors produced with this technique [40]. The inactive region can also be reduced to 450 μm with this technique [40] (see Fig. 4.5).

Sensor conclusions

The 3D sensors have full active edges, which is critical for maximizing the light mass acceptance for the 220/420 m AFP configuration, but is of less import for this 220 m Stage 1 proposal. We note that the IBL decision is expected in June, and even though they are at the TDR stage and are attempting to install in 2013, the sensor choice has not been fully determined, so we are deferring this decision for now. There would be certain advantages to choosing the same technology as the IBL, although their requirements for active edges are more modest.

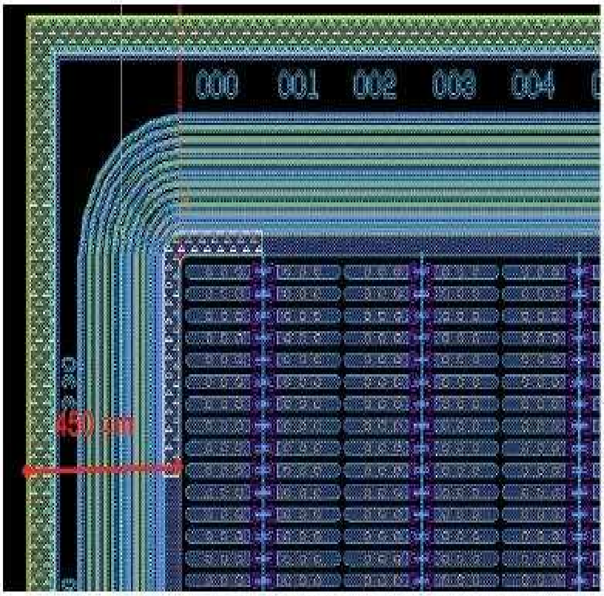

Figure 4.5: n-in-p Sensor design. The number of guard rings is chosen to meet the IBL limit of a 450 μm inactive edge.

4.3.2 The readout chip

The present ATLAS pixel detector [43, 44, 45] is read out by the FE-I3 chip which contains 2880 readout cells of 50 μm $\times$ 400 μm size arranged in a 18 $\times$ 160 matrix. This system is currently functioning extremely well. For ATLAS tracking upgrades, starting with the IBL, the new front-end chip FE-I4 has been developed. The FE-I4 integrated circuit contains readout circuitry for 26 880 hybrid pixels arranged in 80 columns on 250 μm pitch by 336 rows on 50 μm pitch, and covers an area of about 19 mm $\times$ 20 mm. It is designed in a 130 nm feature size bulk CMOS process. Sensors must be DC coupled to FE-I4 with negative charge collection.

The FE-I4 is very well suited to the AFP requirements: the granularity of cells provides a sufficient spatial resolution, the chip is radiation hard enough (up to $\sim 10^{15}$ n$_{eq}$ cm^{-2}), and the size of the chip is sufficiently large that one module can be served by just by one chip. This significantly simplifies the design of the AFP tracker, as no special tiling arrangement is needed.

Each pixel contains an independent, free running amplification stage with adjustable shaping, followed by a discriminator with independently adjustable threshold. The chip keeps track of the firing time of each discriminator as well as the time over threshold (TOT) with 4-bit resolution, in counts of an externally supplied clock, nominally 40 MHz. Information from all discriminator firings is kept in the chip for a latency interval, programmable up to 256 cycles of the external clock. Within this latency interval, the information can be retrieved by supplying a trigger.

Recent IBL discussions indicate that slightly modified FE-I4b chip will be ideally suited to the IBL and AFP. This has the major advantage in that AFP can take full advantage of the IBL development effort.

4.3.3 Location and layout

The stations are proposed to be placed at $\pm$ 216 m and $\pm$ 224 m from the ATLAS interaction interaction point (IP). Two alcoves close to the stations (20 m cables) can house the readout electronics crates that collect signal from the stations, send the trigger data to the Central

Trigger Processor (CTP) and receive the signal back from the CTP.

Each tracking station will consist of five layers of sensors each read out by a single FE-I4 chip. The mechanical design awaits a final sensor determination.

4.4 System performance and operation

To maximize the acceptance for low momentum-loss protons, the detectors should be active as close to their physical edge as possible, this inactive area will range from a few microns for the 3D option to 0.5 mm for standard n-in-n and n-in-p options, due to the sequence of guard rings, which control the potential distribution between the detectors sensitive area and the cut edge to remove leakage current.

The dimensions of the individual cells in the FE-I4 chip are 50 μm $\times$ 250 μm in the x and y directions, respectively. Therefore to achieve the required position resolution in the x-direction of $\sim$ 10 μm, five layers with sensors are required (this gives $50/\sqrt{12}/\sqrt{5} \sim 7$ μm in x and roughly 5 times worse in y). Offsetting planes alternately to the left and right by one half pixel, will give a further reduction in resolution of at least 30%, which should easily meet the performance goals.

4.4.1 Electromagnetic environment

The detectors have to be shielded against the electromagnetic environment in the tunnel by a Faraday cage. The readout chip should be robust with respect to beam-induced EM interactions, power supply noise, ground fluctuations close to the chip inputs, etc. Therefore on-chip pedestal subtraction or proper pulse processing (pulse shaping, double correlation) prior to the threshold decision is required.

4.4.2 Radiation tolerance

The innermost layer of the ATLAS pixel detector is expected to be exposed to a fluence of about 3.0×10^{14} 1 MeV neutrons per cm^2 (n$_{eq}$ cm^{-2}) per year at the full LHC luminosity of 10^{34} cm^{-2}s^{-1} corresponding roughly to a dose of 200 kGy per year. A fluence of 1.0×10^{15} n$_{eq}$ cm^{-2} corresponds to roughly five years of running LHC at full luminosity. Results from test beams with the silicon pixel sensors in the ATLAS [46] and CMS [47] detectors show that the detection efficiency may be kept above 95% for fluences lower than $\sim 10^{15}$ n$_{eq}$ cm^{-2} if the irradiated sensors are operated at sensor bias of 600 V (non-irradiated sensors are normally operated at 150 V) and the pixel electron threshold are lowered.

Results obtained by the RD50 Collaboration with miniature n-in-p strip detectors (1×1 cm^2) using 40 MHz clock rate electronics have shown that, even after 2×10^{16} n$_{eq}$ cm^{-2} planar sensors can yield signal charge equal or even greater than before irradiation [41, 42]. The key feature to achieve large signal charge after heavy irradiation is high electric field, which for typical sensor thickness means operating at bias voltages well in excess of 1000 V. However, thin detectors can achieve high electric fields with lower voltages. Figure 4.6 shows the charge collection vs. dose in 300 μm sensors limited to 900 V. It can be seen that without relying on either on kV range bias or thin sensors, the MIP signal charge for planar sensors after 5.0×10^{15} n$_{eq}$ cm^{-2} is approximately 8000 electrons.

Concerning the 3D-silicon sensors, as can be seen from Fig. 4.3 b), after 5.0×10^{15} n$_{eq}$ cm^{-2} the most probable signal is 12000 electrons.

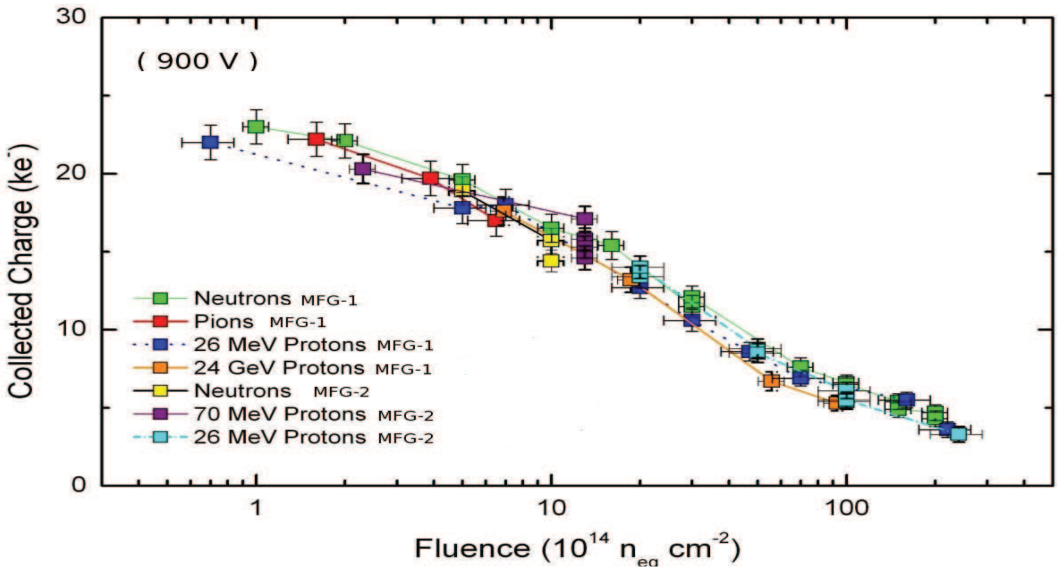

Figure 4.6: Collected charge as a function of fluence up to $2\times\ 10^{16}$ n_{eq} $cm^{-2}$with planar sensors made by two different manufacturers (MFG) biased to 900 V.

4.4.3 Cooling

The operation of silicon detectors at low temperature (∼140 K) limits the leakage current allowing a low depletion voltage. The experience with the ATLAS pixel detector shows that it is sufficient to only cool the readout electronics whilst keeping the sensors at room temperature. Until proper thermal tests are done we assume that the detectors will be cooled to a moderate 5°C.

There are three different cooling approaches under considerations based on experience obtained during development of the detector cooling systems for the ATLAS Inner Detector and the TOTEM detectors. The three options, outlined below, are being tested with simulated heat loads ranging from hundreds to a thousand watts:

1. The modified cooling system, which is based on the TOTEM project solution. The selection of this option depends on the available space for the plant.
2. The thermosiphon cooling system (prototype under development).
3. The Vortex-based Dry Air Cooling System (DACS). A laboratory-scale prototype is available with power up to 500 kW per cooling unit with a possibility to manipulate cooling air temperature between -40° and -10°.

The choice of the coolant for the first two systems was based on its dielectricity, thermodynamic characteristics and its radiation hardness, and is oriented towards fluorocarbon fluids, namely C_3F_8. Technology of such systems is well tested and understood. Nevertheless, unavoidable difficulties with these options are the expected large distance between the cooling plant and the targets (detector plus electronics) to be cooled down, resulting in rather long refrigerant pipelines. The third solution is the preferred one, as its small size and use of dry air as coolant allows for local placement next to the detector and electronics. Tests with realistic AFP detector engineering mockups are envisaged. These should include design supports with integrated cooling channels respecting the geometrical layout of the equipment.

4.5 Ongoing research and development

Once the sensor choice is made, the mechanics and cooling will be developed, and prototypes will be built and tested.

4.6 Conclusion

Although the final sensor choice has yet to be made, the switch from the FE-I3 to FE-I4 readout chip has dramatically simplified the silicon tracker design for the 220 m region. Given that the sensor choice is made within the next few months, the other issues (mechanics, cooling, etc.) will naturally fall into place and there will be sufficient time for prototyping, production, and installation, of the 5-plane AFP silicon detector system (four of these are needed to fully instrument the 220 m region). Using the same readout technology as the IBL project enables us to forgo extensive R&D with its concomitant costs and manpower requirements.

Chapter 5

Fast Timing System

5.1 Introduction

Overlap background due to multiple proton-proton interactions in the same bunch crossing will become prevalent at the LHC as the instantaneous luminosity increases. Much of this background can be removed by kinematical matching between the central system as measured by the central detector (for example, jets from Higgs decay), and inferred from the protons measured in the AFP silicon detectors. For rare processes, the background may still be too large to make a significant measurement, motivating the fast time-of-flight detector. Consider an event with a central massive system and two oppositely directed small angle protons. If the protons are from the same interaction as the central system, the position of the vertex as measured by the central tracks will be consistent with the position as determined from the time difference of the outgoing protons. A time resolution of 10 ps corresponds to a 2.1 mm vertex position resolution, which given the approximately 5 cm width of the luminous region and the 50 μm uncertainty of the central vertex will yield an additional rejection factor of about 20 against this fake background.

5.2 Timing system requirements

The final timing system should have the following characteristics

- 10 ps or better resolution
- acceptance that fully covers the proton tracking detectors
- efficiency near 100%
- high rate capability (O(10) MHz/pixel)
- segmentation for multi-proton timing
- Level 1 trigger capability
- radiation tolerant
- robust and reliable

For the first stage, 220 m at modest luminosity, the requirements are not quite as stringent: 20 ps resolution will suffice, the rate should not exceed 2 MHz/pixel, and the Level 1 trigger capability is not strictly necessary.

5.3 Timing system components

The main components of the timing system are: i) the detector comprised of the radiator that produces light when a proton passes through it and the photo-sensitive device that converts the photons into an electrical pulse; ii) the electronics system that reads out the pulse and interfaces with the ATLAS data acquisition and trigger system; and iii) the reference timing system that provides a low jitter clock signal allowing the correlation of the detector stations which are hundreds of metres apart. Below we describe each of these components.

5.3.1 The detectors

Typically high energy physics time-of-flight detectors have a resolution of about 100 ps [48], an order of magnitude worse than our requirements. Recently spurred by a sub-10 ps measurement obtained in Ref. [49], the focus for dramatically improving time-of-flight resolution has turned towards detectors employing a quartz Cerenkov radiator coupled with a microchannel plate photomultipier tube (MCP-PMT).

We note that the detector design of Ref. [49] does not suit our needs, since it requires putting the MCP-PMT directly in the beam. Over the past several years, we have studied Cerenkov detectors with gas (GASTOF) and quartz (QUARTIC) radiators [50, 24, 1]. For 7 TeV protons, Cerenkov radiation is emitted along a cone with an angle defined by the Cerenkov angle $\theta_c \approx \cos^{-1}(1/n)$, where n is the index of refraction of the radiator.

Figure 5.1(a) shows a schematic diagram of the QUARTIC detector, which consists of four rows of eight 5 mm $\times$ 5 mm quartz or fused silica bars ranging in length from about 8 to 12 cm and oriented at the average Cerenkov angle ($\sim 48^\circ$ for quartz). Any proton that is sufficiently deflected from the beam axis will pass through one of the rows of eight bars, providing eight independent time measurements along the track. Photons are continuously emitted as the proton passes through the bars; those emitted in the appropriate azimuthal angular range are channeled to the MCP-PMT.

Figure 5.1(b) shows a schematic diagram of the GASTOF detector. It has a gas radiator at 1.3 bar in a rectangular box of 20 to 30 cm length, with a very thin wall adjacent to the Hamburg pipe pocket. The protons are all essentially parallel to the axis. A thin 45° concave mirror at the back reflects the light to an MCP-PMT. The gas used in tests is C_4F_8O, which is non-toxic and non-flammable, and has a refractive index of $n = 1.0014$ giving a Čerenkov angle ($\beta = 1$) of 3.0°.

Figure 5.1(c) shows a schematic of an MCP-PMT which consists primarily of a photocathode and microchannel plates. The photo-cathode converts the radiation to electrons, and the MCP's, which are lead glass structures with an array of 3 to 25 micron diameter holes (pores), serve as miniature electron multipliers converting the incoming photons to a measurable signal for the downstream electronics. Phototubes under consideration for QUARTIC Stage 1 are the Photonis Planacon a 64 channel 2 inch square tube with either 10 or 25 μm pores, or the Hamamatsu SL10 a 16 channel 1 inch square tube with 10 μm pores, while a Photek 210 single channel 1 cm tube with 3 μm pores or a Hamamatsu R3809U-50 with 6 μm pores are the leading candidates for GASTOF.

The AFP R&D effort has focussed on the QUARTIC detector, which is segmented and thus meets the requirements of Sec. 5.2 better than the GASTOF detector. The QUARTIC longitudinal segmentation provides multiple measurements of the same proton, reducing the necessary precision for any single measurement to 30 to 40 ps, while the transverse segmentation provides the ability to measure multiple protons in the same detector. It is also useful to have a GASTOF, however, since it makes one excellent measurement (better than 20 ps), and has

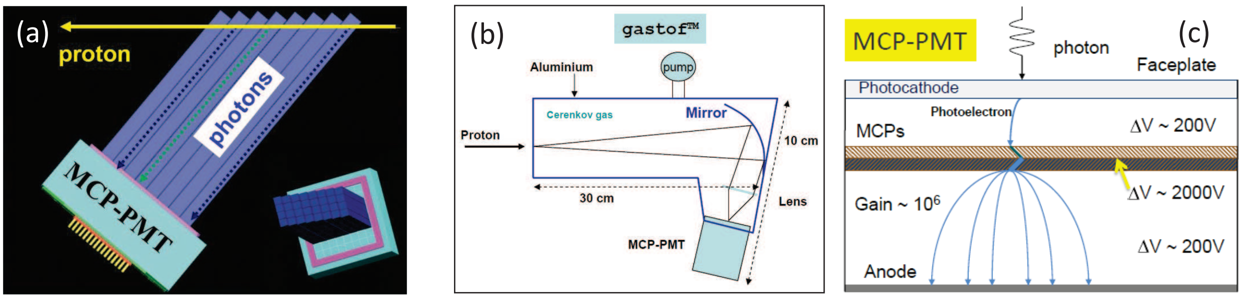

Figure 5.1: (a) A schematic side view of the proposed QUARTIC time-of-flight counter, which shows Cerenkov photons being emitted and channeled to the MCP-PMT as the proton traverses the eight fused silica bars in one row. The inset shows a rotated view with all four rows visible. (b) A schematic view of the proposed GASTOF time-of-flight counter. (c) A schematic view of an MCP-PMT as described in the text.

minimal material so does not cause significant multiple scattering. It can therefore be placed between the tracking detectors without degrading the performance of the final tracking station.

5.3.2 The electronics

The electronics system is designed to provide a 20 ps resolution measurement of the time-of-flight of protons scattered at small angles, provide a Level 1 trigger, and record the time measurements in the ATLAS data stream. The electronics are optimized for the QUARTIC detector, which makes multiple measurements in the 30 ps range, but can also be used for GASTOF, which makes a single measurement in the 10 to 20 ps range. Figure 5.2 presents a schematic overview of the electronics system and includes photos of the primary constituents: pre-amplifiers, constant fraction discriminators, trigger, and high precision time-to-digital converters (HPTDC). The reference timing system, which provides a stable clock signal, is described in Sec. 5.3.3.

Pre-amplification. Due to the high proton rate (up to 10 MHz in the row closest to the beam), the MCP-PMT gain should be as low as possible to maximize the device lifetime, consequently we use a $\times 50$ pre-amplification. Tests have been performed using two $\times 10$ Minicircuits 8 GHz ZX60 amplifiers in series, separated by a $\times 2$ attenuator and a diode to protect the second amplifier from large signals in the case of shower events. Although a bandwidth of 1–2 GHz would suffice for a typical multi-anode MCP-PMT (with a rise time of about 400 ps), we did not find an amplifier in this bandwidth range that had the desired gain as well as low noise (1 dBm) and reasonable cost ($50 per channel).

For the final detector electronics we will replace the ZX60 with a 3mm $\times$ 3mm Minicircuits QFN low profile surface mount pre-amp, and incorporate this and the other discrete components on a PCB board that will plug directly onto the MCP-PMT.

Constant fraction discriminator. The amplified signals will then be sent via several metre long high speed coax cables to the constant fraction discriminator (CFD) boards located in a readout crate installed in a shielded region near the tunnel wall. The CFD system is based on a design developed by the University of Louvain for FP420 [24] with a NIM unit mother board that filters the NIM power and houses 8 single channel CFD daughter boards. These provide a NIM output for testing and an LVPECL output to the HPTDC board that digitizes the time. The final system may be VME based instead of NIM, and will also form a trigger signal prior to being digitized.

Trigger. A coincidence of several CFD channels in the same row can be used to form a

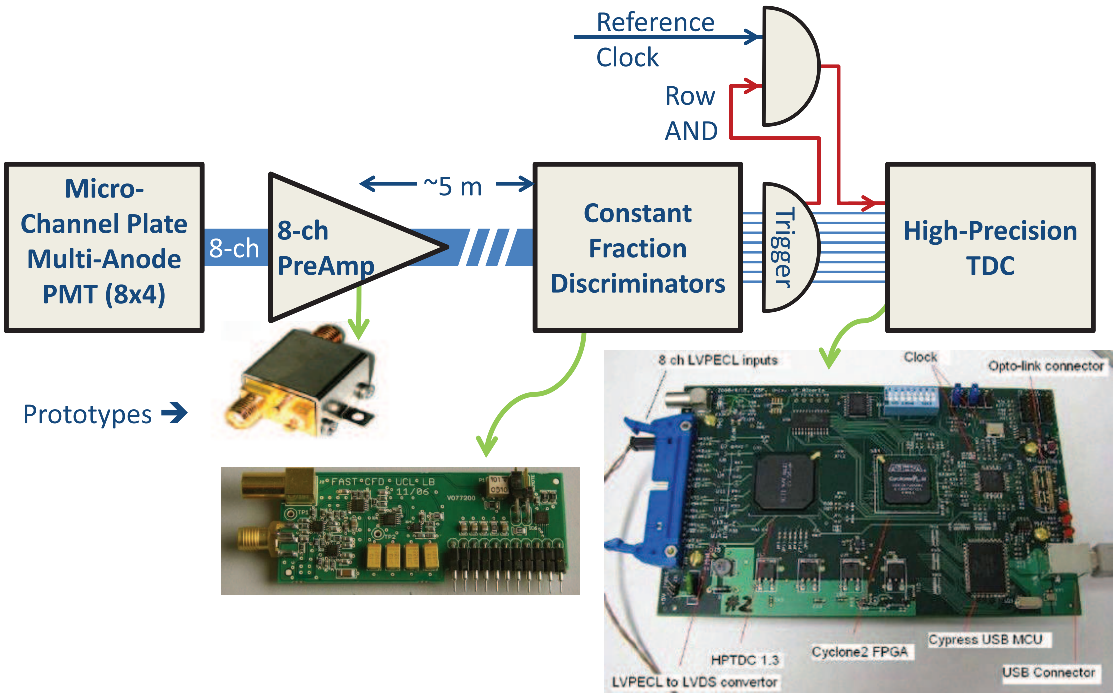

Figure 5.2: A schematic diagram of the electronics chain described in the text. The photographs show a low noise Minicircuits ZX60 pre-amplifier, a constant fraction discriminator daughter board, and the HPTDC board used in laser and beam tests.

trigger. The row triggers can be ORed to form a global trigger that can be sent to Level 1 on a dedicated large diameter air core cable. This global trigger would be satisfied when a proton passes anywhere through the detector. A more sophisticated trigger could be formed in a second Stage of AFP after the L1 Cal upgrade, by correlating the row trigger with the calorimeter η to chose events in a specific mass range. In addition to providing a global trigger, the row triggers can be used to limit the occupancy of the HPTDC board by only passing on the CFD signals for events that pass a multiplicity cut within a row. These row triggers will also be used to filter the reference clock signal, such that the clock signals are only passed to the associated HPTDC chips when the row in question has a proton passing through it. This trigger logic must preserve the channel timing resolution and should introduce a jitter of less than 5 ps.

HPTDC board The filtered CFD and clock LVPECL signals are sent to the HPTDC board via ribbon cable. This board uses the 25 ps least bit 8-channel HPTDC chip developed by CERN for the ALICE Time-of-Flight detector [51]. Our HPTDC board also includes control signals and an optomodule which interfaces to the existing ATLAS Readout Driver (ROD). Our studies indicate that if operated in the standard 8-channel high resolution mode (25 ps least bit), the occupancy of the HPTDC board will eventually exceed 2 MHz causing a loss of data. Simulations show that by doubling the internal clock speed to 80 MHz and using only four channels per chip, the occupancy limit can be increased to 16 MHz at less than 0.1% losses. This capability is satisfactory for our expected maximum 10 MHz trigger rate, and using the filtering described above will also reduce the rate of the reference timing signal to acceptable levels.

5.3.3 Reference clock

The final component of the time-of-flight system is the reference clock used to tie together measurements hundreds of metres apart. Practically, this is done by taking the time difference with respect to a stabilized clock signal. For the clock signal to cancel in the time difference it must have a jitter of 5 ps or less, or it would not be negligible relative to the proton time resolution. The reference timing stabilization circuit is based on a design developed at the Stanford Linear Accelerator Center (SLAC) by Joe Frisch and Jeff Gronberg (LLNL). It uses a phase locked loop feedback mechanism as shown in Fig. 5.3(a). A voltage controlled oscillator (VCO) launches a signal down the cable from the tunnel near the proton detector to the interaction point (IP), where it is reflected and sent back. At the IP end of the cable the signal is sampled with a directional coupler where it is compared in the mixer with the 400 MHz Master Reference, provided in this example from the LHC RF signal. The result is a DC voltage level that is fed back to the VCO to maintain synchronization. Changes in the cable's electrical length cancel when the original and returned signal are added. A high quality large diameter air core coaxial cable was used with a 476 MHz RF signal for preliminary tests (the LHC RF is 400 MHz, so minor modifications are needed to adapt the SLAC design), and the stabilization circuit yielded a 150 fs jitter over a 100 m cable. Figure 5.3(b) shows results from a second test, with a 300 m cable, which was left outside to verify the temperature stability of the circuit. A low noise amplifier was used to boost the return signal to recover the cable and power coupling losses, which are a function of cable length (the measured attenuation was about 7.5 dB for the 300 m cable). The unstabilized circuit was observed to have a variation of 80 ps/10 degrees C, while the stabilized circuit (shown in the figure) reduced the variation to 4 ps/10 degrees C. A residual correction as a function of temperature could reduce this drift to the 1 to 2 ps level, but we propose to control the temperature of the electronics, which is likely the cause of the residual variation. This should bring the drift to the sub-picosecond level along with the jitter. This temperature stabilization is important for us since the seasonal variation in the LHC tunnel is about ± 10 degrees C.

The stabilized 400 MHz RF wave will then be converted to a 40 MHZ square wave that will provide an input signal to the trigger board, such that the clock will be provided to the HPTDC only for triggered events. This is necessary to keep the HPTDC occupancy below 15 MHz.

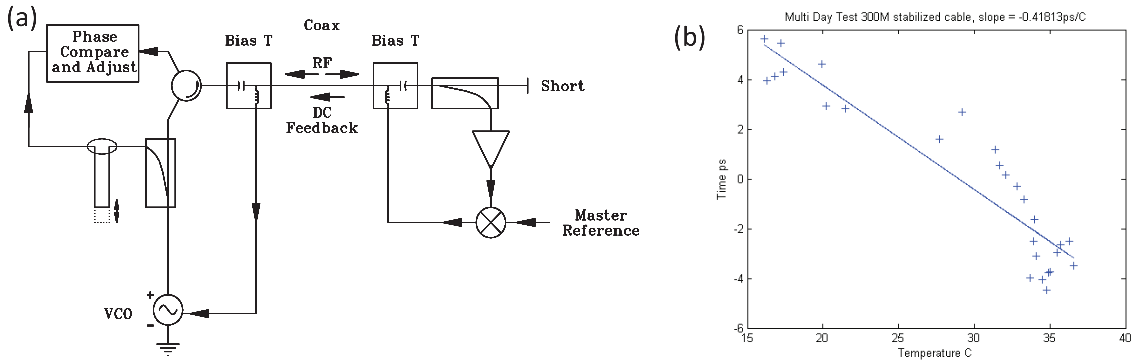

Figure 5.3: (a) Schematic of the Reference timing system as described in text.(b) Results of temperature stabilization test showing a mild drift with temperature (about 4 ps for 10 degrees C).

5.4 Timing system equipment

The Stage I timing system will consist of four 32 channel QUARTIC detectors, two on each side, totalling 128 channels. Five Photonis Planacon or ten Hamamatsu SL10 MCP-PMTs (including spares) will be required to read this out. The natural unit of the electronics is eight channels based on the number of pixels in each row of the Planacon, so we will need 16 amplifier boards, trigger boards, and HPTDC boards. Including the possibility of a two-channel GASTOF detector for each side and two spares, brings the quantity of electronics boards to 20. The infrastructure will consist of high voltage for the MCP-PMT's (CAEN 1491 or similar, one module required per side plus a spare), low voltage for the amplifiers (12 V filtered), five VME crates (two per side plus a spare), and cables. The reference timing system will consist of two transmitter boxes, two receiver boxes, and one 300 m high quality cables per side. Including a Level 1 trigger cable and a spare for each side brings the total to six high quality cables. We imagine the ROD's will be accounted for elsewhere.

5.5 Timing system performance

We have extensively studied the proposed QUARTIC detector, using simulations, beam tests, and laser tests.

Figure 5.4 (reprinted from the Letter of Intent) shows data from a 2008 CERN test beam run with (a) the time difference between between two 90 mm long QUARTIC bars interfaced to a Photonis Planacon with 10 μm pores and read out by the constant fraction discriminator described above, and (b) the efficiency across the width of a bar. The time difference has an rms of about 56 ps, corresponding to 40 ps per bar (assuming the bars are equivalent and uncorrelated), while the efficiency is seen to be uniformly greater than 95% across the bar. The test beam data are consistent with 10 generated photoelectrons per bar confirming expectations from detector simulations.

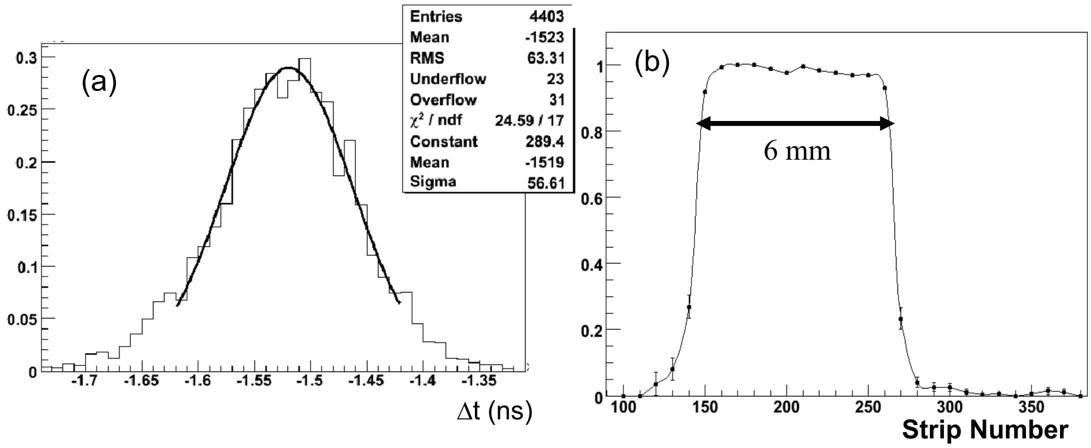

Figure 5.4: (a) The time difference between two 90 mm long QUARTIC bars described in text. (b) the fraction of track events that have a valid time in a QUARTIC bar, as a function of silicon strip number.

Since the 2008 test beam most of the performance testing has been using a pulsed 405 nm laser at the UTA Picosecond Test facility. In this setup we replace the light from the detector with light from the laser, allowing us to explore in a controlled environment all aspects of the system from the MCP-PMT through the electronics. We have obtained a CFD resolution of better than 5 ps, assuming that the pulse is sufficiently amplified (typically we amplify the pulse to ensure an average pulse height of about 500 mV; pulses above 250 mV have very little residual timing dependence on pulse height after using the CFD). We have obtained an HPTDC resolution of about 14 ps, consistent with pulser tests done at Alberta. The 15 ps overall contribution from the CFD/HPTDC is quite acceptable given our overall goal of 30 ps/channel.

Figure 5.5(a) shows a key result from the laser tests, namely that the timing for the 10 μm pore 64 channel Photonis Planacon tube has very little gain dependence for gains as low as 5×10^4. This result is obtained for a laser setting with 10 pe's, the working point of the QUARTIC detector. The validation of low gain running is important as the main technical issues regarding MCP-PMTs are rate and lifetime concerns, both of which are reduced by a factor 20 compared to operation at the canonical 10^6 gain.

Figure 5.5(b) shows the relative gain as a function of calculated output current for our working point. We note for a laser frequency of 5 MHz (last point), corresponding to a calculated current of about 0.4 μA over a 0.2 cm^2 pixel, there is about a 60% gain reduction due to saturation of the pores which have a 1 ms recovery time. For the two previous points, corresponding to the expected maximum rates for Stage 1 of 1 to 2 MHz, the gain is only reduced by 20 to 40%. If the amplification is augmented sufficiently, the timing resolution is observed to be independent of this saturation. This is within a factor of 10 of our expected maximum rate, and this final factor can be attained with a high current version of the Photonis tube already developed, thus meeting our maximum rate needs. We also note that this single channel result (closed circles) is unchanged when fibers are plugged into all eight pixels in a row (open triangles). demonstrating that saturation is a local effect.

More recent test beam data (Fermilab November 2010) using a better constructed single row prototype detector with a 25 μm Planacon yield better results. Figure 5.6 (a) shows the time difference as measured with a LeCroy 8620a oscilloscope of the CFD pulse from two non-adjacent bars. Although this MCP-PMT has inferior intrinsic time resolution due to the larger

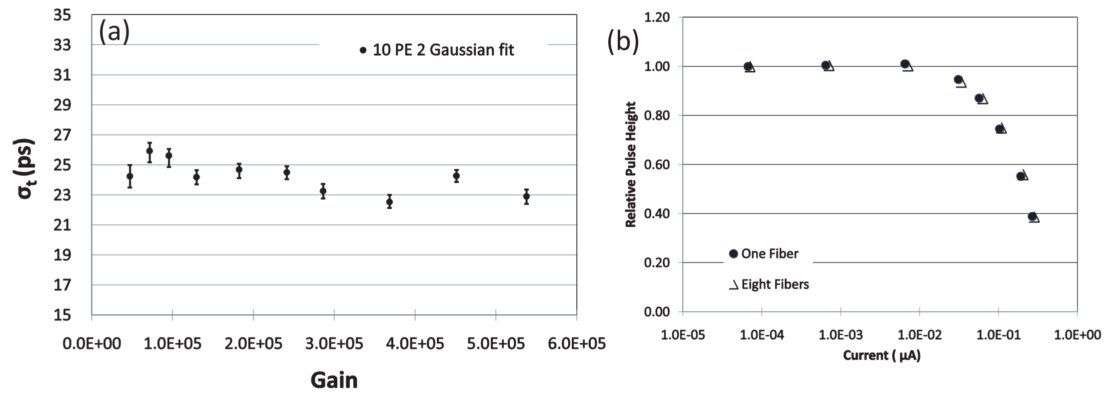

Figure 5.5: (a) Timing resolution versus gain and (b) the relative gain versus current (solid circles with one pixel hit in a row of eight and open triangles when all eight pixels hit in a row)for the 64 channel 10 μm Photonis Planacon tube.

pore size (versus the 10 μm PMT, this is more than compensated for by the higher light yield (about 15 photoelectrons per bar) due to a higher quantum efficiency and a better constructed detector. The 46 ps width implies a single bar resolution of 33 ps including the CFD. Non-adjacent bars were chosen to minimize the correlation between channels. Figure 5.6(b) shows the time difference between a reference signal and the average time from three quartz bars. The reference signal is obtained using a quartz bar interfaced with a silicon photomultiplier (estimated to have 25 photoelectrons and a resolution of 13 to 15 ps). Taking into account the resolution of the reference signal, the 20 ps overall resolution implies that the three bar system resolution is about 15 ps (note this does not include the HPTDC resolution). Including HPTDC resolution we obtain better than 20 ps with 100% efficiency for a single 8 channel detector.

Figure 5.7 shows the time difference between two GASTOF detectors from a 2010 CERN test beam run, with $\delta t = 14$ ps (r.m.s.) implying a single detector resolution of 10 ps (measured with oscilloscope). Including the HPTDC resolution is expected to result in a better than 20 ps measurement, with some inefficiency.

5.6 Ongoing research and development

We have developed a proof-of-concept of the fast timing detector system demonstrating a sub 20 ps resolution. We expect with further minor refinements to obtain sub 10 ps resolution for the full system. We believe the current system is capable of closes to 10 ps without any major adjustments. Nevertheless, there is still R&D in progress on several fronts, although no one in AFP is currently working on the GASTOF detector.

5.6.1 Detector R&D

The detector development effort to date has demonstrated that fused silica bars produce enough light within a reasonable time range to meet our detector resolution goals. Prototype tests have just been one row (8 channels), while the final detector design needs to be refined to incorporate all the channels, and offset the two detectors to reduce the bin size and avoid “cracks” (regions of poor acceptance). We have preliminary indications that a low pass filter is somewhat beneficial to the overall resolution–less light implies worse resolution, but a narrower color range would

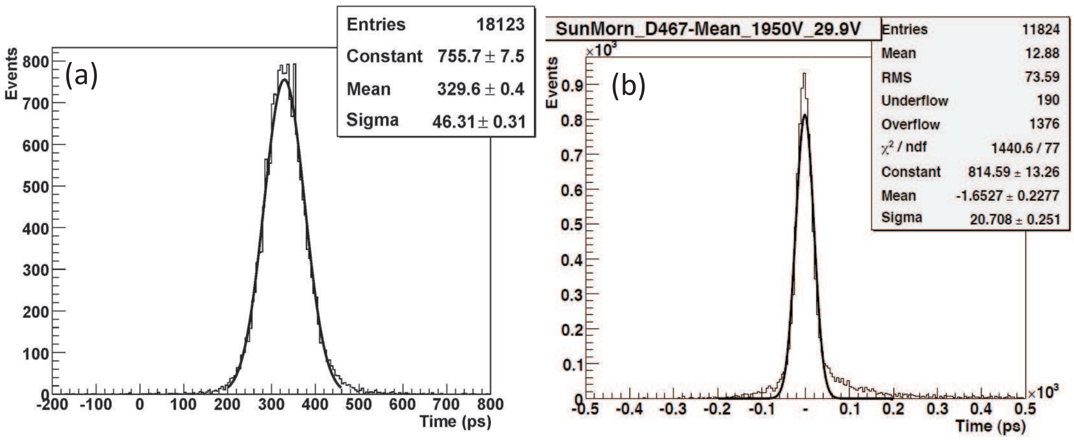

Figure 5.6: Results from November 2010 Fermilab test beam showing (a) the time difference between the CFD signal from two non-adjacent QUARTIC bars (bar 4 and 6) using the LeCroy 8620a oscilloscope (b) the time difference between a reference detector and the average time of three of the QUARTIC bars.

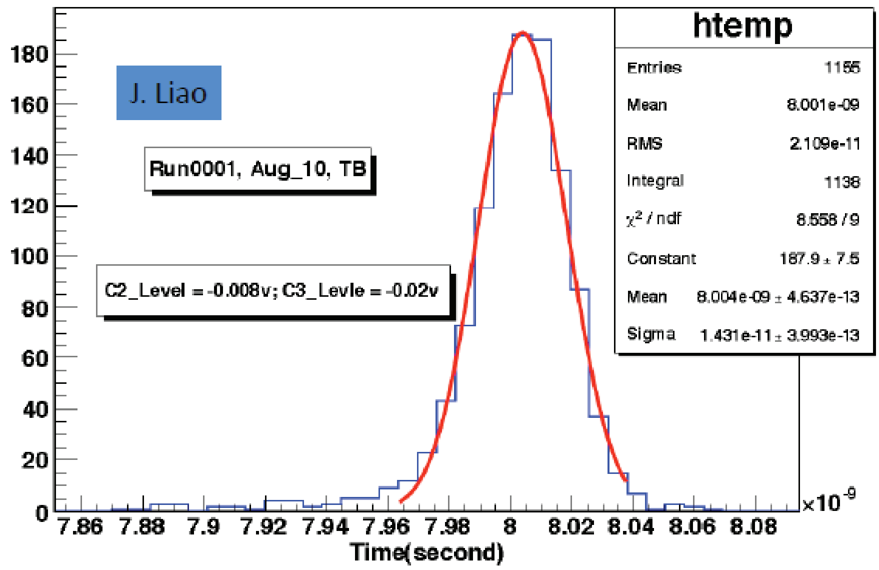

Figure 5.7: The time difference between two GASTOF detectors as described in text.

reduce the resolution broadening from color dispersion.

Another development issue is reducing the size of detector bins close to the beam, while maintaining the same MCP-PMT pixel size to equalize the rate per unit area. Not only would this improve the multi-proton timing capability (which becomes important at high luminosity, where the overlap background is worst), but it would also reduce the rate and lifetime requirements of the MCP-PMT, which are dominated by the pixels closest to the beam. Variable detector bin size could be achieved most easily with quartz fibers instead of quartz bars, and such an option is being explored by Giessen, but can also be done using quartz bars connected to fibers or channeling the light with short air light guides or Winston cones.

5.6.2 MCP-PMT R&D

A key issue is the degradation of the quantum efficiency of the MCP-PMT photocathode from back-scattered positive ions. We have estimated that at high luminosity the hottest pixels of the MCP-PMT's would receive 10 to 20 C/cm^2, which would render them unusable on a few week time scale, so development of an MCP-PMT with a 20 to 30 times longer life is essential. The standard approach to improving the lifetime is to add an ion barrier, a thin film that inhibits the flow of positive ions. The ion barrier method, originally developed for use in night vision devices [52], has been adapted for MCP-PMT's and has been observed to give at least a factor of five lifetime improvement [53]. Recent results with the Hamamatsu SL10 indicate that the lifetime is stable to several C/cm^2 which could already be acceptable for Stage 1.

UTA is working on a Small Business proposal with Arradiance and Photonis, incorporating ALD coated MCP's into the Photonis Planacon, and evaluating the lifetime. Initial results are very promising, and this approach could be used in conjunction with an ion barrier to provide the life time improvement required for Stage 2. We are also involved with Photek, another MCP-PMT vendor that is interested in making long life MCP-PMT's using a more robust "solar blind" photocathode, and could combine this with the other lifetime improvements into an Ultra long life MCP-PMT.

5.6.3 Electronics R&D

We have developed and tested a prototype of the full electronics chain, but work is still in progress here. We are developing an amplifier PCB board to replace the discrete components, and the trigger circuit must be validated. The location of the detectors close to the beam pipe but far from the ATLAS IP, requires moderately radiation-hard electronics on-detector. The location at 220 m from the ATLAS IP has expected radiation levels around 10^{12} neutron-equivalent per cm^2 at the beam pipe, decreasing with distance. At the preamplifier position, the levels are expected to be 10^{10} or less. We plan to analyze radiation monitoring data as the luminosity increases, to develop a more thorough understanding of the radiation environment of the detector. We then plan radiation studies of the amplifier board. We will test the other components as well, but not that all other electronics are located away from the beam near the tunnel wall (or in an alcove). The mechanics, grounding, and shielding will have to be studied in detail based on the final choice of MCP-PMT. We also must conduct further studies to minimize the effect of the coax signal cable runs on the timing resolution and jitter.

The existing Constant Fraction Discriminator (ALCFD) works well, but it would be beneficial to have programmable gain (or adjustable attenuation) for optimal CFD performance. We will also explore the feasibility of adding a low resolution 8 bit ADC for monitoring the MCP-PMT gain, and perhaps correcting for small or pathological pulses. We plan to route the fast timing signals to the motherboard where the fast trigger circuitry will be implemented. The fast signals, the reference time signal, and the row trigger signal will be transmitted via the analog backplane to the time digitizer modules. A dedicated VME trigger module forms the OR of all row triggers into a single-arm master trigger for transmission to the ATLAS central trigger processor.

When a trigger occurs, the high-precision reference clock signal is passed along with the row signals for digitization. The trigger logic must preserve the channel timing resolution and introduce a channel jitter of less than 5 ps. The trigger logic, although quite straight-forward remains to be designed and implemented.

We have developed and tested a single chip HPTDC board, but will need to redesign it to use 3 HPTDC chips to account for the 80 MHz internal clock as described above, which limits the chip to four useful channels, one of which is dedicated to the clock signal. Minor modifications are needed to the reference timing circuit developed by SLAC to adapt from the 476 MHz SLAC RF to the 400 MHz LHC RF, and to convert the 400 MHz stabilized clock to 40 MHz and interface it with the trigger board.

5.7 Timing personnel

The fast timing effort began as a joint ATLAS/CMS effort with Professor Andrew Brandt (University of Texas, Arlington) and Professor James Pinfold (University of Alberta) from ATLAS and Senior Lab Scientist Mike Albrow (Fermilab) and Professor Krzysztof Piotrzkowski (University of Louvain) from CMS. Brandt has been the overall ATLAS timing system leader and along with many graduate and undergraduate students has led the testing effort while Pinfold has led the electronics development and along with an electrical engineer and technicians have developed a modified version of the Louvain CFD, and the HPTDC board from scratch. Within the past two years Professors Hasko Stenzel and Michael Dueren (Giessen) have joined the effort and have been developing a fiber-based version of the QUARTIC detector, while Professor Michael Rijssenbeek (Stony Brook University) and colleagues have joined the electronics effort, and are developing the amplifier board and trigger logic.

5.8 Timing summary

We are in the process of developing an ultra-fast TOF detector system that will have a key role in the AFP project by helping to reject overlap background that can fake our signal. Tests of the current prototype detector design imply an initial detector resolution of 10 to 15 ps, including the full electronics chain. For a luminosity of $\mathcal{L} \approx 2 \times 10^{33}$ cm^{-2}s^{-1}, a 30 ps detector would be sufficient to keep the overlap background to the level of other backgrounds for the dijet channels, and render it negligible for other final states. For $\mathcal{L} \approx 5 \times 10^{33}$ cm^{-2}s^{-1}, a 10 ps detector (still with loose vertex cuts to maximise signal efficiency) would be desirable to keep overlap backgrounds totally under control, without any loss in signal efficiency. For substantially higher luminosity, we would control the background by improving the timing detector resolution to the 5 ps range and/or tightening the vertex window or other background cuts (a factor of several in rejection is possible with modest lost of efficiency).

The simplest approach to achieving faster timing is minor upgrades to current detector technologies. For the QUARTIC detector a next generation MCP-PMT with smaller pixel sizes would allow finer x segmentation for improved multi-proton timing. A smaller pore size would also be expected to give a modest improvement in the time resolution. Better electronics, such as a second generation HPTDC chip under discussion (5 to 10 ps least bit) could also give an incremental improvement and be beneficial for the GASTOF detector which is electronics-limited. Recent improvements in siPM's are promising, and we will continue R&D in this area, as well as monitor advances in other technology for possible upgrades for Stage 2.

Chapter 6

Timescale, Resources, and Conclusions

6.1 Timeline

An approximate timeline of the AFP Stage I project from now through installation assuming approval:

- *02/2011:* Document released to the ATLAS Forward Detector group
- *03/2011:* Review by Forward Detector group
- *04/2011:* Forward Detector group endorses project, project proposed to ATLAS
- *07/2011:* AFP becomes an ATLAS Upgrade Project if endorsed by ATLAS, ATLAS requests preparation of a TDR, new groups join, all attempt to procure R&D and construction funding, regular meetings with relevant CERN Accelerator groups begin
- *7–12/2011:* Development of first silicon prototype and Hamburg pipe prototype, full timing chain test in lab
- *1–6/2012:* Some new funds available, prototype development continues, beam tests, safety review, TDR preparation
- *6/2012:* AFP TDR given to ATLAS for evaluation, testing continues
- *12/2012:* Approval of AFP by ATLAS/LHCC and testing of final prototypes
- *2013:* Construction and testing of production detectors, software development
- *1–3/2014:* Installation of 220 m system

A proposal of the timescale for the project is outlined below for the different parts of the project:

- Movable beam pipe
  - *03/2011:* Meeting with CMS/LHC Vaccuum group to start getting a final movable beam pipe design.
  - *beginning 2012:* Prototype of final movable beam pipe

  - *mid 2012:* Beam tests with movable beam pipe, QUARTIC, silicon sensors
  - *starting Summer 2011:* Safety committee created together with CMS/LHC Vacuum group

- Silicon Pixel detectors

  - *en of Summer 2011:* First sensors ready - Bump-bonding of first sensors to FEI4 chips by Fraunhofer (Berlin)
  - *09/2011:* Cabling of bare modules
  - *12/2011:* First detector ready for beam tests
  - *end 2011-2012:* Alignment and support studies
  - *December 2011:* Prototype of cooling system
  - *end 2012:* Building of final detectors if beam tests successful

- Timing detectors: see the chapter on timing detectors, the design of the timing detectors is already well advanced and beam tests already occured both for QUARTIC and GASTOF

6.2 Installation

The proposal is to install the following during the 2013/2014 shutdown:

1. the movable beam pipes located at 216 and 224 m on both sides of the ATLAS detector
2. cables and fibers in tunnel connecting 220 stations to ATLAS trigger and readout
3. local cables and electronics including LV/HV and reference timing receiver box in alcove near detectors
4. QUARTIC timing detectors: two each in 224 m station after silicon
5. silicon tracking detectors (and cooling) in each of the four stations
6. GASTOF timing detector: one in each 216 m station after silicon

If for some reason only a partial system could be installed, it would be desirable to at least complete the first three items, as the last three could in principle be installed during a minor access period. If sufficient manpower and funds were added to the project (motivated by a BSM Higgs discovery in 2011 for example), the proposal could be upgraded to include installation of 420 m detectors as well on the same timescale (or during the subsequent long shutdown). This would require an updated connection cryostat design, but the rest of the detector system should be almost completely transferable.

6.3 Personnel

Due to this project's current lack of status within ATLAS, the active manpower is extremely limited. The current effort is primarily limited to timing detector R&D. Approval of the technical proposal would immediately ramp up involvement of several groups as shown in Table 1. Other groups that have expressed interest would also likely join the effort and new groups would be recruited.

Institute	Activity	Manpower Total People	Manpower FTE
Armenia	timing detectors	2	1
Czech Republic	Pixel Si detector Cooling	12	5
France, CEA Saclay	Mechanical Engineering Timing detector electronics	10	4
Germany, Giessen	Timing detectors	2	1
Poland	Power supplies	8	4
USA, Texas Arlington	QUARTIC trigger	3	1.5
USA, Stony Brook	QUARTIC	2	1.3
Alberta, Canada	QUARTIC trigger	4	2

Table 6.1: Minimum manpower forseen to be available through installation if AFP project approved.

6.4 Costing and available or requested budget

A detailed costing evaluation is in progress.

The available and requested budgets per country for the project are given in the following (please note that this is just indicative at this stage of the project):

- **Armenia:** Some money can be requested once project is approved.
- **Canada:** 70 kCHF available now for engineer/technician salaries, additional money can be requested once the project is approved
- **Czech Republic:** Money is available for wafers, FEI4 chips, n-on-p sensors (production, tests, flip-chip bonding), if this solution is chosen, as well as cooling of the Si detector
- **France:** Some funds will be available to develop Stage II fast timing electronics when the AFP project is an ATLAS project; engineers can be committed to the project (salaries paid)
- **Germany:** 50% post-doc for timing detector development now, possibility to submit a funding application to BMBF if project considered as an ATLAS project by the end of this year
- **Poland:** A grant from Polish government can be requested once the project is an ATLAS project and the MoUs are signed
- **USA:** UTA MCP-PMT development project funded ($150,000), Stony Brook Electronics technician funded ($35,000), DOE ADR submitted for timing electronics development ($173,000), other fundinf requests planned if approved.

6.5 Conclusion

This Technical Proposal has presented the Stage I plan of the ATLAS Forward Proton (AFP) upgrade: to add high precision silicon and timing detectors housed in specialized movable beam pipes at ~ 220 m upstream and downstream of the ATLAS interaction point to detect intact final state protons scattered at small angles and with small momentum loss. The detectors would be fully integrated into ATLAS forming a new proton detection capability during standard running thus enabling a rich QCD, electroweak and beyond the Standard Model experimental program. For this project to succeed, it must rapidly be declared an ATLAS upgrade project, enabling funding for the final R&D needed for the Technical Design Report. Given final ATLAS/LHCC approval by late 2012 and the procurement of sufficient funds it would be possible to install the full 220 m system in early 2014. Finally, we would like to acknowledge the tremendous work done by the UK groups which initiated this project and sadly have been forced by their funding agencies to abandon it.

Chapter 7

Appendix I: LHC physics debris collimation studies and their impact on AFP detectors acceptance

This chapter is a summary of a sLHC project note written by F. Roncarolo, R. Appleby, K. Potter, P.Bussey and C. Bracco, CERN-sLHC-Project-Note-0029.

7.1 Introduction

The ATLAS Forward Proton (AFP) group is proposing to upgrade the forward region of ATLAS by installing forward proton detectors at 220 m from the interaction point on both sides of the LHC ATLAS experiment. For this purpose, at 220 m location, it is proposed to install movable beam pipes which will host silicon tracking and fast timing detectors (i.e. four independent detector stations). The detectors are designed to operate at intermediate and high instantaneous luminosities of up to $10^{34}\ cm^{-2}s^{-1}$.

At 220 m a system similar to that developed for FP420 is proposed. The 220 m region is less demanding than the 420 m one from an engineering perspective since a cryogenic bypass is not required. However, the experimental acceptance at 220 m is dependent upon the setting of two collimators designed to protect the LHC straight section and dispersion suppressor around ATLAS (and CMS) from the physics debris generated at the two high luminosity experiments. Such two collimators (at about 140 m and 190 m from the IP) are foreseen to be in a closed position, as needed for machine protection, for luminosity higher than a few $10^{33}\ cm^{-2}s^{-1}$.

7.2 IR layout and present collimation scheme

The layout of the first 250 m on the right side of ATLAS is shown in Fig. 7.1, in which the proposed location of the AFP detectors at 220 m is indicated. The two collimators presently foreseen for operation at high LHC luminosity runs are also indicated. Throughout the note these two collimators will be labelled as TCL4 and TCL5. The location for a possible new collimator (TCL6), that will be discussed later in this note, is also indicated. For the issues discussed here, the layout of the left side of ATLAS is practically symmetric.
Both TCL4 and TCL5 are installed on the beam pipe hosting the LHC beam that emerges from ATLAS, after the beam pipes divided. TCL4 has been designed to protect the separation dipole D2 from physics debris and also the first matching section quadrupole Q4 and possibly other

downstream magnets. TCL5 has been designed to protect Q5 and possibly other superconductive elements down to the dispersion suppressor (DS) at about 400 m. TCL5 was proposed in the year 2000, before any proposal for a TCL4, and the details can be found in [54], where the authors proved with simulations the need for the protection of Q5 and estimated the beneficial effects of TCL5 in terms of beam losses reduction in the DS region. At the end of their note, they assess the need for a TCL4 collimator without presenting detailed studies. The TCL5 studies were performed using the LHC optics Version 6.1 and the presented results give as 15 σ_x a convenient collimator half gap for guaranteeing the LHC protection.

Given the TCL4 and TCL5 interference with the proposed AFP physics, the availability of

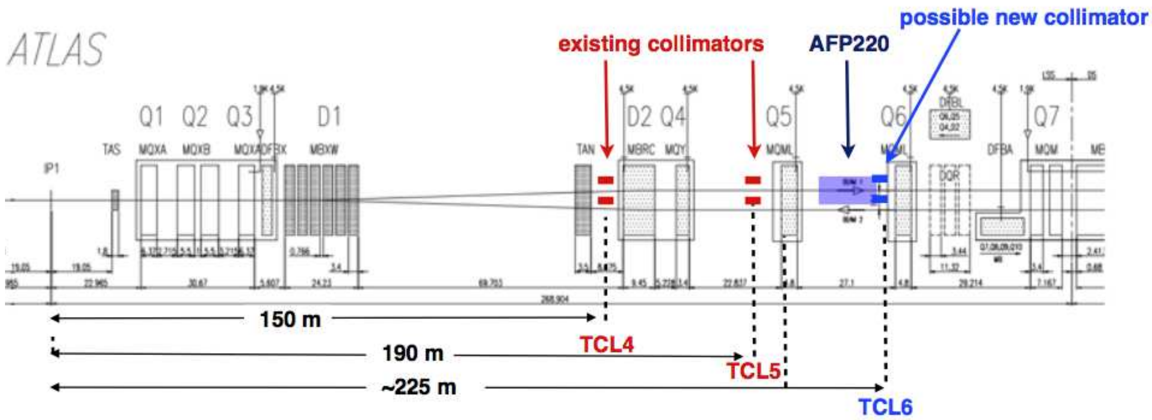

Figure 7.1: Layout of the straight section on the right side of ATLAS.

the new LHC optics Version 6.503 and the lack of information about the TCL4 effectiveness, the AFP collaboration decided to carry out a new study in order to investigate a physics debris protection scheme that allows safe LHC operation as well as full forward protons acceptance at 220 m. In the following sections, we present the result of analytical considerations accounting for the new LHC optics and of numerical simulations aimed at generating beam loss patterns for different collimation settings.

7.3 Optimal collimator settings as studied with beam optics calculations

According to linear beam dynamics, the transverse motion of particles has two amplitude terms. The betatronic one is described by the betatron functions $\beta_{x,y}(s)$ variation along the accelerator structure. A second term is proportional to the particle momentum offset with respect to the reference momentum dp/p, with the dispersion function $D_{x,y}(s)$ as proportionality factor. Considering the horizontal plane, the maximum excursion of a particle with momentum offset dp/p as function of location s is equal to:

$$x_{max}(s) = \sqrt{\beta_x(s)\epsilon_x + \left[\frac{dp}{p} \cdot D_x(s)\right]^2}, \tag{7.1}$$

where ϵ_x is the geometric horizontal emittance describing the particle mapping of the horizontal phase space. The horizontal trajectories of a 7 TeV proton and of three off-momentum protons (with $dp/p = -1 \cdot 10^{-3}, -1 \cdot 10^{-2}$ and $-1 \cdot 10^{-1}$ respectively), as calculated with PTC [55] using the MADX LHC optics V6.503, are shown in Fig. 7.2. Since in all four cases the tracking starts at IP1 with (x,x',y,y') = (0,0,0,0), there is no betatronic contribution and the particle deviation from the reference orbit is only due to the energy dependent term of Eq. 7.1.

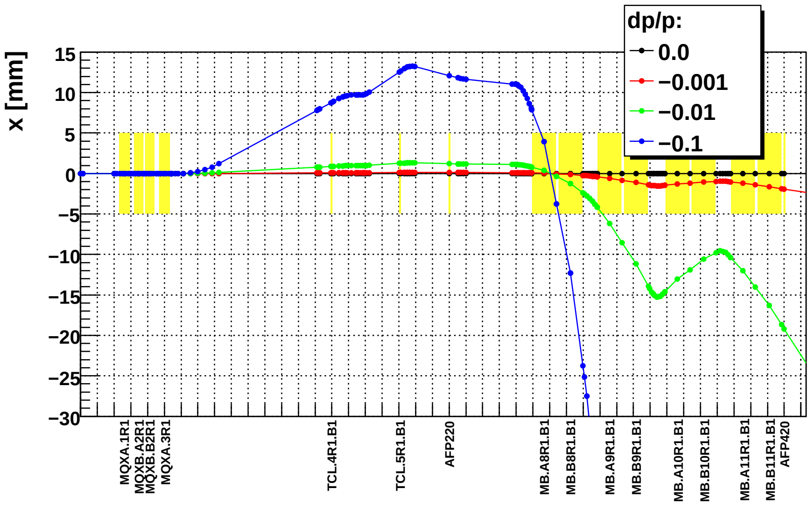

Figure 7.2: Horizontal trajectory of a 7 TeV proton and of three off-momentum protons, as simulated with PTC. For all particles the initial coordinates are at (x,x',y,y') = (0,0,0,0).

Assuming a collimator at a location $s = s_c$ with a full gap centered around the reference beam closed orbit, it is possible to determine the minimum collimator half gap ($x_c(s)$ *or* $y_c(s)$) necessary to intercept a particle with momentum offset dp/p. Considering the horizontal plane, such a quantity defined in units of the betatronic beam size $\sigma_x(s) = \sqrt{\epsilon_x \beta_x(s)}$ results:

$$\frac{x_c(s)}{\sigma_x(s)} = \frac{D_x(s)}{\sigma_x(s)} \cdot \frac{dp}{p} = \frac{D_x(s)}{\sqrt{\beta_x(s)\epsilon_x}} \cdot \frac{dp}{p} = \frac{1}{\epsilon_x} \cdot D_x^n(s) \cdot \frac{dp}{p}, \tag{7.2}$$

where $D_x^n(s) = D_x(s)/\sqrt{\beta_x(s)}$ is called the *normalized dispersion* function. The normalized dispersion and the collimator half gap, as defined in Eq. 7.2, are shown in Fig. 7.3 and Fig. 7.4 respectively, for the two LHC beams outgoing from IP1. It must be noted that in this case D_x is the *unmatched* dispersion function (different from the periodic lattice dispersion) accounting for the fact that protons experience a $D_x = 0$ at the location where they are generated (the IP). The necessary collimator half gap has been plotted for three values of the proton momentum offset with respect to 7 TeV ($dp/p = 2 \cdot 10^{-2}, 5 \cdot 10^{-2}$ and $10 \cdot 10^{-2}$) that cover the range of particles that needs to be intercepted in order to minimize the risk of quenching superconductive elements in the long straight sections and dispersion suppressors. The location of the two existing collimators (TCL4 and TCL5) and of a possible additional collimator (TCL6) are indicated. As an example these calculations indicate that, for intercepting a proton with $dp/p = 2 \cdot 10^{-2}$ (black line in the figure), TCL5 needs to be closed to less than $10 \cdot \sigma_x$ whereas it would be enough to keep TCL6 at about $35 \cdot \sigma_x$.

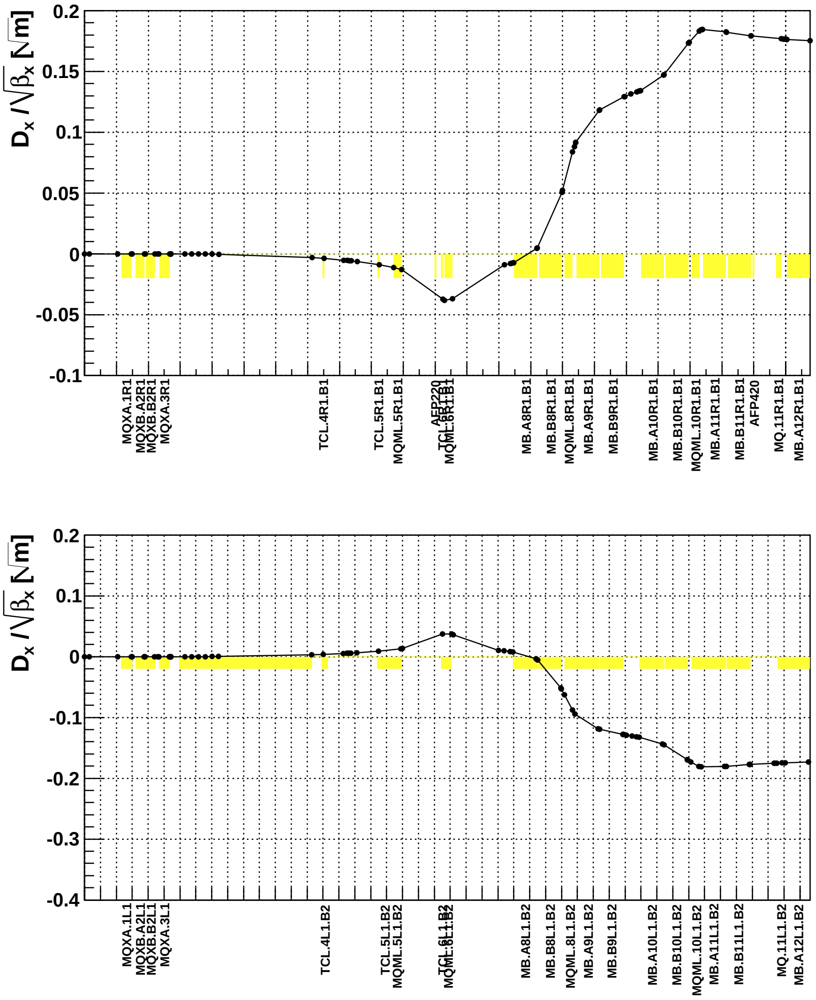

Figure 7.3: Normalized horizontal dispersion in the straight section on the right side of ATLAS for Beam 1 (top) and on the left side for Beam 2(bottom).

7.4 Numerical simulations setup

In order to confirm the analytical calculations discussed above, a set of numerical simulations have been implemented. The numerical simulations consisted in tracking distributions of protons, representing a sample of forward protons generated by p-p collisions, downstream, in the LHC straight section and dispersion suppressor. The tracking included the best available approximation of the LHC physical aperture and were performed with different collimator settings in order to evaluate the effectiveness of the machine protection. Two tracking codes have been used and compared:

- PTC (Polymorphic Tracking Code) [55], that is based on a 'thick lens' model of the accelerator elements and offers an exact Hamiltonian of the magnetic elements; in such a way the trajectory of off-momentum protons is described in the best approximation available for the LHC model; the simulations performed with PTC considered any aperture limit, including collimators, as black absorbers.

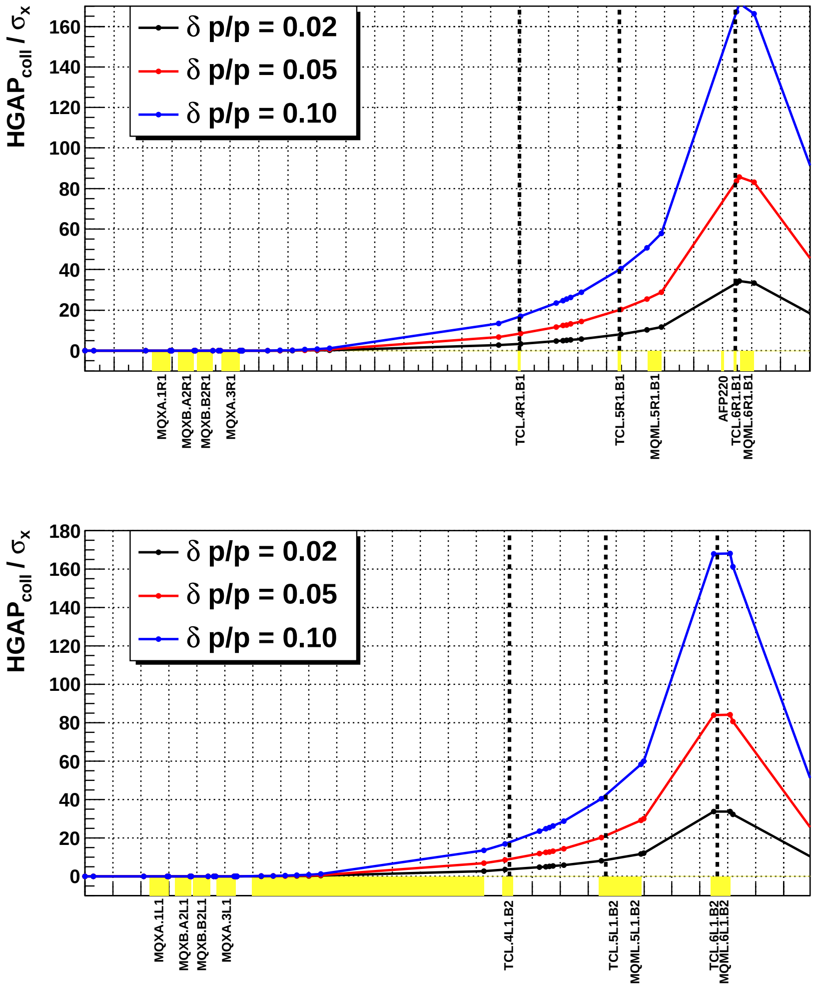

Figure 7.4: Collimators horizontal half gap necessary to intercept protons with 3 different momentum offsets as function of collimator position, for Beam 1 (top) and Beam 2 (bottom).

- SIXTRACK [56], that is based on a 'thin lens' model of the accelerator elements; in particular, a special version of the code including the COLLTRACK tools, that has been designed for fast multi-turn tracking and extensively used for designing the LHC collimation system; SIXTRACK is supposed to be less accurate in tracking protons with more than 10% momentum offset, but has the advantage of simulating elastic and inelastic scattering on the collimators. Therefore, with respect to PTC, it does not neglect the contribution of scattered protons to the losses on the downstream superconducting elements.

Both codes have been interfaced to the MADX LHC optics V6.503 and were given the same LHC aperture model. The aperture model used for the right side of IR1 is shown in Fig. 7.5. The plot covers the region from s=0 to s=230 m, even though the aperture has been modeled and considered by the tracking up to 450 m. The considered aperture model was the one available in MADX at the moment of the simulations and may well be replaced by better approximations for future studies. Despite some uncertainties (e.g. vertical aperture of experimental beam pipe before the TAS) the studies presented here focus on comparisons between different codes and different collimator settings and the results significance must be considered as unbiased.

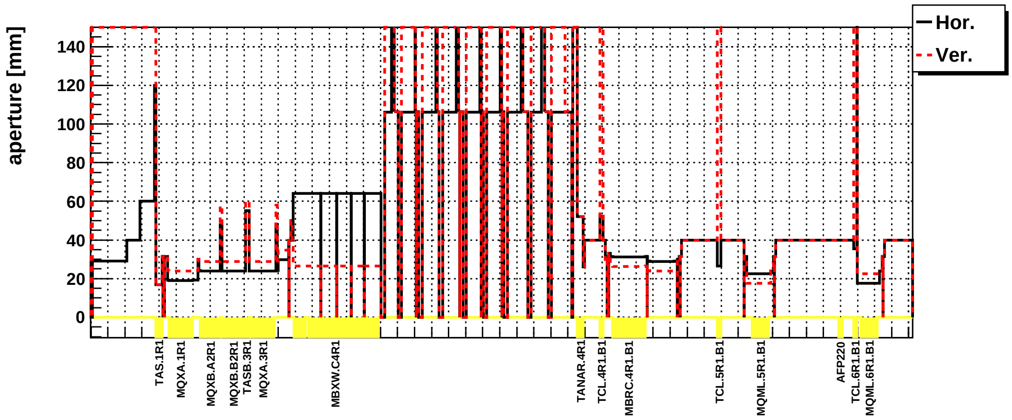

Figure 7.5: Aperture model in the first 230 m from IP1 (Beam 1), used for both the PTC and SIXTRACK simulations.

7.5 Numerical simulation results

7.5.1 PTC loss maps without collimators

For all results presented in this document, the loss maps refer to forward protons generated at IP1 and tracked along the LHC Beam 1 direction (right side of ATLAS) for 450 m in the dispersion suppressor region. For the LHC design, the majority of the DPMJET protons surviving this region will be lost in the cleaning insertions IR3 and IR7.
The first set of loss maps produced with PTC has been performed without TCL collimators installed in the lattice and the estimated number of protons per meter and per second at nominal LHC luminosity is shown in Fig. 7.6. Like in many of the figures that will be presented, the horizontal blue line at $8 \cdot 10^6\, p/m/s$ indicates an estimation of the quench level threshold for the superconductive magnets in the studied region. Such a value assumes that all protons have a momentum of 7 TeV. This approximation is the one used for all machine protection studies before the LHC provides any data.
The average momentum offset (with respect to 7 TeV) of the lost protons and the number of lost protons weighted for the proton momenta are shown in Fig. 7.7 and 7.8 respectively. The three plots yield the following considerations:

- a few peaks of Fig. 7.6 in the final focusing triplets region (s=0-80 m) exceed the estimated quench limit. However, since most of the protons lost in this region have very low momentum, all peaks fall below the quench limit when normalizing for the proton momentum, as evident in Fig. 7.8.

- the TAN absorber at about 140 m indeed intercepts a large number of forward protons as indicated by the peak reaching 10^8 protons per meter per second; but it cannot quench.

- the losses along the Q5 quadrupole at about 190 m approach the estimated quench limit and require a protection;

- the estimated losses from about 250 m to the dispersion suppressor result in an order of magnitude safety with respect to the estimated quench limit.

The calculated energy deposition expressed in Watt per meter is shown in Fig. 7.9. The values resulting form the loss maps are well in agreement with the LHC Design Report [57], stating

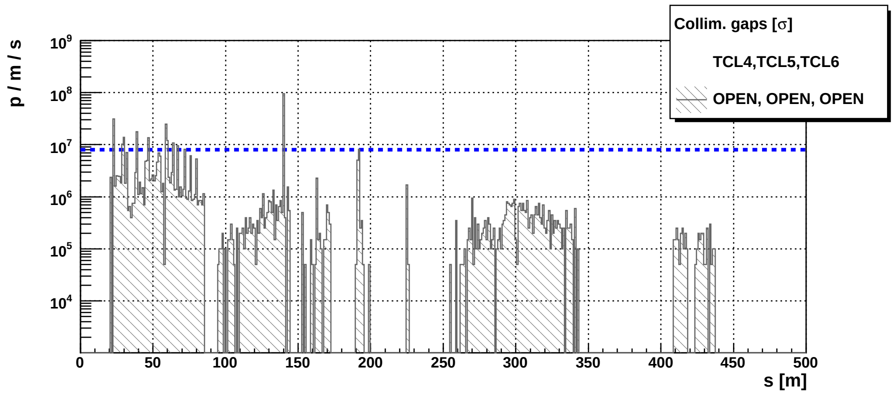

Figure 7.6: PTC loss maps with no TCL collimators installed in the IR1 straight section. The horizontal blue line indicate the estimated quench limit assuming 7 TeV protons.

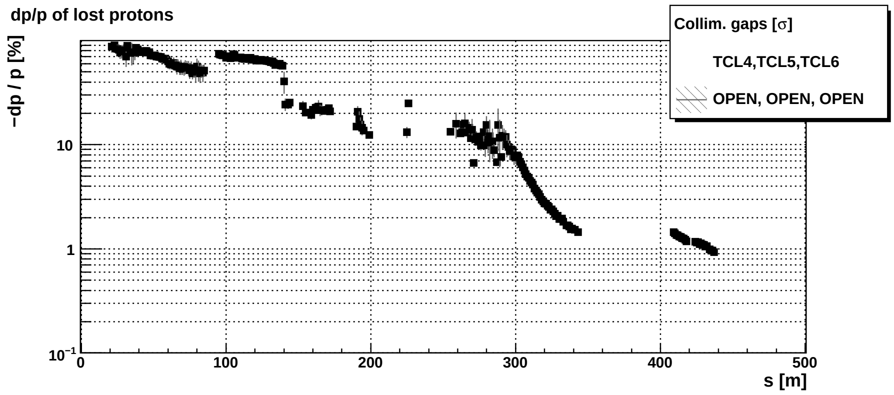

Figure 7.7: Average momentum offset with respect to 7 TeV of the protons lost according to the distribution of Fig. 7.6

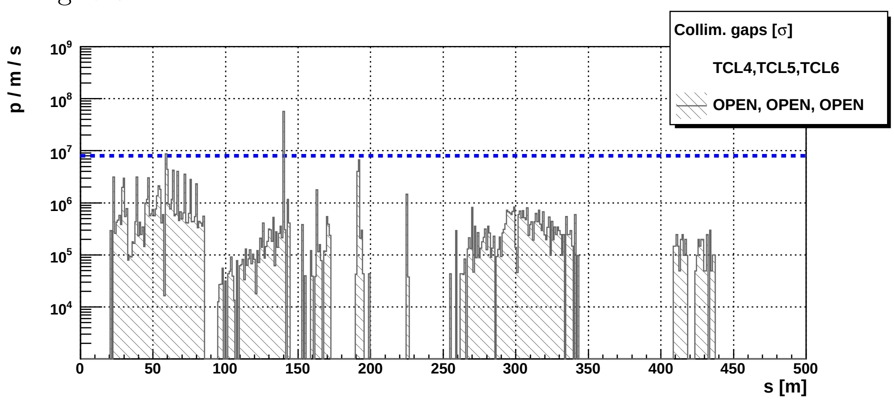

Figure 7.8: PTC loss maps with no TCL collimators installed in the IR1 straight section, scaled to the factor p/p_0 where p is the lost protons momentum and p_0=7 TeV. The horizontal blue line indicate the estimated quench limit assuming 7 TeV protons.

that the deposited energy in the triplets can reach the level of 10 Watts per meter.

7.5.2 PTC loss maps with single collimators

The loss maps produced with PTC for different settings of the TCL4 collimator, while maintaining all other collimators wide open, are shown in Fig. 7.10 for all the region on the right side of ATLAS. The plots indicate that TCL4 at $30\,\sigma_x$ (blue line) is sufficient to protect all magnets (Q4 included) in the region from 150 m to 180 m from the interaction point. For the same settings the losses on the Q5 magnet are reduced by a factor of 10. On the other hand, even an extreme closure of TCL4 (e.g. red line in the figure) only partially reduces the integrated losses from 250 m downstream.

The loss maps produced with PTC for different settings of the TCL5 collimator, while maintaining all other collimator wide open, are shown in Fig. 7.11. In this case, the plots indicate that TCL5 at $50\,\sigma_x$ (yellow line) is sufficient to protect all magnets (Q5 and Q6 included) in the region from 190 m to 250 m from the interaction point. For the same settings the integrated losses in the region from 250 m to 350 m are slightly reduced, whereas the peak losses remain, as without collimators (black line), one order of magnitude below the estimated quench limit. In this second region, even when the TCL5 collimator is closed to $10\,\sigma_x$ (red line), the peak losses remain unchanged even though the integrated losses are reduced by about a factor of 5.

It is very relevant to notice that neither TCL4 or TCL5 have any effect on the losses after 350 m from the IP, even when closed to $10\,\sigma_x$.

7.5.3 PTC loss maps with different collimator schemes

This section discusses two possible collimation schemes that, according to the simulations, guarantee the same LHC protection as with the existing scheme and allow enough forward proton acceptance at the AFP detectors proposed at 220 m. Both proposals envisage the presence of a collimator (TCL6) at about 230 m, in front of the Q6 quadrupole.

The first alternative implies the displacement of the TCL5 collimator from the slot just upstream of Q5 to the one upstream of Q6. The loss maps produced with PTC with both TCL4 and a new TCL6 at $30\,\sigma_x$ is shown in Fig. 7.12 (green line) and compared to the situation without collimators (black) and with a possible configuration of the present scheme (red, TCL4 at $30\,\sigma_x$ and TCL5 at $15\,\sigma_x$). This alternative configuration results in the reduction of a factor 10 (w.r.t. the case of no collimators) of the peak losses on Q5 and reduces by a factor of 3 (w.r.t. the existing solution) the integrated losses in the region from 250 m to 350 m. This solution would not require the production of a new collimator.

The second alternative implies the fabrication of a new collimator and its installation in front of Q6, while leaving in place the TCL5 collimator. The loss maps produced with PTC while setting TCL4 at $30\,\sigma_x$, TCL5 at $50\,\sigma_x$ and a new TCL6 at $40\,\sigma_x$ is shown in Fig. 7.13 (green line) and compared to the situation without collimators (black) and to the first alternative presented above (red). This second alternative would guarantee a full cleaning of the losses in the Q5 region, while reducing by a factor of about 2 (w.r.t. the existing solution, red line in Fig. 7.12), the integrated losses in the region from 250 m to 350 m.

As discussed later in the note, both alternatives would allow enough forward proton acceptance at the AFP detectors proposed at 220 m.

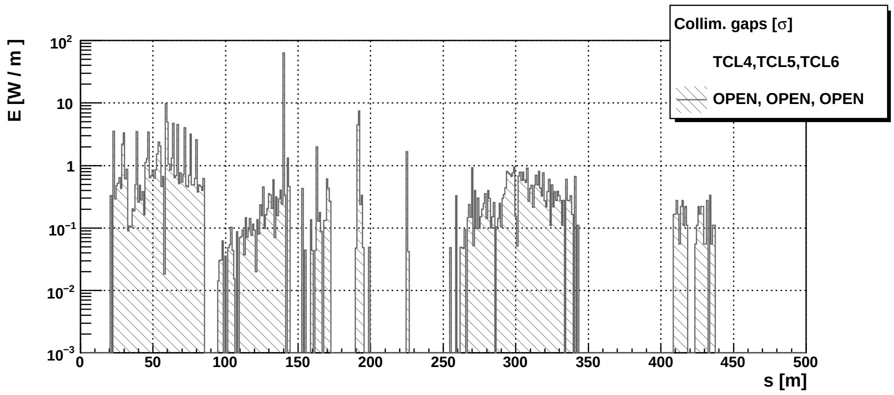

Figure 7.9: Energy deposition corresponding to the loss map shown in Fig. 7.6. Hence, it should be better if p/p_0 is considered (see Fig. 7.8).

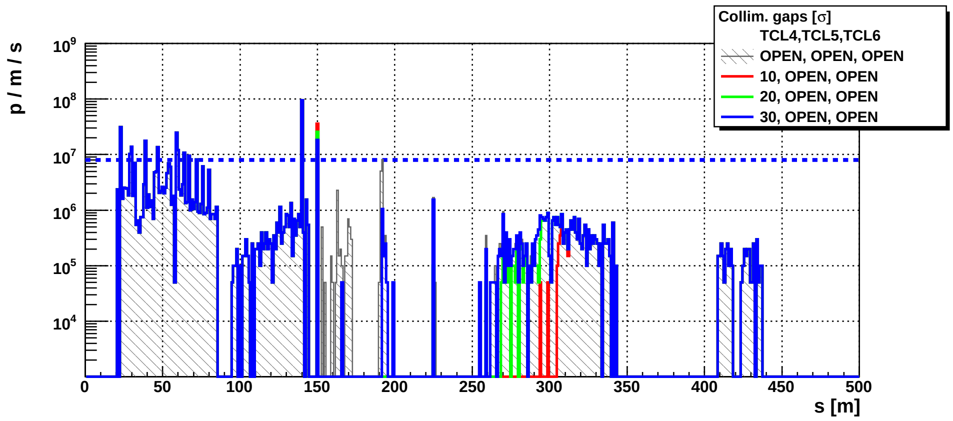

Figure 7.10: PTC loss maps with different settings of the TCL4 collimator installed at about 140 m from IP1. The horizontal blue line indicate the estimated quench limit assuming 7 TeV protons.

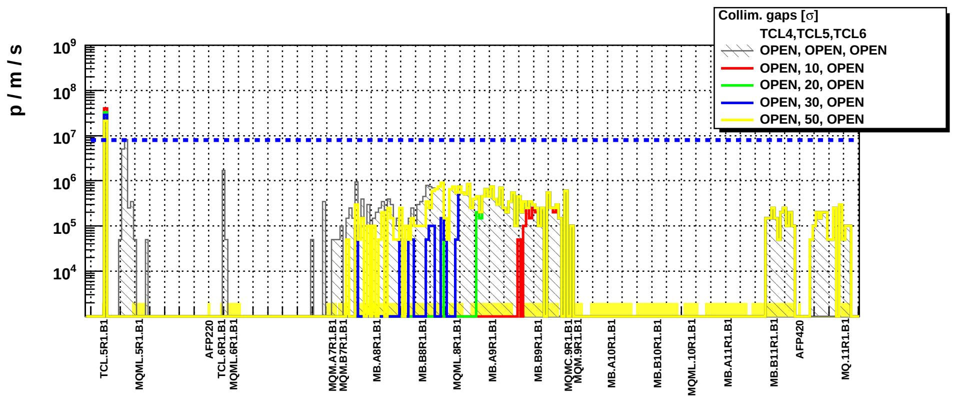

Figure 7.11: PTC loss maps with different settings of the TCL5 collimator installed at about 190 m from IP1. The horizontal blue line indicate the estimated quench limit assuming 7 TeV protons.

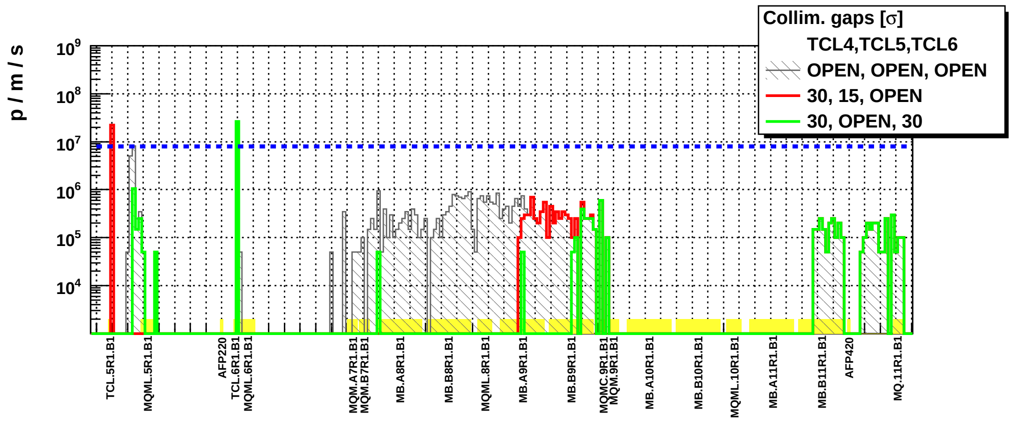

Figure 7.12: Comparison between loss maps with the presently foreseen collimation scheme (red) and a first alternative scheme (green) implying the displacement of TCL5 in front of Q6.

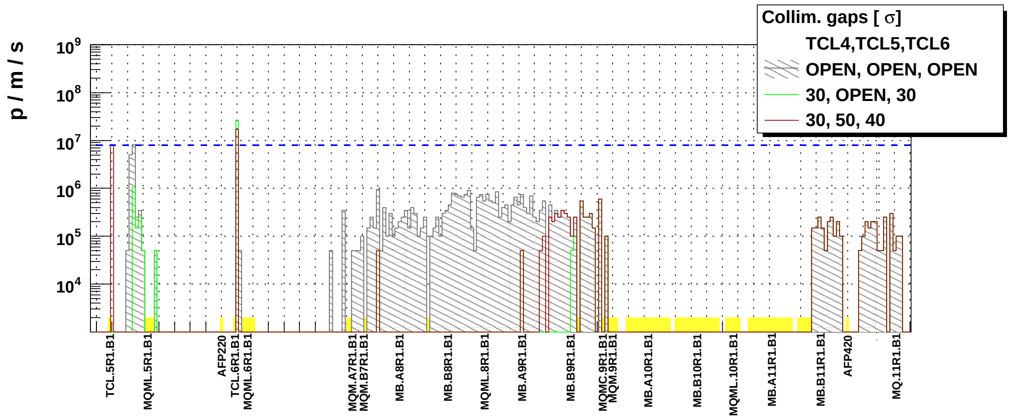

Figure 7.13: Comparison between loss maps with a second alternative scheme (green) implying the installation of a new collimator in front of Q6 and the first alternative presented in Fig. 7.12.

7.6 Conclusion

The analytical calculations and tracking simulations presented in this note provide two alternative collimation schemes to the one presently foreseen in the ATLAS (and CMS) straight section regions. According to these studies, the two alternatives would guarantee the LHC protection from physics debris and enough acceptance for the detectors proposed at 220 meters from the IP. Both alternatives imply the installation of a collimator between the Q5 and Q6 magnets, as close as possible to Q6. This looks possible after studying the present LHC layout and a visual inspection in the tunnel. However, a detailed study of the collimator integration is necessary for validating the proposal.

The overall study interpretation depends on the estimated quench limit for the superconducting elements and the early LHC runs will give information about the accuracy of such estimation.

Even though the studies considered a perfectly linear model of the LHC optics, the relative comparison among loss maps produced with different collimation schemes is considered accurate. Indeed, the numerical simulations reproduced nicely the results of Baichev-Jeanneret performed with a different tracking code and p-p generator. In addition, the two independent codes PTC and SIXTRACK exhibited very consistent results when using the same LHC model in terms of optics and aperture.

The absolute simulation accuracy can be improved by considering magnetic field errors measured in the laboratory and magnet elements misalignment measured in the LHC tunnel. The results could also be improved by using the accelerator optics as measured during the early LHC runs.

A complete estimation of the effect of the physics debris on the LHC elements can be achieved by modeling the electromagnetic and hadronic showers resulting from the scattering of the of the proton on the TCL. This can be done with Monte Carlo codes such as Geant4 and FLUKA, with the showers initiated from the PTC loss maps in the collimators.

Chapter 8

Appendix II: LHC Optics, Acceptance, and Resolution

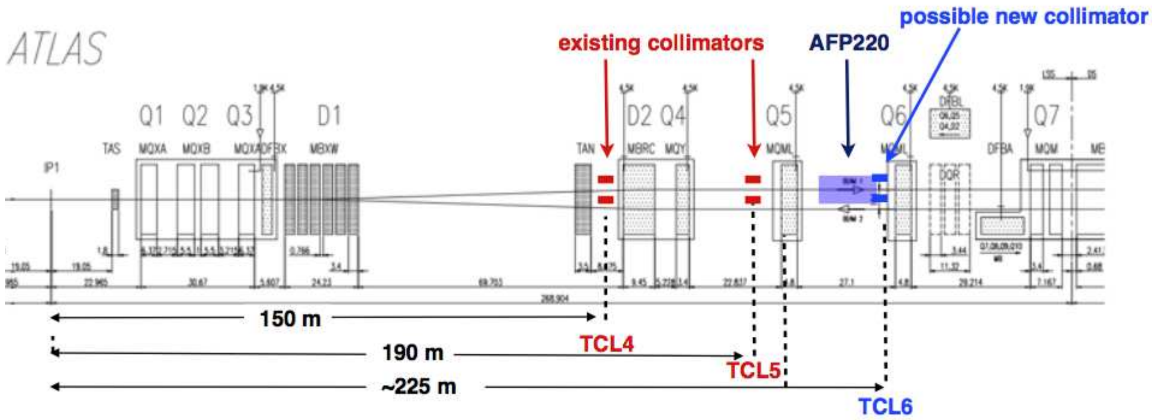

Figure 8.1: chematic view of the beamline at IP1.

8.1 Beamline

The configuration of the LHC beamline around the interaction points is shown schematically in Figure 8.1. The proposed forward detector stations are to be installed in the regions located at approximately 220 m from the IP1 interaction point in both beamlines downstream of the central detector. A similar installation is planned for the IP5 region. Protons that have lost energy in the primary interaction are not focussed to travel long distances around the beamline and emerge laterally after passing through bending magnets. At 220m we can observe protons that have lost typically 100 GeV or more in the primary interaction. The acceptance and the ultimately achievable energy resolution of the forward detectors depends on the LHC beam optics and on the position of the detectors relative to the beam.

The AFP Collaboration has written a tracking program, FPTrack [58], which has been incorporated into the ATHENA package. It tracks protons (or other particles) that emerge in a forward direction from the interaction region, and tracks them through the system of magnets and collimators that form the beamline, in either direction. FPTrack is much easier and faster to use in this context than the MAX-D program, the standard beam transport program used at

CERN, and detailed comparisonss have been carried out to ensure that the two programs give results that are in agreement. A model of the LHC beamline optics is implemented, and it can be updated when new beam optics configurations are announced. The CMS collaboration also have their own tracking program and, again, checks have been made that the programs are all equivalent. All calculations presented here are in terms of the planned 7000 GeV beamline.

The tracking operates by applying thick-magnet bending using a full momentum-dependent formula at each bemline element. This is essential owing to the non-linearities in the system when off-axis and off-momentum particles are being tracked. Collimators are taken into account, as are the apertures of the beamline elements. Two collimator conditions are considered, "open", in which the collimators TCL.4, TCL.5 and TCL.6 are opened, and "closed", in which they are set at positions that have been calculated to protect the beam elements with minimal obstruction to the beam. In this context the configuration "30,50,40" described in Appendix I has been used.

It should be noted that in the optics files used in the present work there are no sextupole magnets, and so the horizontal and vertical bending and focussing of the protons are independent of each other. All the critical properties of the beamline of relevance here depend only on the horizontal behaviour of the beam apart from aperture effects, which are fully taken into account in both dimensions.

Unless otherwise stated, we use the ExHuME or FPMC Monte Carlo [59] to generate outgoing protons from the central exclusive production of a SM Higgs Boson, although the results will apply for any double-diffractively produced system. Version 6.503 of the LHC optics files have been used with: $\beta^* = 0.55$ m; angular divergence at the IP $\sigma_\theta = 30.2$ μrad; crossing angle = 142.5 μrad in the vertical (horizontal) plane at IP1 (IP5); beam energy spread $\sigma_E = 0.77$ GeV. The energy spread of the 7000 GeV beam is taken into account and is an irreducible limiting factor on the mass resolution obtainable by proton tagging detectors at the LHC

8.2 Detector Acceptance

The position and direction of a proton as it hits the 220 m detectors (for a given LHC optics) depend on the energy E and scattering angle θ of the proton as it emerges from the primary interaction, and on the z-vertex position where this occurs, although the latter has a relatively weak effect. The variables E and θ are directly related to ξ, the fractional longitudinal momentum loss of the outgoing proton, and $-t$, the square of the four-momentum transfer. Figure 8.2 shows the acceptance in the ξ-t plane for the 220 m regions for beam 1 and beam 2 respectively, around IP1. The acceptance is averaged over the azimuthal angle of the emerging proton, and hence can take intermediate values in the range (0., 1.).

The acceptance is affected by the collimator settings used. To illustrate this, the figures shows acceptances with the collimators referred to above open and closed. Unless mentioned, all quantities in the present section refer to calculations made with the closed-collimator configuration. There are regions of parameter space where the acceptance, averaged over the azimuthal angle of the proton, is excellent, and these are not greatly impacted by the necessary use of the collimators.

Figure 8.3 shows the proton distributions in the horizontal coordinate x at 220 m from the interaction point. The distribution is averaged over the proton momentum distribution and depends on the type of physics process that is generating the protons. There are differences between the two beamlines which it is necessary to keep under scrutiny. The upper distributions are obtained as an average over a range of masses of a centrally double-diffractively produced object, between 180 and 1440 GeV. The lower distributions are obtained from a model of the main diffractive processes that are expected to occur in proton-proton interactions at 7000+7000

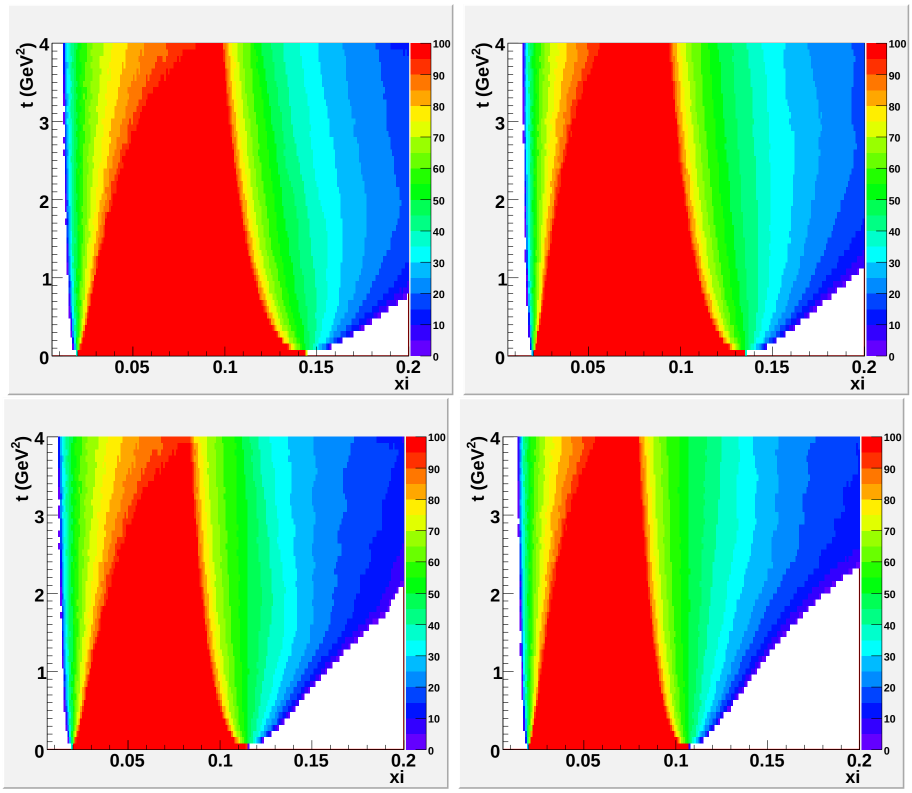

Figure 8.2: Acceptance in the ξ, t plane for protons to reach planes at 220 m in beam 1 (left) and beam 2 (right) around IP1, where ξ is the fractional energy loss of the proton. The variable plotted as t is the modulus of the squared momentum transfer to the proton at the IP and ξ its fractional energy loss; no detector effects are included here. Upper (lower) plots: collimators open (closed).

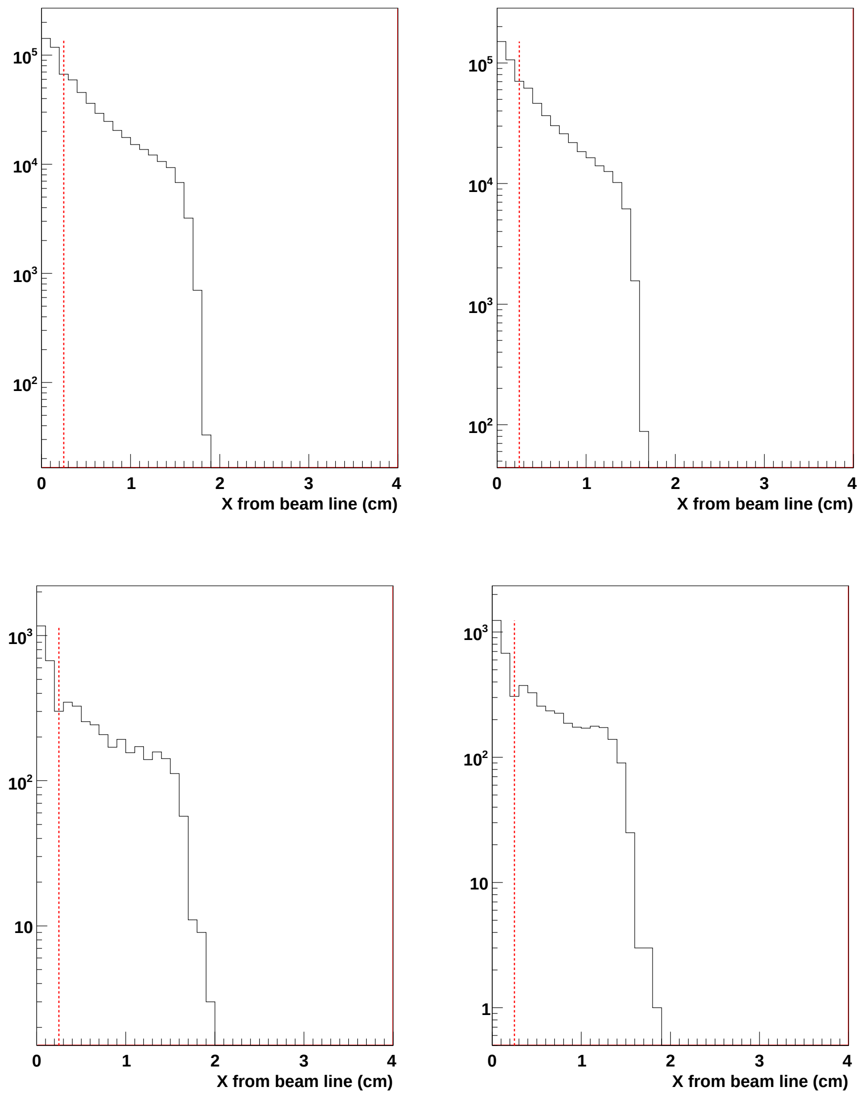

Figure 8.3: Distributions in x for protons at the plane at 220 m in beam 1 (left) and beam 2 (right) around IP1. The distributions are for single protons arising from the central exclusive double-diffractive production of an object with mass averaged over the mass range 180 to 1440 GeV (upper). The lower plots are for protons produced in association with diffractive production.

GeV. These are of physics interest in their own right, but will form a background to any processes of a rarer nature.

In order to understand the issues that determine the design of the silicon detector systems, a further set of plots (fig 8.4) shows the x distributions obtained from protons originating from cenmtrally produced objects generated over a selection of masses. The general feature is that at lower masses the protons emerge closer to the beamline, with broader distributions developing as the mass increases. In the plots shown in this figure, a pair of protons in coincidence is not demanded, and just the single protons are plotted, since the probability of a a coincidence is small at masses below about 400 GeV. In fig. 8.5, proton distributions are shown at higher masses with the requirement that a proton is detected in both silicon detector systems. Fig. 8.6 shows the proton hit distributions for different region in diffractive mass.

Fig. 8.7 shows the acceptance of the system for detecting a proton in the 220m systems in both beamlines in coincidence, as a function of the mass of a double-diffractively produced central object X. It varies substantially with the distance of the silicon detectors from the beam, which for convenience is taken here to be the same in both beamlines, although in practice this is not a necessary constraint. As the distance increases, the lower end of the range of accepted masses increases, but the upper end is not affected. The acceptances shown are calculated with our best available model of the collimator settings that could be used. To illustrate the effect of the collimators, the acceptances have been calculated for one position setting with the collimators wide open, (which is not seen as a possible operating condition). The collimator settings affect the acceptance over the upper mass range, and it can be seen that an optimally calculated setting of the collimators, consistent with machine safety, will be required.

The position of the silicon detectors that we can use will be determined in close collaboration with the accelerator experts, and will need to allow for an inevitable “dead region” occupied by the wall of the movable beam pipe and the edge of the silicon detectors. The permitted distance between the beam and the closest physical material is normally assumed to be 10 times the Gaussian width “sigma” of the beam, where sigma at 220m is 0.09 mm horizontally according to the currently assumed optics. We show results for the separation between the beam and the active silicon detection region having an “optimistic” value of 2 mm, a “realistic” value of 2.5 mm and a “pessimistic” value of 3 mm.

8.3 Momentum determination

The mapping of the energy loss and outgoing angle of a proton at the interaction point on to a position and angular measurement in the detector at 220 m or 420 m can be visualized using chromaticity plots. Figure 8.8 shows iso-energy and iso-angle curves for protons with energy loss ranging from 0 to 1000 GeV in steps of 100 GeV at 220 m, evaluated at points in the range $\pm 250\mu$rad in steps of 10 μrad. If the protons were bent out of the beamline in a simple manner, the isoenergetic sets of points would be vertical, corresponding to a fixed value of x for a given proton momentum. However the non-linear nature of the beam optics, involving energy dependence of the transfer matrices, produces chromaticity plots that are very different from such a situation.

The chromaticity plots show that the measurement of the energy of the outgoing proton requires good measurements of both position and angle in the detector stations. Thus, at low momentum losses ξ an excellent position measurement is required, whereas the measurement of higher momentum losses becomes increasingly determined by the angular measurement. Hence we shall require detector stations distributed suitably along the space available to us at 220m.

Polynomial-based parametrization formulae have been developed in order to evaluate the

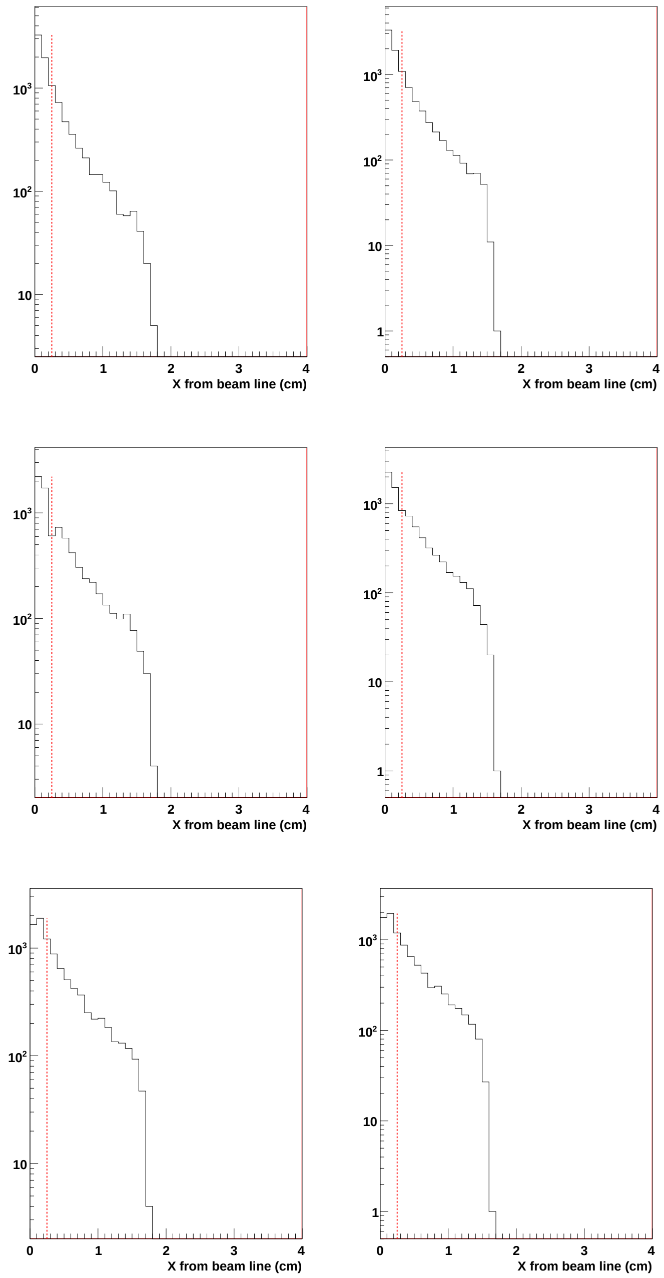

Figure 8.4: Distributions in x for protons at the plane at 220 m in beam 1 (left) and beam 2 (right) around IP1. The distributions are for single protons arising from the central exclusive production of an object with mass 180 GeV (upper), 240 GeV (centre), 360 GeV (lower).

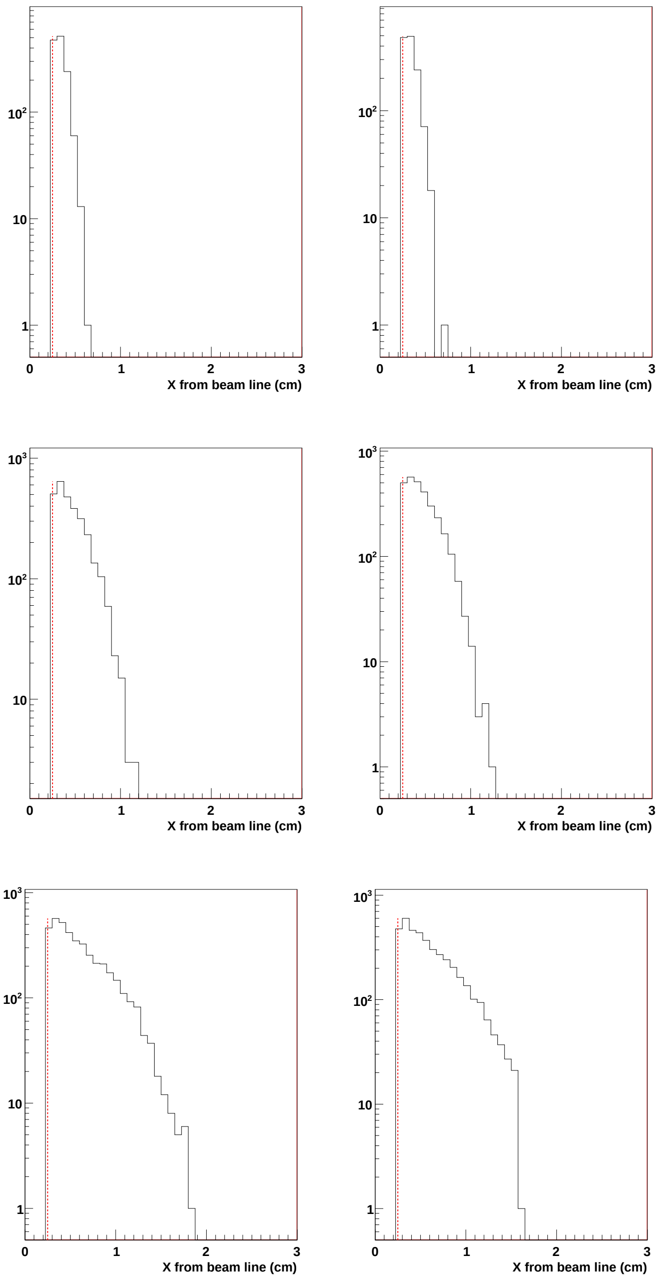

Figure 8.5: Distributions in x for protons at the plane at 220 m in beam 1 (left) and beam 2 (right) around IP1. The distributions are for protons from the central exclusive production of an object with mass 360 GeV (upper), 480 GeV (centre), 600 GeV (lower). Both protons are require to emerge at a distance of at least 2mm from the beam.

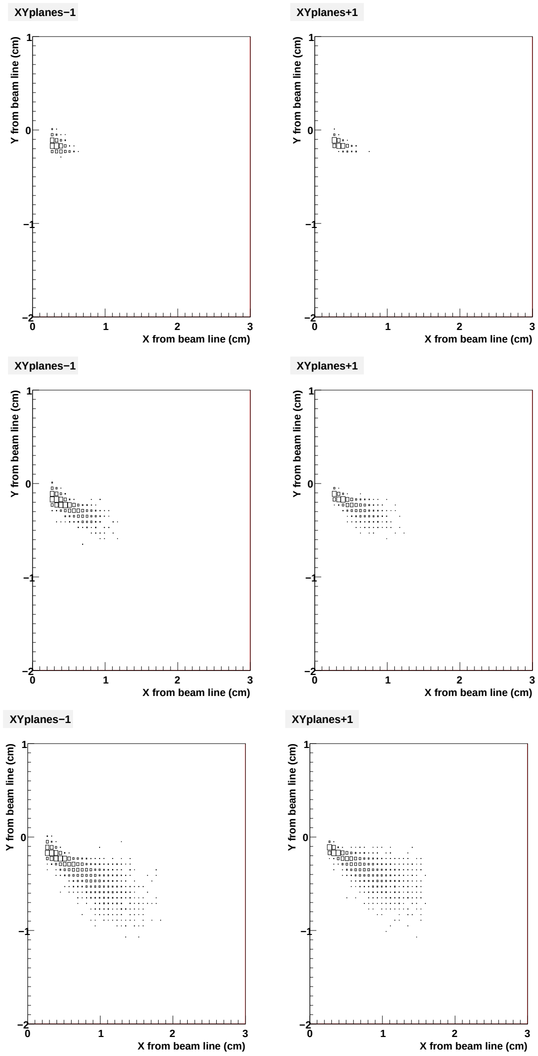

Figure 8.6: Distributions in x, y for protons at the plane at 220 m in beam 1 (left) and beam 2 (right) around IP1. The plots are for objects with mass 360, 480 and 600 GeV (second, third and fourth lines) when both protons are detected.

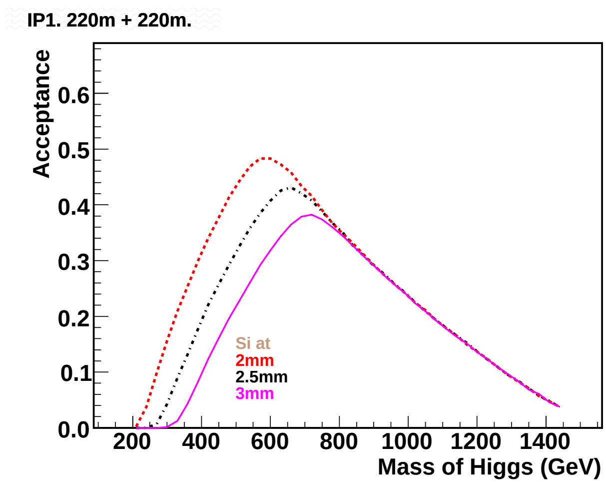

Figure 8.7: Acceptance as a function of centrally produced mass for 220 + 220 m proton tags for the edge of the silicon detector active region located at different distances from the beam. The collimators are closed.

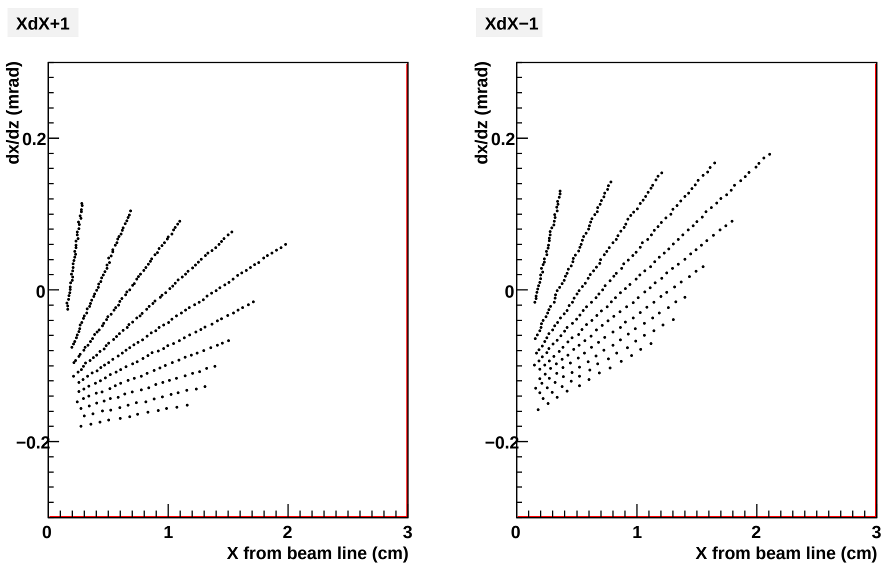

Figure 8.8: Chromaticity distributions for the 220m detectors in beam 1 (left) and beam 2(right). The radially distributed sets of points are for protons at energies of 6900 GeV, 6800 GeV, etc, starting at the left of each plot and reading clockwise. Within each set, the points denote protons emerging from the primary interaction at intervals of 10 μrad in the horizontal plane.

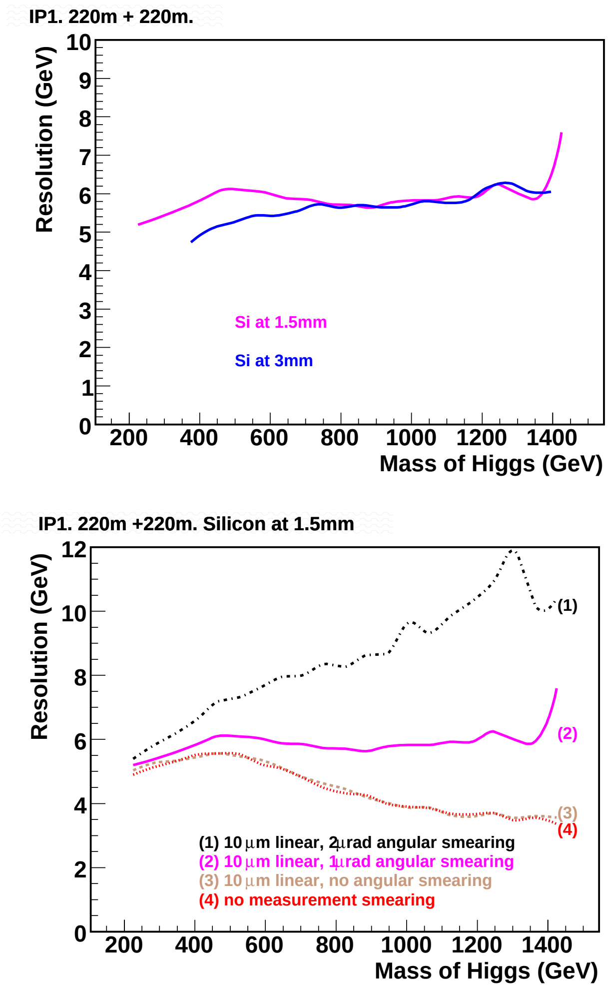

Figure 8.9: Reconstructed mass resolution for production of central objects of various masses. First plot: applying nominal measurement resolution and experimental smearings, the resolution for two different values of the silicon distance from the beam is compared. Second plot: effect of various values of measurement resolution on the mass resolution. The fluctuations on the curves are of a statistical origin.

proton momenta from the measured parameters in the silicon detectors. The formulae are based on fits to the calculated positions and angles, using the generated values of the momentum and emission angle at the IP, and averaging over the width of the beam-beam interaction region. Further development in this area is in hand, using the ALFA code to unfold the initial parameters of the forward proton given the final measured parameters.[60]

8.4 Mass measurement

From the momenta of the pair of oppositely emerging protons in an event, the mass of the centrally produced system can be calculated by a missing-mass formula [61]. The mass resolution was evaluated by a Gaussian fit to the difference of the calculated and input masses. Minimizing this resolution is important for the physics capabilities of the proposed new detectors. For present purposes, we consider protons whose event vertex is at the nominal position of the interaction point. Effects of variations of the x and z are easily included, and we find that they are not large. It is to be noted that the vertex position is well-measured by the central detector for every event, and the average value of x and z for a given run will also be well-measured; both quantities are expected to is expected to be quite stable within a run. Thus offline corrections for the mean variations and event-by-event are easily applied.

The following factors affect the measured mass resolution of a narrow object produced in the exclusive double diffraction process:

- The Gaussian width of the momentum distribution of the circulating proton beam. This is specified as 0.77 GeV.
- The lateral uncertainty of the position of the interaction point. This is taken to be 11.8 μm from the intrinsic beam width, but can be improved if the central silicon detector system provides a better measurement on an event-by-event basis.
- The angular spread of the interacting beams, corresponding to a lateral momentum smearing of 0.21 GeV on the outgoing proton.
- The position measurement uncertainty in the detector system
- The angular measurement uncertainty in the detector system.

Figure 8.9 shows the affect of the above factors on the mass resolution. We first confirm that the resolution is not greatly dependent on the distance of the silicon detectors from the beam, provided that the acceptance is present, by fixing the smearing conditions at some standard values (Item (2) below).We then examine the effects of fixing the silicon distance at a minimum value of 1.5 mm, and varying the smearing that is applied (right plot):

- (1) Applying 10 μm linear and 2 μrad angular smearing on the x measurement of the proton at 220m.
- (2) As (1), but with the angular smearing reduced to 1 μrad.
- (3) As (1) but with no angular smearing
- (4) With no measurement smearings, but including all the intrinsic smearings.

It can be seen that an accurate angular measurement is critical, but to achieve a reasonable value of $\pm 1\mu$rad in this quantity, we must measure the positions to high precision. As the momentum loss ξ of the protons emerging from the primary interaction increases, the missing mass increases but the momentum measurement becomes increasingly dependent on the angular measurement, as noted in discussing the chromaticity plots.

It is possible to measure the transverse momentum of the proton as it emerges from the interaction point, again by means of polynomial-based parametrization formulae using the measurements in the detector stations. Both x and y measurements are required to determine the full transverse momentum of the proton. The measurement is degraded by two factors. The angular beam spread at the interaction points is equivalent to a $\pm$ 0.21 GeV transverse momentum spread, both horizontally and vertically, and the poorer measurement uncertainty in the y direction increases the overall uncertainty on p_T significantly. Studies are continuing to determine the requirements for particular physics studies and whether they can be achieved.

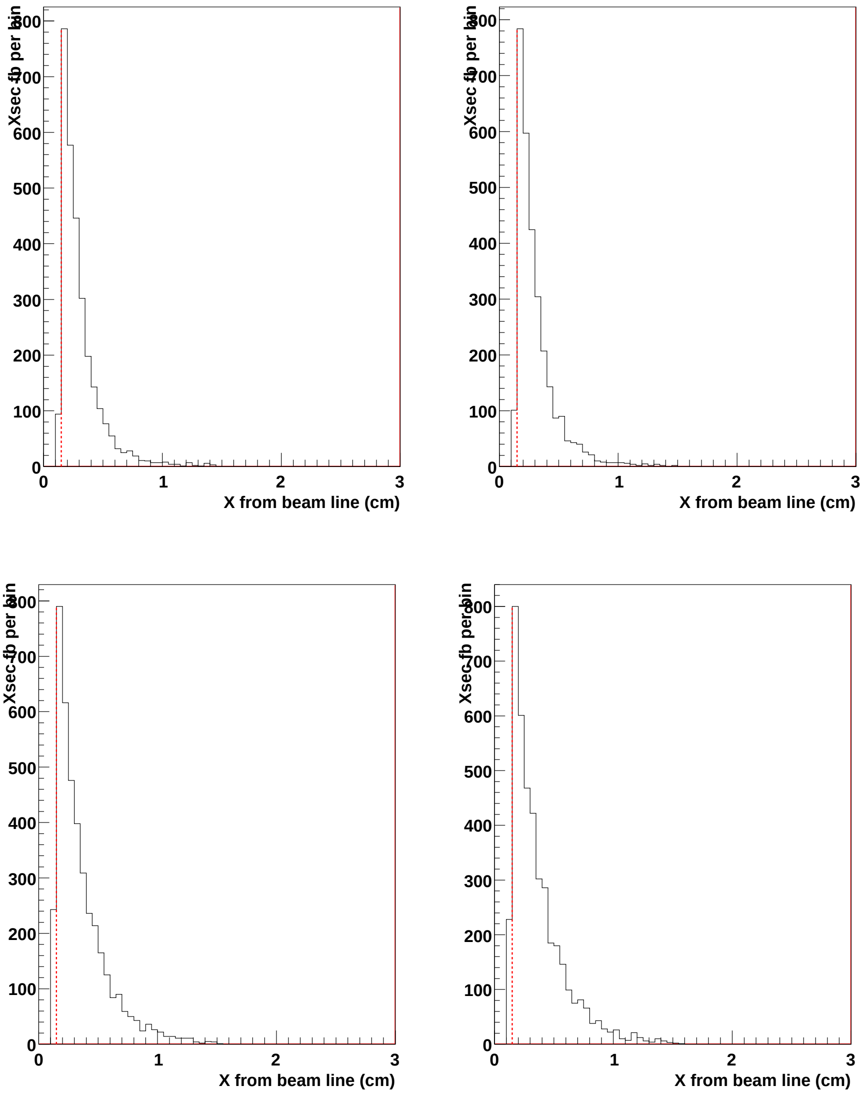

Figure 8.10: Cross section for detecting a forward proton accompanying a muon pair produced by the photon-photon process in the central detector within a rapidity range of ± 2.5. Left, beam 1; right; beam 2; upper, muon $p_T > 4$ GeV; lower, muon $p_T > 6$ GeV. The plotted cross sections are fb per bin in x measured in the silicon planes.

8.5 Calibration

Consistent alignment of the silicon system relative to the magnets, the beamline and the experimental hall can be achieved by means of beam position monitors, as discussed in the relevant section of this proposal. However to take account of any unknown or unforseen effects, it is necessary to calibrate the momentum measurement of the protons. This can be done by means of the production of lepton pairs, of which muon pairs give best precision, in the central ATLAS detector. Triggers exist that should be able to record events in which a muon pair is produced by the photon-photon process where the photons radiate off the protons. At present, we foresee a trigger on muon pairs where each muon has transverse momentum of at least 6 GeV, however a lower value could be helpful.

The accurately measured momenta of the muons allow the momenta of the forward protons to be accurately evaluated. If either of the latter is measured in the respective forward system, its measured momentum can be compared with the value obtained from the muon pairs, and with sufficient statistics a calibration can be achieved. It is not necessary to record both of the forward protons that emerge in any given event.

Using the LPAIR program to generate muon pairs produced within an overall rapidity range of ± 2.5,we have estimated the rates of calibration events that can be obtained in this way. They are shown in fig. 8.10 and their values should allow a suitable calibration to be made over a period of time: to calibrate a shift of the mean momentum of one-tenth of its measured resoution, 100 events would be required, which would require of the order of $1/20$ fb^{-1} of integrated luminosity. The situation is assisted if the detectors can be moved as close as possible to the beam, which is desirable anyway.

Another possible calibration method that we are considering is to use the bremstrahlung photons recorded in the ZDC. The energy of such a photon has been lost by the forward proton, whose energy is thereby calibrated. There are serious backgrounds in this method, however, and it is harder to implement than the muon-pair method, although the cross section is very much higher.

8.6 Summary

The beam optics at LHC allows protons that have lost momentum in a diffractive interaction to emerge from the beam envelope at regions 220 m from the interaction point. By placing silicon detector arrays in these locations we can detect the protons and obtain good acceptance for diffractively produced objects with a wide range of masses above 180 GeV, the precise acceptances depending on how close it is possible to place the detectors relative to the beam. The expected position and angle resolutions for the protons obtained in the silicon stations are expected to yield mass resolutions of around 6 GeV from the proton pair alone.

Chapter 9

Appendix III: A possible extension of the AFP project using 420 m detectors

In order to detect centrally produced objects in the mass range $\sim$ 120 GeV it will be necessary to install proton tagging detectors in the cold region of the LHC 420m from the ATLAS IP. The FP420 Collaboration commissioned the CERN design office, working with the TS/MME group to design a cost effective and safe replacement for the 420m connection cryostat. The main design parameters were to provide warm beam pipes and sufficient space to install moveable silicon tracking and fast timing detectors with little or no disruption to the LHC itself. In this chapter, we describe the new connection cryostat design, as weel as the physics motivations of such an extension of our proposal.

9.1 Physics program in 220+420 stage

With the 420 m extension of the forward proton detecting system, much broader spectrum of physics applications will be reached. A detailed complete description is given in [24]. Here we summarize those topics that were not possible with the 220 m detectors only. As a rule of thumb, the acceptance in ξ for detectors at 220+420 m corresponds to $0.0015 < \xi < 0.1$ and is dominated by very low t.

9.2 Central Exclusive Production

There are three important reasons why CEP is especially attractive for studies of new particles. Firstly, if the outgoing protons remain intact and scatter through small angles then, to a very good approximation, the primary active di-gluon system obeys a $J_z = 0$, C-even, P-even, selection rule [7]. Here J_z is the projection of the total angular momentum along the proton beam axis. This selection rule readily permits a clean determination of the quantum numbers of any new resonance. Secondly, because the process is exclusive, the energy loss of the outgoing protons is directly related to the invariant mass of the central system, allowing an excellent mass measurement irrespective of the decay mode of the central system [61]. Even final states containing jets and/or one or more neutrinos are measured with $\sigma_M \sim 2$ GeV/c^2. Thirdly, in many topical cases and in particular for Higgs boson production, a signal-to-background ratio of order 1 or better is achievable. This ratio becomes significantly larger for Higgs bosons in certain regions of MSSM parameter space [62]. The CEP cross sections in the following discussion are calculated using the KMR model [7].

9.2.1 $h \to b\bar{b}$

As an example of what may be possible with ATLAS FP, we briefly review a detailed analysis carried out in [62] of the $h \to b\bar{b}$ channel in a specific MSSM scenario. The MSSM point chosen for this analysis is m_A = 120 GeV and tanβ=40. The lightest Higgs boson, h, has a mass of 119.5 GeV and the cross section×branching ratio is approximately 20 fb. ATLAS FP is particularly well suited to observing the Higgs sector in certain regions of MSSM parameter space; at high tanβ the CEP cross sections are in general enhanced with respect to the Standard Model and the branching ratio to $b\bar{b}$ can be as high as 90% if the light SUSY decay channels are not allowed. Furthermore, the $J_z = 0$ selection rule suppresses the irreducible $b\bar{b}$ continuum background significantly, thus enhancing the signal to background ratio with respect to standard search channels. Finally, because the pseudo-scalar A cannot be produced in CEP, ATLAS FP will provide a clean measurement of the mass and quantum numbers of h and H even when m_A is close to m_h or m_H, which can occur at high tanβ. CEP can therefore provide complementary information about the Higgs bosons if the MSSM is realised in nature and could allow a measurement of the $Hb\bar{b}$ coupling, which may be difficult in other production channels.

The challenge is controlling the overlap (or pile-up) background at high luminosity. The primary overlap background consists of a three-fold coincidence in one bunch crossing between an event producing a hard scatter, with the signature of interest detected in ATLAS, and two single diffractive events that produce forward protons within the acceptance of the forward detectors. The overlap background is most problematic for dijet final states because there is a large cross section for non-diffractive dijet production at the LHC. For example, the overlap background to $h \to b\bar{b}$ is estimated to be a factor of 10^5 (10^7) larger than the signal for a luminosity of 10^{33} (10^{34}) cm^{-2} s^{-1}.

There are several techniques that can be employed to reject the overlap background: (i) vertex matching using the di-jet vertex and fast-timing detectors, (ii) topological requirements, (iii) kinematic matching between the di-jet system and central system measured by the forward detectors and (iv) charged track veto which discriminates against the much larger track multiplicity in non-diffractive events due to multiple parton-parton interactions. The result is that the overlap background in the $h \to b\bar{b}$ channel is negligible up to $\sim 2{\times}10^{33}$ cm^{-2}s^{-1} and smaller than the other backgrounds up to $\sim$ $5{\times}10^{33}$ cm^{-2} s^{-1}. At instantaneous luminosities up to 10^{34} cm^{-2} s^{-1} it becomes desirable to upgrade the fast timing system to a resolution of 5 to 10 ps.

Figure 9.1 (a) shows the expected mass distribution for protons tagged at 420 m for this parameter choice given 60 fb^{-1} of data collected at $2{\times}10^{33}$ cm^{-2} s^{-1}. The significance is 3.5σ. Figure 9.1 (b) shows the same distribution but for 300 fb^{-1} of data collected equally at $7.5{\times}10^{33}$ cm^{-2} s^{-1} and 10^{34} cm^{-2} s^{-1} and assuming improved timing rejection. The significance increases to 4.5σ.

A detailed study of the coverage in the M_A-tanβ plane afforded by forward proton detectors at 420m and 220m from the interaction point was carried out in [62] for several benchmark MSSM scenarios. Figure 9.2 shows the 3σ contours for $h \to b\bar{b}$ observation (upper plot) and $H \to b\bar{b}$ observation (lower plot). Curves are shown for 60 fb^{-1} and 600 fb^{-1}. The 60 fb^{-1} scenario was presented as 3 years of data taking at ATLAS and CMS at 10^{33} cm^{-2} s^{-1}, which was a scenario with negligible overlap background. The 600 fb^{-1} scenario corresponds to 3 years of data taking by both ATLAS and CMS at 10^{34} cm^{-2} s^{-1}. Figure 9.2 shows that a large region of the M_A-tanβ can be covered at the 3σ level given enough luminosity. For example, if tanβ = 40

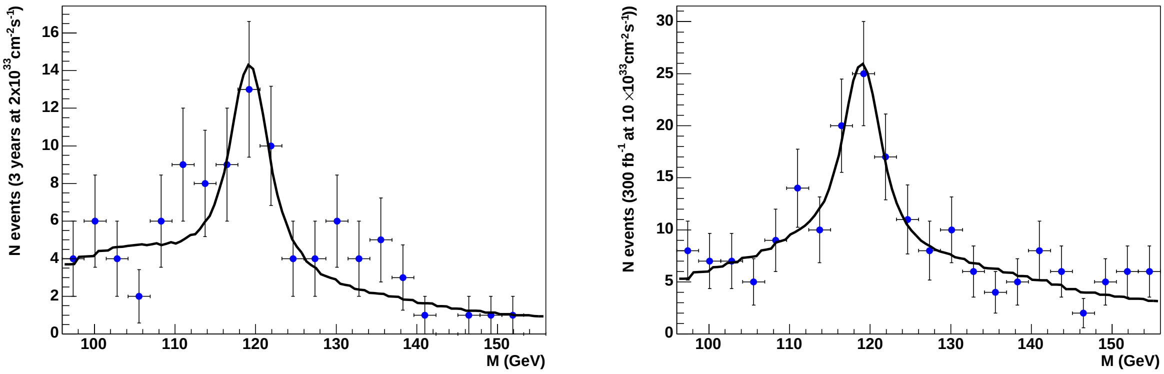

(a) (b)

Figure 9.1: Typical mass fits for the 120 GeV/c^2 MSSM $h \to b\bar{b}$ for (a) 3 years of data taking at 2×10^{33} cm^{-2} s^{-1} (60 fb^{-1}, 3.5σ, 10 ps timing) and (b) 1.5 years of data taking at 7.5×10^{33} cm^{-2} s^{-1} and 1.5 years of data taking at 10^{34} cm^{-2} s^{-1} (300 fb^{-1}, 4.5σ, 5 ps timing).

and $M_A = 120$ GeV/c^2, then $h \to b\bar{b}$ would be observed with 3.8σ significance with 60 fb^{-1} of data (upper plot). For tan$\beta > 30$, the significance is 5σ or above. Such a measurement would provide a unique determination of the quantum numbers of the Higgs boson.

It is also possible to test for CP-violation in the MSSM Higgs sector. The azimuthal asymmetry in the outgoing tagged protons is expected to be quite sizable in some MSSM scenarios [63, 64]. In addition, the cross sections can become so large in the MSSM that the excellent mass resolution of the forward detectors could allow to distinguish between Higgs bosons that are almost degenerate in mass, as shown for the tri-mixing scenario in [63].

9.2.2 $h \to \tau\tau$

In the MSSM, the branching ratio of the Higgs bosons to $\tau\tau$ is approximately 10% for $M_{H/A} >$ 150 GeV/c^2 if the decays to light SUSY particles are not allowed. The τ's decay primarily to 1-prong (85%) or 3-prong (15%) track topologies; therefore requiring no additional tracks on the $\tau\tau$ vertex is very effective at reducing non-exclusive background.

The possibility of observing the Higgs boson through its decay to $\tau\tau$ was investigated in [62], It was shown that the heavy neutral Higgs, H, can be observed at 3σ in this channel across a large area of the $M_A -$ tanβ plane; for m_A ∼120 GeV, the 3σ contour extends as low as tan$\beta \sim 10$ and at higher masses, $m_A \sim 200$ GeV, the $\tau\tau$ channel is observable for tan$\beta > 40$. The light Higgs boson, h, can be observed at 3σ confidence for m_A <130 GeV and tan$\beta > 15$.

9.2.3 $h \to 4\tau$

The possibility of a Higgs boson decaying to 4τ arises in the NMSSM, which extends the MSSM by the inclusion of a singlet superfield, $\hat{S}$ [63]. The Higgs sector of the NMSSM contains three CP-even and two CP-odd neutral Higgs bosons, and a charged Higgs boson. According to [65] the part of parameter space that has no fine-tuning problems results in the lightest scalar Higgs boson decaying predominantly via $h \to aa$, where a is the lightest pseudo-scalar. The scalar Higgs boson has a mass of ∼100 GeV/c^2. If the a has a mass of $2m_\tau \lesssim m_a \lesssim 2m_b$, which is

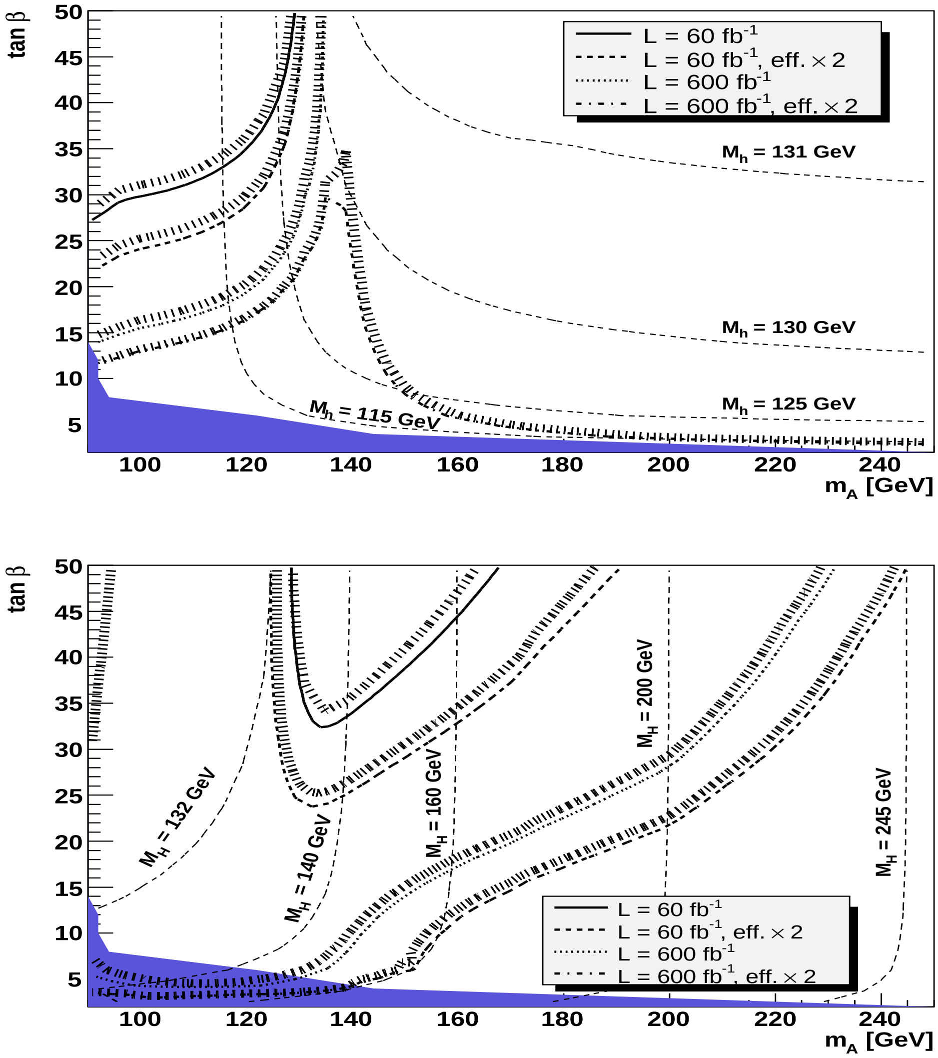

Figure 9.2: 3σ contours for $h \to b\bar{b}$ (upper plot) and $H \to b\bar{b}$ (lower plot) in the M_A - $\tan\beta$ plane of the MSSM within the M_h^{max} benchmark scenario (with $\mu = +200$GeV) for different luminosity scenarios as described in the text. The values of the mass of the Higgs bosons, m_h and M_H, are indicated by contour lines. Overlap background considered to be negligible. The dark shaded (blue) region corresponds to the parameter region that is excluded by the LEP Higgs boson searches.

preferred on general theoretical grounds, then the decay channel $h \to aa \to 4\tau$ would become the dominant decay chain. This is not excluded by LEP data and in such a scenario the LHC could fail to discover any of the Higgs bosons [65].

It was shown in [66] that the lightest Higgs boson could be discovered in CEP using forward proton detectors at ATLAS. It is expected that approximately 3-4 events will be retained (after all cuts) using a muon trigger of $p_T > 10$ GeV given three years of data taking if the instantaneous luminosity is greater than 10^{33} cm^{-2} s^{-1}. The event rates double if a combination of lepton triggers are used [24]. There is no appreciable background. The mass of the h is obtained using the missing mass method to an accuracy of $2-3$ GeV/c^2 (per event). Furthermore, using the kinematic information provided by the forward detectors and the tracking information from the central detector, it is also possible to make measurements of the a mass; in the above scenario the mass measurement is 9.3 ± 2.3 GeV/c^2.

9.2.4 Photon-Photon physics

The increase in forward detectors acceptance will ensure high rates of dilepton events used for calibration of 420 m detectors and for the luminosity measurement as already discussed Section 2.3.1. The rates for SM WW two-photon production are greatly enhanced and the production can be measured right from the kinematic mass threshold.

Easiest to observe experimentally are the fully leptonic decay channels; requiring no additional tracks on the $l^+ l^-$ vertex, large lepton acoplanarity and large missing transverse momentum strongly reduces the backgrounds, such as $\gamma\gamma \to \tau^+\tau^-$. The cross section for events where both W bosons decay into a muon or electron with $p_{\mathrm{T}} > 25$ GeV and a neutrino $E_{\mathrm{T}}^{\mathrm{miss}} > 20$ GeV is $\sim$ 2fb if both protons are tagged in a forward detector at either 220m or 420m [4]. For 30 fb^{-1} collected at low luminosity, one would expect approximately 60 events. The double proton tag requirement is necessary at high luminosity in order to efficiently suppress the overlap background from inclusive (partonic) WW production. Thus for 100 fb^{-1}, one would expect 200 events with two proton tags. It was shown in [4] that the SM two-photon could be observed at 5σ CL with thus 5fb^{-1}of data.

It is possible to investigate the higher rate semi-leptonic decay channel, although further studies are required to determine the effect of the overlap background. It was shown in [9] that the production cross section has a sharp turn on at $\sim 2m_W$, which allows an *in situ* calibration of the absolute forward detector energy scale to much better than 1% given 100 fb^{-1} of data. This process is also an interesting probe of the $WW\gamma$ vertex. The coupling enters the cross section calculation to the fourth power and so should be extracted with less than 1% uncertainty given 100 fb^{-1} of data. This constraint is competitive with the standard measurement from non-diffractive $W\gamma$ production and is insensitive to many of the systematics involved in that case.

The opportunity to investigate anomalous gauge boson couplings in vector boson pair production is to some extent possible with 220 mdetectors only. With combined detector acceptance, distributions of the background processes (arising from for example QCD double pomeron exchange WW production) can be well measured and the contamination in the signal sample can be well determined by cut inversion methods. In this way the background will be determined from data and derived limits on anomalous gauge couplings coupling will be more robust.

9.2.5 Supersymmetric particle production

Exclusive two-photon production of new charged particles provides a simple mechanism for the production of new physics beyond the Standard Model. Two photon production of SUSY leptons has been investigated in [67] and the cross section for $\gamma\gamma \to \tilde{l}^+\tilde{l}^-$ can be as large as 1 fb, while

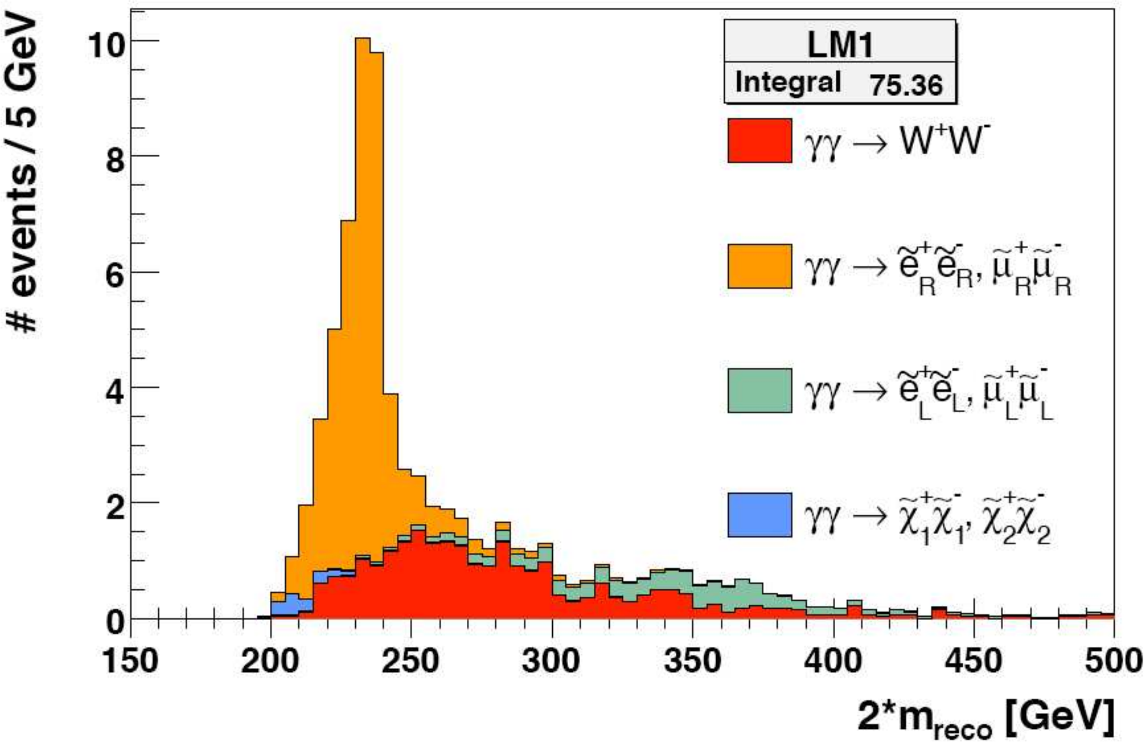

Figure 9.3: Distribution of the reconstructed mass for the LM1 SUSY signal and the WW background for an integrated luminosity of 100 fb^{-1}.

remaining consistent with the direct search limits from LEP. The production via $\gamma\gamma$ fusion has the added advantage over standard LHC production mechanisms of being a direct QED process, with minimal theoretical uncertainties.

In [67], the two-photon production of charged SUSY pairs is investigated for three benchmark points in mSUGRA/CMSSM parameter space. The two-photon production of $\tilde{e}^+\tilde{e}^-$, $\tilde{\mu}^+\tilde{\mu}^-$, $\tilde{\tau}^+\tilde{\tau}^-$ and charginos (χ_1, χ_2) in the fully leptonic decay channels are considered, which means that the final state consists of two leptons and a large amount of missing energy carried by the LSP and, in the case of $\tilde{\tau}/\chi$ pair production, neutrinos. Around 50 signal events with S/B$\sim$ 2 in 100 fb^{-1} are expected depending on the benchmark point chosen. Results for the LM1 SUSY point are shown in Figure 9.3.

.

9.3 New connection cryostat

The LHC dispersion suppressor and arc magnets are placed in one continuous cryostat from the Q7 quadrupole downstream of an IP, all the way to the Q7 quadrupole of the next IR [68]. At the position of the missing magnet of the dispersion suppressor, some 420 m downstream of each IP, there is a 14 m long Connection Cryostat (CC) which contains cold beam-pipes, the 2K heat exchanger, or X-line, and various cryo-lines which run throughout the continuous cryostat. The CC also carries the superconducting busbars of the main bending magnets and quadrupoles and nearly 100 superconducting cables for corrector magnets and other systems.

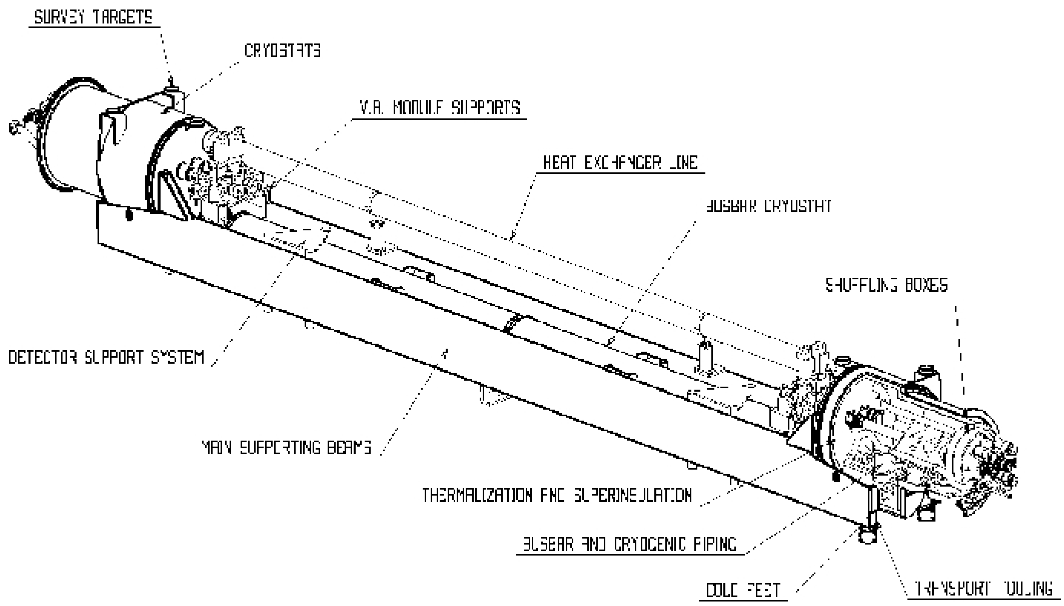

Figure 9.4: The new connection cryostat for FP420

There are sixteen CCs in the LHC, each made to be as similar as possible to a standard dipole magnet cryostat, at least as far as interconnection and handling are concerned. At this 420 m point, the dispersion function D, with the standard high luminosity optics, is approximately 2 m and hence protons from the IP which have lost around 1% of their momentum are well separated from the circulating beam, as described in Chapter 8. In order to allow the use of near-beam detectors at this 420 m position it is proposed to replace the existing connection cryostats on each side of IP1 with a warm beam-pipe section and a cryogenic bypass. A New Connection Cryostat (NCC) with approximately 8 m of room temperature beam-pipes has been designed using a modified Arc Termination Module (ATM) at each end.

In addition to two modified ATMs and warm beam-pipes, the NCC shown in Fig. 9.4 has a small cross section cryostat below the beam-pipes carrying all the cryo-lines and superconducting circuits and a new specially designed cryostat for the X-line. All this is supported by two longitudinal beams to make a single unit which can be directly exchanged for an existing connection cryostat. The passage of the X-line through the ATM modules is the main modification needed to the standard ATMs and the geometrical layout of this passage has been arranged to be as far away as possible from the downstream beam-pipe in order to leave adequate space for near-beam detectors and their associated equipment. The cross-section of the NCC, with the space around the beam-pipes available for detectors and associated mechanics, is shown in Fig. 9.5.

The existing connection cryostat contains a box structure of lead plates of 15 mm thickness enclosing the two beam-pipes to reduce the radiation field in the tunnel, essentially replacing the shielding provided by the cold mass in a standard arc dipole cryostat. The same thickness of lead shielding will be provided around the warm beam-pipes and detector stations of the NCC.

There are also short lengths of cylindrical shielding in the form of collars around the beam-

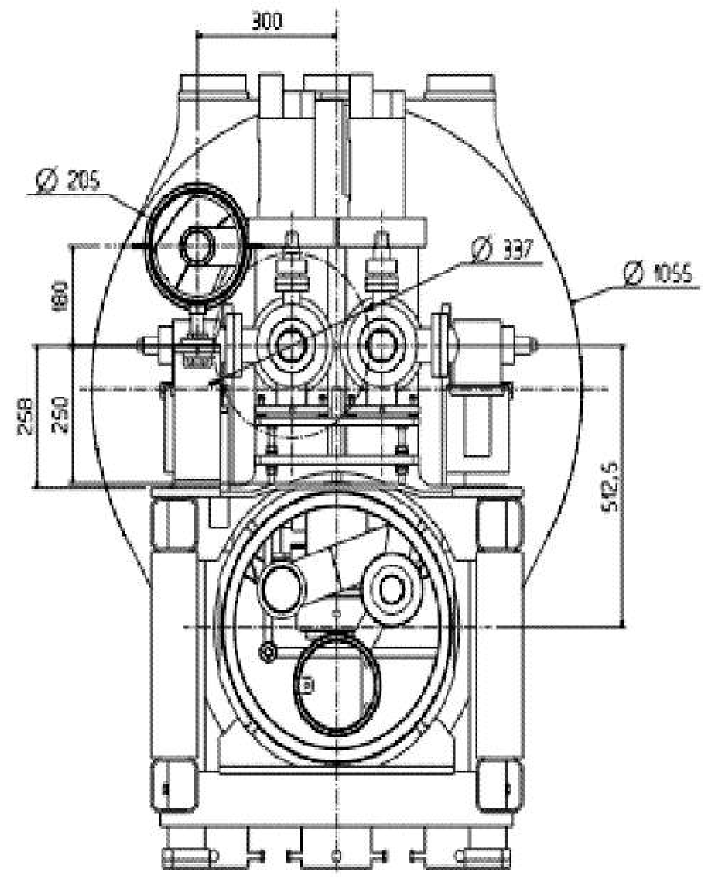

Figure 9.5: Cross-section view of the new connection cryostat for FP420

pipes at each end of the existing connection cryostat to limit the risk of quenching adjacent superconducting magnets. Similar collars will be incorporated into the modified ATM's at each end of the NCC in order to ensure that the NCC is at least equal to the existing cryostat in terms of influence on the local radiation fields and quench performance.

	Normal Days
Warmup from 1.9K to 4.5 K	1
Warmup from 4.5K to 300 K	15
Venting	2
Dismantling interconnection	10
Removal of the connection cryostat	2
Installation of the FP420 cryostat	5
Realization of the interconnections	15
Leak test and electrical test	4
Closing of the vacuum vessel	1
Evacuation/repump	10
Leak test	2
Pressure test	4
Cooldown from 300 K to 4.5 K	15
Cooldown from 4.5K to 1.9 K	3
Total [days]	89

Table 9.1: The estimated time in days required to install one NCC

The final engineering design of the new connection cryostat still has to be completed in the CERN central design office of the TS/MME group. The design aim is to meet or exceed the same specifications as the existing connection cryostat, whilst providing the maximum useable space for the silicon and timing detectors at 420 m. The preliminary design offers acceptable solutions for all cryogenic and mechanical engineering aspects as well as integration into the LHC environment [69, 70]. The final cryogenic performance will depend on the detailed design, but it has already been established that the additional static heat load arising from the two additional cold to warm transitions will be tolerable for the LHC cryogenic system. During LHC operation, simulations show that the NCC actually contributes a slightly lower dynamic heat load than the existing connection cryostat, because in the 8 m long warm section some synchrotron radiation is being absorbed at room temperature.

Since the completion of the preliminary design of the NCC the LHC collimation group have finalised their stage II collimator requirements and work has started on the construction of so-called 'cryo-collimators' for IR3, to be installed in the 2012/2013 long shutdown. The cryo-collimators are to be installed in what are currently cold sections of the LHC and a new cryo by-pass has been designed and is already under construction, based on similar ideas to the NCC [72] as shown in Fig. 9.6. In view of this it is now intended to base the final NCC design on the components of the new LHC cryo by-pass. Because the new collimators must be installed in the shortest possible beam length the original ATM based design used for the NCC has been abandoned and a new cold to warm transition designed in only 1.25 m. The new cryo by-pass provides 1.7 m of warm beampipe for the collimators in an over-all length of 4.2 m. Adapting this new mechanical concept to the NCC design should thus increase the distance available for detector stations by up to two metres, but the increased thermal contraction of the 14 m long NCC, compared to the 4.2 m by-pass, will have to be correctly taken into account and the

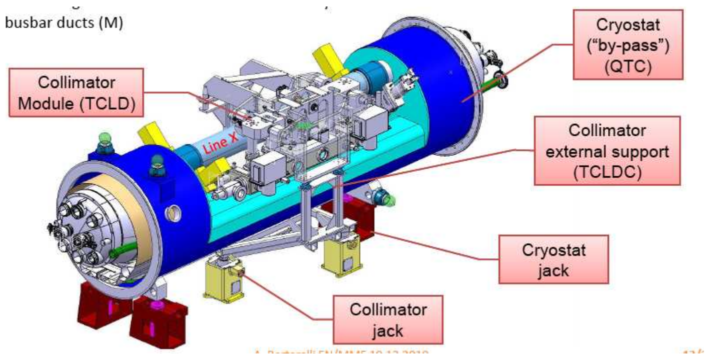

Figure 9.6: Schematic view of the cryo-bypass and collimator (Courtesy of V. Parma).

horizontal displacement of the X-line needed to allow access to the detectors will have to be made by means of dog-legs in the warm section. Both of these modifications should be straightforward, but will reduce the gain in space along the beamline. It also has to be noted that the cryo by-pass leaves only 100 mm below the beampipes for the collimator support and moving mechanism. This same distance was 250 mm with the preliminary NCC and hence the free space available has to be increased for the final NCC or the moving beampipe system will have to adopt the new collimator support and moving system. The latter solution would be preferable from the LHC machine point of view, but both possible solutions require a detailed engineering study. It has to be noted that the increased distance was needed to allow the detectors to be mounted on a separate table for stability and alignment reasons. Finally it is clear that the construction and installation of the cryo by-passes in the LHC in 2013 will greatly simplify the preparation and work needed to construct and install NCC's in 2016. While more design work will be needed to finalise the NCC's, all engineering solutions will have been checked out on the LHC and methods of construction and installation tried and tested. The cost of the NCC's should also be reduced [71].

The cutting and removal of the existing connection cryostat and its replacement by an NCC is very similar to the replacement of a standard LHC dipole and the task has been evaluated by the group responsible for all the LHC interconnections. Table 9.1 shows the sequence of operations and the estimated time needed in normal working days to complete the exchange of a connection cryostat from start of warm-up to being ready for beam. It is thus conceivable that the installation of an NCC cryostat and near-beam detectors could be completed in a three month shutdown. A preliminary study of the transport aspects has shown that adequate tooling exists and it can be expected that the time needed will be in the shadow of other operations shown in Table 9.1. However, the number of Connection Cryostats that can be replaced in any one shutdown will depend on the work load of the interconnection teams.

9.4 Summary

In summary, a preliminary design for a replacement connection cryostat that would allow near beam detectors to be placed in the 420 m region has been completed, and a final design can profit from the new cryo bypasses being installed in IR3 in 2013. The solution proposed is expected to have an acceptable cryogenic performance and give similar radiation profiles in the region. With the appropriate approvals and funding, two such cryosats could be built and ready for installation in the long shutdown of 2016, with negligible risk to LHC operations and performance for physics.

Bibliography

[1] A. Brandt, B. Cox, C. Royon *et al.* [AFP Collaboration], "Letter of Intent for ATLAS FP: A Project to Install Forward Proton Detectors at 220 m and 420 m Upstream and Downstream of the ATLAS Detector," `http://jenni.web.cern.ch/jenni/AFP.loi_atlas.pdf`.

[2] `http://www-hep.uta.edu/~brandta/ATLAS/AFP/AFP.html`

[3] V. M. Budnev, I. F. Ginzburg, G. V. Meledin and V. G. Serbo, Phys. Rept. **15** (1974) 181.

[4] E. Chapon, O. Kepka, C. Royon, Phys. Rev. **D81** (2010) 074003; O. Kepka and C. Royon, Phys. Rev. D **78** (2008) 073005.

[5] J. de Favereau de Jeneret *et al.*, arXiv:0908.2020 [hep-ph].

[6] A. Bialas and P. V. Landshoff, Phys. Lett. B **256** (1991) 540.

[7] V. A. Khoze, A. D. Martin and M. G. Ryskin, Eur. Phys. J. C **23** (2002) 311; V. A. Khoze, A. D. Martin, R. Orava and M. G. Ryskin, Eur. Phys. J. C **19** (2001) 313; A. B. Kaidalov, V. A. Khoze, A. D. Martin and M. G. Ryskin, Eur. Phys. J. C **33**, 261 (2004); V. A. Khoze, A. D. Martin and M. G. Ryskin, Eur. Phys. J. C **19** (2001) 477 [Erratum-ibid. C **20** (2001) 599].

[8] J. R. Cudell, A. Dechambre, O. F. Hernandez, arXiv 1011.3653; J. R. Cudell, A. Dechambre, O. F. Hernandez, I. P. Ivanov, Eur. Phys. J. C **61** (2009), 369; A. Dechambre, O. Kepka, C. Royon, R. Staszewski, arXiv:1101.1439.

[9] M. Boonekamp, R. Peschanski, C. Royon, Phys. Rev. Lett. **87** (2001) 251806; Nucl. Phys. B**669** (2003) 277; Phys. Lett. B**598** (2004)243; M. Boonekamp, A. De Roeck, R. Peschanski, C. Royon, Phys. Lett. B**550** (2002) 93; M. Boonekamp, C. Royon, J. Cammin and R. B. Peschanski, Phys. Lett. B **654** (2007) 104 [arXiv:0709.2742 [hep-ph]].

[10] T. Aaltonen *et al.* [CDF Run II Collaboration], arXiv:0712.0604 [hep-ex]; T. Aaltonen *et al.* [CDF Collaboration], Phys. Rev. Lett. **99** (2007) 242002

[11] A. Abulencia *et al.* [CDF Collaboration], Phys. Rev. Lett. **98** (2007) 112001.

[12] K. Piotrzkowski, Phys. Rev. **D63** (2001) 071502.

[13] G. Abbiendi *et al.* [OPAL Collaboration], Phys. Rev. D **70** (2004) 032005

[14] P. J. Bell, Eur. Phys. J. C **64** (2009) 25 [arXiv:0907.5299 [hep-ph]].

[15] C. Grojean (CERN & Saclay, IPhT), James D. Wells (CERN & Michigan U., MCTP), private communication.

[16] A. Brandt *et al.* [UA8 Collaboration], Phys. Lett. B **297** (1992) 417.

[17] V. Barone and E. Predazzi, *High-energy particle diffraction*, Springer, 2002.

[18] S. Alekhin *et al.*, “HERA and the LHC - A workshop on the implications of HERA for LHC physics: Proceedings Part B”, arXiv:hep-ph/0601013.

[19] M. Arneodo and M. Diehl, *“Diffraction for non-believers”*, hep-ph/0511047 (2005).

[20] M. Albrow *et al.* [CMS and TOTEM Collaborations], CERN-LHCC-2006-039; The FP420 R&D Project: Higgs and New Physics with forward protons at the LHC, JINST 4 T10001, hep-ex/0806.0302 (June 2008), accepted in J. Inst.: `http://www.iop.org/EJ/abstract/1748-0221/4/10/T10001`.

[21] M. Deile *et al.*, arXiv:1002.3527 [hep-ph], page 6.

[22] V. A. Khoze, A. D. Martin and M. G. Ryskin, Eur. Phys. J. C **18** (2000) 167 [arXiv:hep-ph/0007359].

[23] K.Piotrzkowski, U. Schneekloth, Proc. of the ZEUS Collaboration Meeting, March 1994, DESY, Hamburg.

[24] M. G. Albrow *et al.* [FP420 R&D Collaboration], arXiv:0806.0302 [hep-ex].

[25] A. Guerrero *et al.*,“CERN front-end software architecture for accelerator controls,” (ICALEPCS 2003), Korea, Oct 2003. in Gyeongju 2003, Accelerator and large experimental physics control systems, p. 342.

[26] M. Slater *et al.*, “Cavity BPM tests for the ILC energy spectrometer”, SLAC-PUB-13031.

[27] S. Walston *et al.*, “Performance of a High Resolution Cavity Beam Position Monitor System”, unpublished.

[28] CERN-LHCC-2010-013 / ATLAS-TDR-019 5/09/2010 https://espace.cern.ch/atlas-ibl/Shared%20Documents/ATLAS-TDR-019.pdf; http://indico.cern.ch/conferenceDisplay.py?confId=127

[29] T. E. Hansen et al., First Fabrication of Full3D Detectors at SINTEF, JINST **4** (2009) P03010.

[30] G. Pellegrini et al., First Double-Sided 3-D Detectors Fabricated at CNM-IMB, Nucl. Inst. Meth. **A592** (2008) 38.

[31] S. Parker, C. Kenney and J. Segal, 3D-A proposed New Architecture for Solid-State Radiation Detectors, Nucl. Inst. Meth. **A395** (1997) 328.

[32] C. Kenney et al., Silicon detectors with 3-D electrode arrays: fabrication and initial test results, IEEE Tr. Nucl. Sci **46** (1999) 1224.

[33] M. Mathes et al., Test Beam Characterizations of 3D Silicon Pixel Detectors, IEEE Tr. Nucl. Sci 55 (2008) 3731.

[34] P.O. Hansson et al., 3D Silicon Pixel Sensors: Recent Test Beam Results, Nucl. Inst. Meth. A321 (2010).

[35] C. Da Via et al., 3D Active Edge Silicon Sensors with Different Electrode Configurations: Radiation Hardness and Noise Performance, Nucl. Inst. Meth. 604 (2009) 505.

[36] G. Aad et al., ATLAS Pixel Detector Electronics and Sensors, JINST **3** (2008) P07007.

[37] A. Lounis et al., TCAD Simulations of the ATLAS Pixel Ring and Edge Structure for SLHC Upgrade, Internal Report ATL-UPGRADE-PUB-2010-001, ATL-COM-UPGRADE-2009-013, CERN, Geneva, Jan 2010.

[38] G. Kramberger et al., Comparison of Pad Detectors Produced on Different Silicon Materials after Irradiation with Neutrons, Protons and Pions, Nucl.Inst.Meth. **A 612** (2010) 288.

[39] L. Andricek et al., Processing of Ultra-Thin Silicon Sensors for Future Linear Collider Experiments, IEEE Tr. Nucl. Sci **51** (2004) 1117.

[40] L. Andricek et al., Nucl. Inst. Meth. (2010) in press, In Proc. of 7th International Hiroshima Symposium on Development and Applications.

[41] I. Mandic et al., Observation of Full Charge Collection Efficiency in Heavily Irradiated n+p strip Detectors Irradiated up to 3 x 10**15 n(eq)/cm2, Nucl. Inst. Meth. A612 (2010) 474.

[42] G. Casse et al., Enhanced Efficiency of Segmented Silicon Detectors of Different Thicknesses After Proton Irradiations up to 1x10**16 n(eq)/cm2, Nucl. Inst. Meth. In Press (2010).

[43] E. Mandelli et al., IEEE Trans. Nucl. Sci. 49 (4) (2002) 1774.

[44] L. Blanquart et al., IEEE Trans. Nucl. Sci. 49 (4) (2002) 1778.

[45] L. Blanquart et al., IEEE Trans. Nucl. Sci. 51 (4) (2004) 1358.

[46] ATLAS Collab., JINST **3** (2008) P07007.

[47] CMS Collab., NIM **A 552** (2005) 232.

[48] P-909: `http://www.cdf.fnal.gov/upgrades/btb.proposal.ps`.

[49] M. Akatsu, *et al.*, Nucl. Instr. and Meth. **A** 440 (2000) 124; M. Akatsu, *et al.*, Nucl. Instr. and Meth. **A** 528 (2004) 763; Y. Enari, *et al.*, Nucl. Instr. and Meth. **A** 547 (2005) 490.

[50] L. Bonnet, T. Pierzchala, K. Piotrzkowski, P. Rodeghiero. Acta Phys. Polon. B38 (2007) 477-482; hep-ph/0703320.

[51] CERN/LHCC 2002-016 Addendum to the ALICE TDR 8, 24 April 2002.

[52] `http://www.nightvision.com/products/military/case_study-gen3.htm`

[53] N. Kishimoto, et al., Nucl. Instr. and Meth. **A** 564 (2006) 204; T. Mori, "Lifetime of HPK Square-shape MCP-PMT," Cracow Fast Timing Workshop, Dec. 2010 (`http://www-d0.fnal.gov/r̃oyon/timing_cracow/`).

[54] I. Baichev, J.-B. Jeanneret and G.R. Stevenson, *Beam losses far downstream of the high luminosity interaction points of LHC - intermediate results*, LHC-Project Note 208, CERN, 2000

[55] E. Forest, F. Schmidt and E. McIntosh, "Introduction to the Polymorphic Tracking Code", CERN-SL-2002-044-AP, KEK report 2002-3, July 2002.

[56] R. Assmann *et al*, The proceedings of PAC03, pag. 3496.

[57] The LHC design report, CERN-2004-003 (2004)

[58] P.J. Bussey and W. Plano, FPTrack, in preparation.

[59] J. Monk and A. Pilkington, Comput. Phys. Commun. **175** (2006) 232 [arXiv:hep-ph/0502077]; M. Boonekamp, A. Dechambre, V. Juranek, O. Kepka, M. Rangel, C. Royon, R. Staszewski, [arXiv:1102.2531].

[60] R Staszewski et al,. ATL-COM-LUM-2009-016, Nucl. Instr. Meth. A609 (209) 136

[61] M. G. Albrow and A. Rostovtsev, arXiv:hep-ph/0009336.

[62] B. Cox, F. Loebinger, A. Pilkington, JHEP 0710 (2007) 090; S. Heinemeyer et al., Eur. Phys. J. C **53** (2008) 231.

[63] J. R. Ellis, J. F. Gunion, H. E. Haber, L. Roszkowski and F. Zwirner, Phys. Rev. D **39** (1989) 844; J. R. Ellis, J. S. Lee and A. Pilaftsis, Phys. Rev. D **71** (2005) 075007 [arXiv:hep-ph/0502251].

[64] V. A. Khoze, A. D. Martin and M. G. Ryskin,

[65] R. Dermisek, J.F. Gunion. Phys. Rev. Lett. **95** (2005) 041801. Eur. Phys. J. C **34** (2004) 327

[66] J. R. Forshaw, J. F. Gunion, L. Hodgkinson, A. Papaefstathiou and A. D. Pilkington, JHEP **0804** (2008) 090 [arXiv:0712.3510 [hep-ph]].

[67] J. Ohnemus, T.F. Walsh and P.M. Zerwas, Phys. Lett. B328 (1994) 369-373; G. Bhattacharya *et al.*, Phys. Rev. D 53, (1996) 2371; M. Drees *et al.*, Phys. Rev. D 50, (1994) 2335; N. Schul and K. Piotrzkowski, arXiv:0806.1097.

[68] “LHC Design Report Vol. 1”, CERN-2004-003, CERN, Geneva, Switzerland (2004).

[69] T. Columbet, “Cryogenics preliminary calculation for the FP420 cryostat”, https://edms.cern.ch/document/827775.

[70] S. Pattalwar *et al.* “A New Connection Cryostat to insert FP420 Proton Tagging Detectors in the LHC Ring”, Proceeds APAC (2007) 103.

[71] R. Folch, “FP420 Cryostat Modules Workpackage”, https://edms.cern.ch/document/823322.

[72] V. Parma, talk at the Chamonix Workshop, January 2011.